Prediction of Nitric Oxide Concentrations During Inflammation and Carcinogenesis

by

Melanie Pei-Heng Chin

B.S. Chemical Engineering, B. A. Chemistry (2004)
North Carolina State University
M. S. Chemical Engineering Practice (2006)
Massachusetts Institute of Technology

Submitted to the Department of Chemical Engineering
In Partial Fulfillment of the Requirements of the Degree of

DOCTOR OF PHILOSPHY IN CHEMICAL ENGINEERING

at the

MASSACHUSETTS INSTITUTE OF TECHNOLOGY

February, 2010

Signature of Author.... ....

Department of Chemical Engineering
January 28, 2010

Certified by..

William M. Deen
Carbon P. Dubbs Professor of Chemical Engineering
Thesis Supervisor

Accepted by........... ....

William M. Deen
Carbon P. Dubbs Professor of Chemical Engineering
Chairman, Committee for Graduate Students

Abstract

Nitric oxide is a biological messenger which is synthesized enzymatically throughout the body and which has numerous physiological functions, including roles in blood pressure control, regulation of clotting, and neurotransmission. It is produced also by macrophages as part of the non-specific immune response, and has been shown to be toxic to invasive microorganisms. However, sustained overproduction of NO, as observed with chronic inflammation or infection, may damage the host tissue and has been linked to increased risk for cancer. Nitric oxide may facilitate tumorigenesis or metastasis by influencing tumor-cell proliferation, angiogenesis, or lymphangiogenesis. However, the concentrations of NO in inflamed tissues or during carcinogenesis are largely unknown. The objective of the research in this thesis was to predict NO concentrations in an inflamed colon and a cutaneous metastatic melanoma, two areas where NO has been implicated in the development or progression of disease.

Nitric oxide production in the colon has been linked to inflammatory bowel disease (IBD) and increased risk for colon cancer. However, measurements of NO concentration in the inflamed colon have not been available and it is not known what levels of NO are pathophysiological. A computational model, based on anatomical length scales and rates of NO production measured in cell cultures, was developed to predict spatially varying NO concentrations within a colonic crypt under inflammatory conditions. A variety of scenarios were considered, including different spatial distributions of macrophages and a range of possible macrophage and epithelial synthesis rates for NO. The results were used to predict the range of NO concentrations (<0.3 μM) and cumulative NO dose (560 μM • min) experienced by a given epithelial cell migrating from the base to the top of the crypt. This first set of predictions was based on literature data on the cellular synthesis and consumption of NO.

Knowledge of the rates at which macrophages and epithelial cells synthesize NO is critical for predicting the concentrations of NO and other reactive nitrogen species in colonic crypts during inflammation, and elucidating the linkage between inflammatory bowel disease, NO, and cancer. Macrophage-like RAW264.7 cells, primary bone marrow-derived macrophages (BMDM), and HCT116 colonic epithelial cells were subjected to simulated inflammatory conditions, and rates of formation and consumption were determined for NO, O_2, and O_2^-. Production rates of NO were determined in either of two ways: continuous monitoring of NO concentrations in a closed chamber, with corrections for autoxidation; or NO_2^- accumulation measurements in an open system, with corrections for diffusional losses of NO. The results obtained using the two methods were in excellent agreement. Rates of NO synthesis (2.3 ± 0.6 pmol s^{-1} 10^6 cells^{-1}), NO consumption (1.3 ± 0.3 s^{-1}), and O_2 consumption (58.8 ± 17 pmol/s/10^6 cells) for activated BMDM were indistinguishable from those of activated RAW264.7 cells. NO production rates calculated from NO_2^- accumulation data for HCT116 cells infected with *Helicobacter cinaedi* (3.9 ± 0.1 pmol/s/10^6 cells) were somewhat greater than those of RAW264.7 macrophages infected under similar conditions (2.6 ± 0.1 pmol/s/10^6 cells). Thus, RAW264.7 cells have nearly identical NO kinetics to primary macrophages, and stimulated epithelial cells are capable of synthesizing NO at rates comparable to macrophages. Using this new cellular data to refine the predictions of the colon model, simulations of NO diffusion and reaction in a crypt during inflammation gave maximum NO concentrations of about 0.2 μM.

The presence of iNOS and nitrotyrosine in human metastatic melanoma tumors suggest that NO plays a role in the pathophysiology of metastatic melanomas. However, the concentrations of NO that melanoma cells are exposed to *in vivo* remains unknown. Cellular rates of NO synthesis and consumption were experimentally determined and used in a reaction-diffusion model to predict NO concentrations in a cutaneous melanoma. NO synthesis by A375 melanoma cells was undetectable using Griess assays. The rate constant for intracellular NO consumption by A375 cells ($7.1 \pm 1.1\ s^{-1}$), was determined by monitoring NO concentrations in a closed chamber with corrections for autoxidation and consumption from media-generated O_2^{-}. Incorporating NO kinetic data from A375 cells and macrophages into a reaction-diffusion model, NO was found to be localized to the periphery of the melanoma; roughly 90% of the NO synthesized by macrophages is consumed within 30 μm of the tumor edge. Several additional scenarios were modeled, including the effects of varying the volume fraction of macrophages surrounding a melanoma tumor and intratumoral NO synthesis by melanoma cells. As such, a range of NO concentrations were predicted (< 0.2 μM) for the edge of the tumor. Our model may offer some insight into the role NO plays in the metastasis of cutaneous melanomas, which occurs primarily through lymphatic spread. At the melanoma edge, NO may inhibit melanoma cell apoptosis, contributing to abnormal tumor growth and invasion of local lymph vessels or NO may act as a lymphangiogenic factor.

The colonic crypt model and the cutaneous melanoma model developed in this work provide the first NO concentration predictions for tissues during inflammation. Despite the different geometries and different cell types involved, the maximum values estimated in both cases were ~ 0.2 μM. The results from this work can be used for predicting intracellular levels of other reactive nitrogen species, and should help guide further studies to understand the mechanisms by which NO contributes to carcinogenesis in IBD and in cutaneous melanomas.

Acknowledgements

I would like to express my sincerest thanks and appreciation for my thesis advisor, Professor William M. Deen. He has provided unending scientific insight and guidance as well as patience and encouragement. He has been a true mentor, teacher, and friend throughout my academic career at MIT.

I would also like to thank my thesis committee members, Professors James G. Fox, Kristala J. Prather, Gerald N. Wogan, as well as David B. Schauer, who passed away in May 2009, for their interesting ideas, discussions, and important feedback. Thanks to members of the Deen group including Kristin Mattern, Gaurav Bhalla, Brian Skinn, and Chang Hoon Lim for making the lab an enjoyable place. Thanks to Laura Trudel for all of her help with cell culture and for making the basement of Building 26 a fun place to work.

I cannot thank my parents enough for their unending love and support. Lastly, I would like to thank all the friends I have made at MIT for making graduate school incredibly memorable. In particular, I owe a lot to John Angelos. Whether it was studying together during first year, accompanying me to the lab late at night, listening to presentations, or just making me laugh on bad days, he helped me get through graduate school.

Table of Contents

List of Tables

List of Figures

Chapter 1. Introduction

1.1. Biological Impact of Endogenous Nitric Oxide

Nitric oxide is a biological messenger that participates in many physiological pathways. NO is formed from the guanidine nitrogens of L-arginine via an enzymatic oxidation caused by NO synthase (NOS) [Nathan, 1992]. The isoforms of NOS include constitutive NOS in endothelium (eNOS) and neurons (nNOS), as well as an inducible form (iNOS). As constitutive NOS isoforms, nNOS and eNOS exist in the cell as preformed proteins whose activity is switched on by the elevation of intracellular Ca^{2+} concentrations, resulting in relatively low levels of NO. The expression of iNOS, on the other hand, is regulated by cytokines with enzyme activity lasting for days or weeks, and produces a much higher level of NO. The *de novo* synthesis of iNOS mRNA and protein is induced by interferon-gamma (IFN-γ), a cytokine which is most characteristic for type 1 T-helper cells [Dalton, et al., 1993].

NO plays many roles *in vivo*. NO acts as a vasodilator when released by the endothelium of blood vessels and functions as a neurotransmitter and neuromodulator in the central and peripheral nervous systems. The regulatory roles of NO in the neuronal and vascular systems require the low levels of NO derived from nNOS or eNOS. In its protective role as part of the immune system, however, NO is associated with the expression of iNOS and prolonged, high NO production.

1.2. Nitric Oxide and the Immune Response

The innate immune system consists of certain types of cells and humoral factors that recognize, inactivate, and kill infectious agents. Mechanisms of defense include the phagocytosis of bacteria by neutrophils or macrophages and the production of nitric oxide and superoxide. Macrophages are terminally differentiated mononuclear phagocytes that originate in the bone marrow and pass out of blood vessels for distribution throughout the body.

Macrophages are activated when the inductive signal binds to suitable receptors on the cell surface. One inducer, IFN-γ, 'primes' macrophages; in the primed state, the macrophages can bind to tumor cells without secreting lytic mediators. However, with the addition of bacterial lipopolysaccharide (LPS), macrophages become fully activated, allowing the cells to secrete factors that assist in the killing of invading microorganisms, tumor cells, or infected host cells.

Cytokines and microbial products often act in synergistic pairs to induce expression of iNOS. IFN-γ and bacterial LPS are the prototypic, best-studied examples of iNOS inducers, and are effective stimulators of mouse macrophages either in combination or alone. Tumor necrosis factor (TNF) in conjunction with any of the interferons (including α and β) or interleukin 1-beta (IL-1*β*) has also been shown to elicit NO production in murine macrophages *in vitro* [Nathan, 1992; Pahan, et al., 1997]. Among viral and microbial products, lipoprotein of *Mycobacterium tuberculosis*, the flagella of gram-negative bacteria, *Salmonella typhimurium*, and DNA from various protozoan parasites have all been shown to elicit NO production by macrophages [Mori, et al., 1999; Gao, et al, 1999; Ohashi, et al., 2000; Cherayil, et al., 2000; Shoda, et al., 2001; Thoma-Uszynski, et al., 2001]. In addition, several noncytokine, nonmicrobial substances, such as ozone and asbestos, induce iNOS or augment its induction [Nathan, et al., 1994].

The study of macrophage-synthesized nitric oxide evolved from early work trying to understand the association between exposure to high levels of nitrates and gastric cancer. In several studies, mammals maintained on low nitrate diets excreted more nitrate than ingested [Tannenbaum et al, 1978]. In rats, treatments with *Escherichia coli* LPS led to approximately a

10-fold increase in urinary nitrate (NO_3^-) [Wagner et al, 1983], and macrophages were later shown to be a major source of this nitrate in LPS-treated mice [Stuehr and Marletta, 1985]. Establishing LPS and IFN-γ as stimulators of primary macrophage cultures, Stuehr and Marletta also compared several murine macrophage cell lines (RAW264.7, WEHI-3, PU5-1.8, J774A.1, and P338D1) to peritoneal primary macrophages by measuring the synthesis of nitrite/nitrate under these stimulatory conditions [Stuehr and Marletta, 1987]. However, nitrite or nitrate themselves could not replicate the cytotoxicity of macrophages except at acid pH [Stuehr and Nathan, 1989], a condition in which nitrite can generate NO. This, along with the discovery that nitric oxide is formed as an intermediate in the L-arginine to NO_2^-, NO_3^-, and citrulline pathway [Marletta, et al., 1988], helped establish that macrophages synthesize nitric oxide to assist in the killing of invading microorganisms. Use of animal model systems proved that NO produced by macrophages *in vivo* was genotoxic in target tissues [Gal and Wogan, 1996].

Although activation of iNOS has been demonstrated extensively in mouse macrophages, and even in other different types of animal macrophages, including cow [Adler et al., 1995], horse, sheep, and goat [Jungi et al., 1996], there was debate over whether or not human macrophages are capable of NO generation. Initial skepticism was fueled by studies showing blood monocytes from normal American donors contain little or no functional NOS protein [Weinberg, et al., 1993]. *In vitro* treatment of human peripheral blood mononuclear cells with LPS and IFN-γ also failed to elicit NO production [Schneemann, et al., 1993], even though these stimuli are highly effective in activating murine macrophages. However, as described next, it is now generally accepted that human macrophages produce NO.

NO production by humans was first consistently demonstrated in patients with infections or inflammatory conditions [Dykhuizen, et al., 1996]. iNOS expression was observed within different inflamed tissues of patients with sepsis [Annane, et al., 2000] and in macrophages from patients with tuberculosis [Nicholson, et al., 1996], rheumatoid arthritis [St. Clair, et al., 1996], and malaria [Anstey, et al., 1996]. Mononuclear phagocytes taken from these patients, studied either directly or following stimulation *in vitro* with cytokines, were found to express iNOS. These results suggested that NO production by human macrophages is more readily detectable when the cells are activated *in vivo.* Given the biochemical evidence of NO production [Vouldoukis, et al., 1995] and that iNOS mRNA and protein expression have been repeatedly demonstrated in activated human macrophages [Kobzik, et al., 1993; Reiling, et al., 1994; Weinberg, 1998], there is no longer any doubt that human monocytes and macrophages can express functional iNOS at the protein level or that NO secretion by macrophages plays a role in the human innate immune response. The differences in NO induction between human and rodent macrophages may be due to species variations or from maturation and specialization of the cells; murine studies use mature macrophages whereas studies in humans use bloodstream monocytes.

1.3. Pathophysiology of Nitric Oxide

1.3.1. Reactive Nitrogen Species formed from NO

Although NO is necessary for normal physiological function, it is cytotoxic and mutagenic at high concentrations. Overproduction of NO has been observed in infectious or inflammatory states of the colon, bile duct, and liver [Tamir and Tannenbaum, 1996]. While NO can act directly, much of its cytotoxicity may be due to reactive products associated with NO.

As mentioned, under inflammatory conditions, neutrophils and macrophages produce superoxide along with NO. Superoxide is a byproduct of cell aerobic metabolism and interaction of molecular oxygen with free electrons from the mitochondrial electron transport chain results in its generation [Halliwell and Gutteridge, 1989]. Although it is scavenged by superoxide dismutase (SOD), it is present in virtually all cells [Boveris, et al., 1972; Bray, et al., 1974; Tyler, 1975]. Superoxide is also generated by an NADPH oxidase on the external membrane surface of macrophages, thereby contributing extracellular generation of O_2^- [Babior, 1984; Berton et al., 1988]. Superoxide (O_2^-) and other reactive oxygen species are known to cause DNA damage from base modification and strand breaks [Trush and Kensler, 1991]. Left unrepaired, the DNA damage may lead to permanent mutations and possibly cancer.

The rapid reaction of NO with superoxide forms peroxynitrite, $ONOO^-$. Peroxynitrite can cause lipid peroxidation [Radi et al., 1991] and irreparable damage to DNA, including oxidation of bases, single-strand breaks, and DNA-DNA cross links [Burney et al., 1999; Tretyakova et al., 2000]. Peroxynitrite also leads to the opening of the permeability transition pore in the inner mitochondrial membrane [Packer et al, 1997], an event linked to necrosis and apoptosis [Hirsch et al., 1997]. Consequently, $ONOO^-$ has been linked to cancer and neuro-degenerative disorders such as Alzheimer's disease [Smith et al., 1997].

NO can also react with oxygen to form nitrous anhydride, N_2O_3, which is a powerful electrophilic nitrosating agent. N_2O_3 may damage DNA directly through nitrosation of primary amines on DNA bases or indirectly by nitrosating various secondary amines to form N-nitrosamines. When metabolized, these carcinogenic ntirosamines can in turn react with DNA at multiple nucleophilic sites and lead to deamination and cross-linking of DNA. [Tannenbaum et al, 1994].

1.3.2. NO and Carcinogenesis

In part due to these reactive nitrogen species, excessive amounts of NO can lead to cytotoxicity, which when chronic, results in enhanced cell replication and increased risk for cancer. In fact, epidemiological studies demonstrate an association between chronic inflammation and increased cancer risk [Ohshima and Bartsch, 1994]; examples include inflammatory bowel disease and colon cancer [Levin, 1992; Farrell and Peppercorn, 1997], *Helicobacter pylori* infection and gastric cancer [Asaka *et al*, 1997; Ebert *et al*, 2000], and *Schistosoma haematobium* infection and bladder cancer [Badawi *et al*, 1995; Mostafa *et al*, 1999]. Thus, the damage of host tissue under prolonged exposure to high concentrations of NO, as seen with chronic disorders, suggests a causative role for NO in the pathophysiology of these diseases [Tamir and Tannenbaum, 1996].

Moreover, a series of studies also implicate NO in tumorigenesis [Hofseth, et al., 2003; Crowell, et al., 2003]. For example, the incidence of gastric carcinogenesis induced by *Helicobacter pylori* is decreased in iNOS-deficient mice [Nam et al., 2004]. NO may influence tumor progression and metastasis directly by contributing to tumor-cell proliferation, migration and invasion, and indirectly through the expression of angiogenic and lymphangiogenic factors. Histological examinations show a correlation between high angiogenic activity or high VEGF expression and iNOS expression in human brain [Ludwig, et al., 2000], head and neck [Gallo, et al., 1998], lung [Marrogi, et al., 2000], breast [Vakkala, et al., 2000], stomach [Song, et al., 2002] and colon [Ambs et al., 1998] tumors. Similarly, lower VEGF expression and slower growth of B16 melanomas has been observed in iNOS deficient mice, which suggests that iNOS promotes tumor growth through induction of VEGF expression and angiogenesis [Konopka et al., 2001].

In addition, there is evidence that iNOS expression and/or activity correlates positively with lymph-node metastasis, which occurs from the invasion of tumor cells into the lymphatic vessels and eventually the lymphatic system. Clinical studies suggest that NO is involved in this process in several types of tumors including head and neck [Franchi, et al., 2006], breast [Nakamura et al., 2006], melanoma [Massi, et al., 2009], and gall-bladder tumors [Niu, et al., 2004], whereby NO exposure induces vascular endothelial growth factor C (VEGFC) expression. VEGFC is a putative lymphangiogenic factor that mediates lymphangiogenesis and metastasis [Alitalo, et al., 2002]. Thus there exists a growing body of evidence that indicates NO has a role in the regulation of tumorigenesis, tumor angiogenesis and lymphangiogenesis, progression and metastasis.

1.4. Existing Models for NO

The first mathematical models for the biotransport of nitric oxide calculated concentration profiles by modeling one-dimensional diffusion of NO generated from point sources [Lancaster 1994, Wood and Garthwaite, 1994]. Approximating the reaction of NO as first order, Lancaster found that NO could diffuse to significant concentrations over fairly long distances. Similarly, Wood and Garthwaite (1994) modeled the diffusion of NO generated in neurons as either single or multiple point sources in the brain. The results from their model suggested that a single point source of NO could influence approximately two million synapses by diffusion to a volume of brain tissue 200μm in diameter. Both of these works were significant in elucidating NO's diffusive capabilities but had limitations as one-dimensional point-source models. More extensive models considered the geometrical structure of NO sources as important factors in the diffusion process. Philippides, et al. (2000) modeled NO diffusion from hollow spherical neurons in the brain. Vaughn, et al. modeled the diffusion of NO produced in endothelium into surrounding tissue using both first order and second order decay terms (1998). However, these models are for scenarios in neuronal signaling and in the endothelium; when the research in this thesis began, there were no existing models for nitric oxide production in tissue during the immune response.

Although there were no previous models for NO in inflamed tissue, reaction-diffusion models have been developed to predict NO concentrations in various cell culture experiments. In particular, Chen and Deen (2002) described spatial and temporal changes in NO, O_2^-, peroxynitrite, and N_2O_3 concentrations for macrophages in plated cell culture configurations. Nalwaya and Deen (2004) incorporated additional factors in modeling NO and O_2 concentrations for activated macrophages in plated cell culture, including the inhibitory effect of NO on respiration. The reactions involving NO and O_2 in these cell culture experiment models are also used for estimating NO levels in tissue. Moreover, it was shown that unlike NO, which is more diffuse, the fast chemical kinetics of reactions involving O_2^- and peroxynitrite are such that their concentrations are confined to small regions near the cells. As such, NO levels in tissue can be estimated independently from the complex reaction schemes involving other reactive nitrogen species. Once the tissue concentrations of NO are estimated, the concentrations of other reactive NO products can be calculated separately using detailed intracellular models [Lim, et al., 2008].

1.5. Known Cellular Kinetic Rates

1.5.1. NO Synthesis by Macrophages

The rates at which cells synthesize or consume NO is critical for predicting NO concentrations in tissue during inflammation. Of the macrophage cell lines that Stuehr and Marletta studied, RAW 264.7 cells were shown to synthesize nitrite and nitrate at rates similar to those of primary macrophages [Stuehr and Marletta, 1987]. Subsequently, RAW cells became commonly used in lieu of primary macrophages in NO toxicity studies [Lewis and Deen, 1995; deRojas-Walker et al, 1995; Nalwaya and Deen, 2004; Nalwaya and Deen, 2005]. The specific activation conditions of RAW 264.7 cells in plated cell cultures has been well characterized; the effects of cell density, varied LPS- and IFN-γ concentrations [Zhuang and Wogan, 1997], liquid depths [Chen and Deen, 2002], and activation times [Lewis and Deen, 1994] have all been investigated. With these established stimulation conditions, several studies have determined nitric oxide synthesis in activated macrophage cultures by measuring concentrations of nitrite and nitrate, the main products of NO oxidation [Marletta et al, 1988; Lewis and Deen, 1994; deRojas-Walker et al, 1995]. One limitation of this approach is that NO production by cells may be underestimated because it assumes that NO diffusion out of the liquid is negligible. In reality, the diffusional loss of NO to the headspace is usually quite significant in typical plate culture systems [Chen and Deen, 2001]. Using a closed chamber fitted with NO and O_2 sensors, Nalwaya was the first to use time-dependent NO and O_2 concentrations simultaneously in plated RAW 264.7 cell cultures to determine NO kinetic rates more directly [Nalwaya and Deen, 2005]. However, it remained unclear how NO kinetic rates of macrophage-like RAW264.7 cells compare with those of primary macrophages.

1.5.2. NO Synthesis by Cells other than Macrophages

Colonic biopsies from patients with inflammatory bowel diseases show pronounced expression of iNOS in the colonic epithelium [Rachmilewitz, et al., 1995] but little is known about the regulation of iNOS activity in colonic epithelial cells. Under basal conditions, minimal quantities of NO are produced in the colonic epithelium, as evidenced by nitrite and nitrate accumulation measured in cultured colonic explants [Rachmilewitz, et al., 1995; Ribbons, et al., 1995]. Because epithelial cells in healthy mucosa do not express iNOS, it is believed that enzyme activity is also induced by cytokines released in the inflamed tissue; time course studies have demonstrated a time-dependent expression of iNOS mRNA, first observed at 6 hours and maximal at 24 hours after cytokine exposure [Dignass et al, 1995]. Cultured primary colonic epithelial cells harvested from rats and HT-29 human colonic epithelial cells express iNOS and generate increased levels of NO in response to stimulation by IFN-γ and LPS, as well as other cytokines such as IL-1α, TNF-α, and enteroinvasive *E. coli* [Dignass et al, 1995; Witthoft et al, 1998; Kolios et al, 1998; Wright et al, 1999]. However, rates of NO production, inferred from these reported nitrite accumulation rates vary by some two orders of magnitude [Witthoft et al, 1998; Wright et al, 1999], with the upper end of these rates corresponding to NO synthesis that is roughly an order of magnitude less than that of macrophages [Nalwaya and Deen, 2005]. The uncertainty over the rates of colonic epithelial cell NO synthesis may be attributed to variable experimental setups, such as unreported liquid depths of the culture media, which can affect the diffusional loss of NO and the inferred NO synthesis rates. Regardless, the data do support the notion that proinflammatory cytokines or bacteria induce NO production in colonic epithelial cells.

Metastatic melanoma tumors excised from patients have been shown to express low levels of iNOS [Ekmekcioglu, et al., 2000]. *In vitro* studies have also established positive iNOS expression in A375 and MeWo human melanoma cell lines [Zheng et al., 2004], primary melanoma cells isolated from metastatic lesions, and in normal adult melanocytes [Salvucci et al., 2001]. However, despite demonstrating iNOS expression in A375 and MeWo cells, Zheng et al. (2004) found that levels of nitrite accumulation were barely detectable. Other studies have also reported negative Griess results for melanoma cells in culture, including K-1735 C4 murine metastatic melanoma cells [Xie et al., 1995] and G361, a human melanoma cell line [Andrews et al., 1995]. Thus, it remains unclear whether melanoma cells actually produce NO from iNOS;

melanoma cells have also been shown to express the other constitutive isoforms of nitric oxide synthase (eNOS and nNOS), [Salvucci et al., 2001; Ahmed and Van Den Oord, 1999] which may contribute to low levels of NO production.

1.5.3. Cellular NO consumption

Another consideration in measuring rates of NO synthesis is that cells also consume NO. In addition to the reaction between NO and superoxide, which occurs in all cells, NO may also be consumed via enzymatic pathways. For instance, NO dioxygenase (NOD) is responsible for the oxidation of NO to NO_3^- in certain mammalian cells [Gardner et al, 2000]. NO may also react with oxygen-ligated reduced metals to produce NO_3^- and the oxidized metal [Eich et al, 1996]. Measurements of NO consumption by rat hepatocytes indicate that the overall intracellular NO consumption rate via these various mechanisms can be modeled as being first order in NO concentration [Thomas et al, 2001]. The extent that any of these mechanisms occur in cells will tend to limit the maximum achievable NO concentration. The rates of NO consumption measured for a variety of cell types are summarized in Table 1.1. The wide range of values is likely to stem from differences in cell types as well as the variations in cell culture and growth conditions. Most of the cells listed in Table 1.1 are adherent cells grown on tissue culture plates, with the exception of TK6 and NH32, which are grown in suspension, and Caco-2 cells, which are grown on semi-permeable filters.

1.5.4. Oxygen consumption

Respiration rates (R_{max}) have been measured for a variety of mammalian cell types. O_2 consumption rates for different hybridoma cell types are reviewed by Ruffieux et al. (1998); the average O_2 uptake rate from the eleven studies surveyed was 55 pmol/s/10^6 cells. In addition, several other mammalian respiration rates have been measured, and are listed in Table 1.2. As seen, the rates of respiration by the various cell types are all on the same order of magnitude and fall in the range between ~20 to 60 pmol/s/10^6 cells.

1.5.5. Extracellular Superoxide Production

The synthesis of extracellular superoxide by macrophages involves NADPH, a plasma-bound enzyme. The release of superoxide occurs upon phagocytosis of bacteria and assists in the subsequent killing of the ingested microorganisms. Stimulated production of O_2^- was first described as a "respiratory burst" because the release of superoxide during phagocytosis corresponded to an observed increase in cellular oxygen consumption [Drath and Karnovsky, 1975]. While the respiratory burst typically continues for a few minutes after activation (and can last for as long as one hour) in certain types of macrophages [Berton, et al., 1988], superoxide synthesis has been shown to remain constant for up to three days with constant stimulation [Johnston, et al., 1978]. Activators for superoxide production in macrophages include phorbal 12-myristate 13-acetate (PMA) [Auger and Ross, 1992], zymosan, as well as IFN-γ or the combination of IFN-γ and LPS [Nathan, et al., 1983; Nathan, et al., 1984; Murray, et al., 1985]. Moreover, unlike stimulation of nitric oxide production, there is no apparent time lag for cellular O_2^- synthesis [Johnston, et al., 1978; Chen and Deen, 2002; Nalwaya and Deen, 2005]. Murine resident peritoneal macrophages (PM) have been shown to generate O_2^- under control conditions at either negligible or very low rates [Drath and Karnovsky, 1975; Johnston, et al., 1975].

Table 1.1. Comparison of rate constants for intracellular NO consumption by various mammalian cell types

Cell	**Cell Type**	k_c (s^{-1})	**Reference**
NH32	Human lymphoblast	0.1	C. Wang, 2003
TK6	Human lymphoblast	0.3	C. Wang, 2003
RAW264.7	Macrophage	0.6	Nalwaya and Deen, 2005
βTC3	Pancreatic β	1.7	C. Wang, 2003
K9	Rat hepatocyte	2	Gardner et al., 2001
PC12	Rat adrenal pheochromocytoma	4	Gardner et al., 2001
K562	Human myelogenous leukemia	5	Gardner et al., 2001
MLE	Murine lung epithelial	9	Gardner et al., 2001
A549	Human lung adenocarcinoma	9	Gardner et al., 2001
Caco-2	Human colonic epithelial	38	Gardner et al., 2001

Table 1.2. Comparison of oxygen consumption rates by various mammalian cell types.

Cell	**Cell Type**	$R_{max}\left(\frac{pmol}{s\cdot10^6\,cells}\right)$	**Reference**
various	Hybridoma cells	55	Ruffieux, et al., 1998
K9	Rat hepatocyte	33	Gardner et al., 2001
PC12	Rat adrenal pheochromocytoma	33	Gardner et al., 2001
K562	Human myelogenous leukemia	17	Gardner et al., 2001
MLE	Murine lung epithelial	57	Gardner et al., 2001
A549	Human lung adenocarcinoma	43	Gardner et al., 2001
Caco-2	Human colonic epithelial	42	Gardner et al., 2001
J774.1	Unactivated murine macrophage	16	Brown et al., 1998
RAW264.7	Unactivated murine macrophage	33	Nalwaya and Deen, 2005

Table 1.3. Comparison of reported O_2^- formation rates for primary murine macrophages

Cell	**Stimulant**	***O_2^- formation*** (pmol/mg protein/min)	**Reference**
PM	none	0.08	Drath and Karnovsky, 1975
PM	zymosan	1.07	Drath and Karnovsky, 1975
PM	none	0.002	Johnston, et al., 1978
PM	zymosan	0.16	Johnston, et al., 1978
J774	zymosan	0.07	Johnston, et al., 1978
PU5-1.9	zymosan	0.06	Johnston, et al., 1978
P388D1	zymosan	0.03	Johnston, et al., 1978
Human monocyte	zymosan	0.2	Johnston, et al., 1978
BMDM	IFN-γ + zymosan	0.78	Phillips and Hamilton, 1989
BMDM	LPS +zymosan	0.38	Phillips and Hamilton, 1989

Abbreviations: PM, peritoneal macrophages; BMDM, bone marrow-derived macrophages; IFN-γ, interferon-γ; LPS, *E. coli* lipopolysaccharide.

Table 1.4. Comparison of reported O_2^- formation rates for murine RAW264.7 macrophages and human monocytes.

Cell Type and Stimuli	O_2^- formation $\left(\frac{pmol}{s \cdot 10^6 cells}\right)$	**Reference**
Human monocyte + PMA	0.35	Johnston, et al., 1976
RAW264.7 + IFN-γ + LPS	0.05	deRojas-Walker, et al., 1995
RAW264.7 + IFN-γ + LPS	2.9	Lewis, et al., 1995
RAW264.7 + IFN-γ + LPS	0.3	Chen and Deen, 2002
RAW264.7 + IFN-γ + LPS	0.33	Nalwaya and Deen, 2005
RAW264.7 + IFN-γ + LPS	0.3	Kim and Wogan, 2006
RAW264.7	0.5	Brune et al., 1997
RAW264.7 + IFN-γ + LPS	1.33	Brune et al., 1997

Exposure to zymosan and PMA generates a heightened O_2^- response in PM and bone marrow-derived macrophages (BMDM). The generation of O_2^- can also be elicited by pre-exposing BMDM to certain cytokines, including granulocyte-macrophage colony stimulating factor (GM-CSF), TNF-α, IFN-γ, bacterial LPS, and, to a lesser extent, IL-lα prior to exposure to zymosan [Phillips and Hamilton, 1988]. The rates of superoxide synthesis in these studies are listed in Table 1.3, along with formation rates measured for murine macrophage cell lines (J774.1, PU5-1.9, and P388D1) and human monocytes. From Table 1.3, it is seen that the superoxide synthesis rates for human monocytes, murine peritoneal macrophages and bone marrow-derived macrophages are all within the same order of magnitude. The rates of superoxide synthesis for RAW264.7 cells, quantified on a pmol/s/10^6 cell basis, are listed in Table 1.4. In these studies, activation was achieved by stimulating macrophages with IFN-γ and LPS; the variations in earlier reported rates [Lewis, et al., 1995; Brune et al., 1997], spanning 2 orders of magnitude, may be attributed to variations in cell culture media. In particular, riboflavin (under laboratory lighting) and HEPES buffer, two ingredients in media, are known producers of superoxide [Keynes, et al., 2003]. Interestingly, the other reported rates of superoxide synthesis by Chen and Deen (2002), Nalwaya and Deen (2005), and Kim and Wogan (2006), ~0.3 pmol/s/10^6 cells, are in good agreement with superoxide synthesis rates reported for primary human monocytes.

1.6. Objectives

Despite numerous models for NO in vascular or neural contexts, none existed for iNOS-produced NO and the concentrations of NO in tissue during infection or inflammation remained unknown. In particular, nitric oxide production has been linked to inflammatory bowel disease (IBD) and increased risk for cancer in the colon, where measurements of NO concentration pose significant technical challenges, and it is unclear what NO levels are pathophysiological. Consequently, the first objective of this thesis was to develop a model to predict NO concentrations in the colonic crypts during inflammation. As presented in Chapter 2, a computational approach, based on anatomical length scales and rates of NO production measured in cell cultures, was used to predict NO concentration profiles for a variety of scenarios within the crypt during inflammation.

The second objective was to characterize NO, O_2, and O_2^- production and consumption rates for a macrophage cell line, primary macrophages and colonic epithelial cells, as described in Chapter 3. These kinetic rates are critical parameters for modeling NO concentrations in tissue during inflammation and are also useful for predicting intracellular levels of other reactive nitrogen species that may contribute to cytotoxicity and mutagenesis. Although the rates of NO synthesis and consumption for RAW264.7 cells are known [Nalwaya and Deen, 2005], there may be differences between the murine macrophage-like cell line and primary macrophages. Significant variations in reported NO synthesis rates by colonic epithelial cells also warranted further characterization of their kinetic rates.

The third objective, described in Chapter 4, involved characterization of cellular kinetic rates and NO concentration predictions in a different disease – melanoma. The presence of iNOS and nitrotyrosine in human metastatic melanoma tumors has been correlated with poor survival rates in patients but the concentrations of NO that melanoma cells produce and are exposed to *in vivo* remains unknown. Although it has been shown that A375 and MeWo melanoma cells express iNOS *in vitro* [Zheng et al., 2004], it remains unclear whether or not the cells actually produce measurable levels of NO and the rates of NO consumption have not been reported. NO kinetic rates in melanoma cells were determined by monitoring NO concentrations in a closed chamber apparatus, like that employed for macrophage and epithelial cells studies, and were subsequently incorporated into a model that predicts NO concentrations in a cutaneous metastatic melanoma.

Chapter 2. Predicting Nitric Oxide Concentrations in the Colonic Crypt During Inflammation

2.1. Introduction

The relationship between the chronic inflammation of inflammatory bowel disease and colon cancer has been demonstrated directly in experimental animals; for example, *Citrobacter rodentium* infections produce lesions similar to those of IBD and have been shown to promote colonic adenomas in lines of targeted gene mutant mice [Newman et al, 2001]. Although the precise etiology of IBD remains to be elucidated, there is a growing body of both experimental and clinical evidence that links chronic gut inflammation with enhanced production of nitric oxide. Evidence for increased synthesis of NO has been reported in patients with active ulcerative colitis, with either increased inducible nitric oxide synthase (iNOS) activity [Boughton-Smith et al, 1993; Lundberg et al, 1994; Middleton et al, 1993] or increased intestinal luminal NO concentrations [Herulf et al, 1998]. Thus, NO generated by iNOS activity is likely to contribute to the increased vascular permeability and tissue injury seen in active IBD. This is just one example of a more general linkage between chronic inflammation, sustained NO overproduction, and various forms of cancer, and several pathways for NO-induced damage to tissue cells have been proposed as possible mediators [Tamir and Tannenbaum, 1996]. Among the most likely damaging agents are reactive nitrogen species derived from NO, including nitrogen dioxide (NO_2), nitrous anhydride (N_2O_3), and peroxynitrite ($ONOO^-$).

As shown in Figure 2.1, the inner lining of the colon, or mucosa, consists of three distinct layers: the muscularis mucosa, the lamina propria, and the epithelium. The lamina propria forms the connective tissue that surrounds tubular invaginations, known as colonic crypts. Lined with an epithelial layer that is one cell thick, the crypts are filled with intestinal luminal fluid and

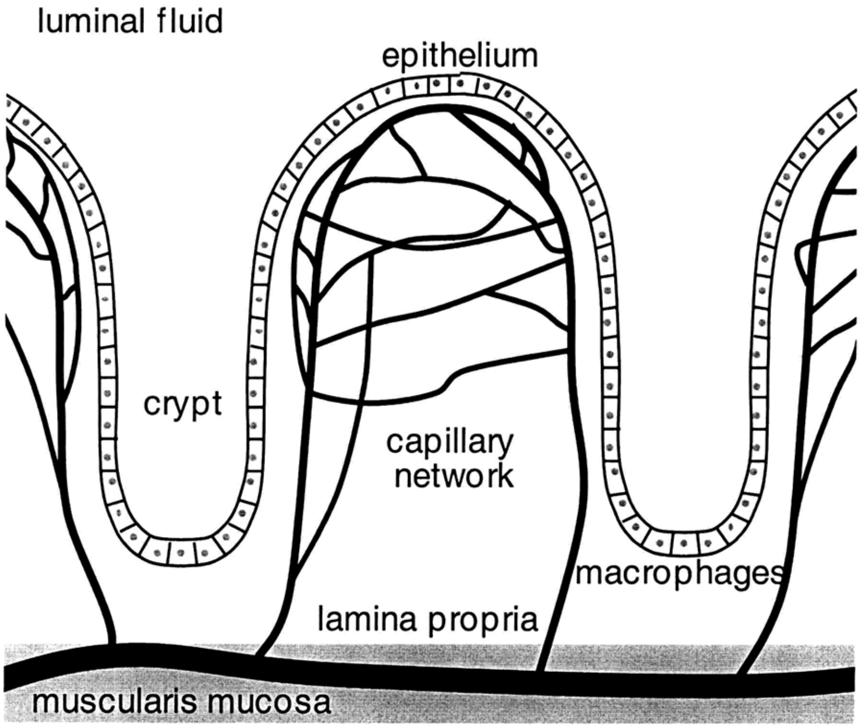

Figure 2.1. Schematic representation of colonic crypt anatomy.

surrounded by an intricate network of blood capillaries. Under normal circumstances, intraluminal microbes do not elicit an inflammatory response, but rather coexist with the epithelium. During an infection, however, macrophages migrate to the sites of microbial invasion as part of the immune response, where the NO they synthesize may assist in killing the invading microorganisms. Thus, macrophage populations are distributed within the mucosa [Pull et al, 2004], as depicted on the right in Figure 2.1. With the onset of IBD, the mucosa becomes inflamed and ulcers may form in the colon. IBD is also associated with increased epithelial permeability to solutes such as ovalbumin and mannitol [Nejdfors et al, 1998]. Immunohistochemical staining of samples taken from patients with active ulcerative colitis show that significant iNOS reactivity is localized in the crypt epithelium and in macrophages aggregated around crypt abscesses [Kimura et al, 1998; Singer et al, 1996], suggesting that both cell types are sources of NO.

The apparent linkage between NO and the pathogenesis of IBD notwithstanding, it is unknown what concentrations of NO in the colon are pathophysiological. The same may be said for other inflamed tissues. In the colon and elsewhere, estimates of NO concentration are needed to quantify levels of other potentially damaging reactive nitrogen species and to identify the most likely mechanisms of chemical damage to host cells. The measurement of tissue NO concentrations *in vivo* is technically difficult, so computational models are often the most practical option for estimating NO levels. By describing rates of reaction and diffusion in realistic geometries, NO concentration distributions can be inferred with reasonable confidence. No such models have been available for the colon. Accordingly, we used a computational approach, based on anatomical length scales and rates of NO production measured in cell cultures, to predict NO concentration profiles within a colonic crypt during inflammation. A variety of scenarios were considered, including a range of possible macrophage and epithelial synthesis rates for NO and various spatial distributions of macrophages.

2.2. Model Formulation

2.2.1. Geometric Assumptions

The model was based on a single murine colonic crypt, which was approximated as the axisymmetric structure shown in Figure 2.2. Intestinal luminal fluid or mucus (volume V_1) is surrounded by an epithelial cell layer (V_2). A layer of macrophages lines the bottom of the crypt (V_4). The entire region is bounded on the side and bottom by blood vessels (surfaces S_4 and S_5). The spaces between the epithelium and crypt capillaries, and between the macrophage layer and blood vessels of the muscularis mucosa, represent lamina propria tissue (V_3 and V_5, respectively). The surfaces S_1 (luminal fluid), S_2 (epithelium), and S_3 (lamina propria) define the top of the crypt.

The epithelium is assumed to be one cell thick [Singer et al, 1996], with cells having an average diameter of 5μm [Lipkin, 1985]. In addition, the radial distance from the center of the crypt to the surrounding capillaries is approximately 45 μm [McLaren et al, 2002], as seen in rats. Assuming the same relative dimensions as those in humans [Araki et al, 1996], the vertical extent of these capillaries was estimated to be roughly 125 μm, which gives a distance of 25 μm between the bottom of the crypt and the blood vessels of the submucosa. The macrophages are approximated as a monolayer of cells, with average diameters of 15 μm [Leskovar et al, 2000] . These assumptions, along with known murine colonic crypt widths (15 μm) [Paulsen et al, 2000] and depths (100 μm) [Drucker et al, 1999] were used to calculate the six anatomical dimensions (three radii and three layer thicknesses) listed in Table 2.1.

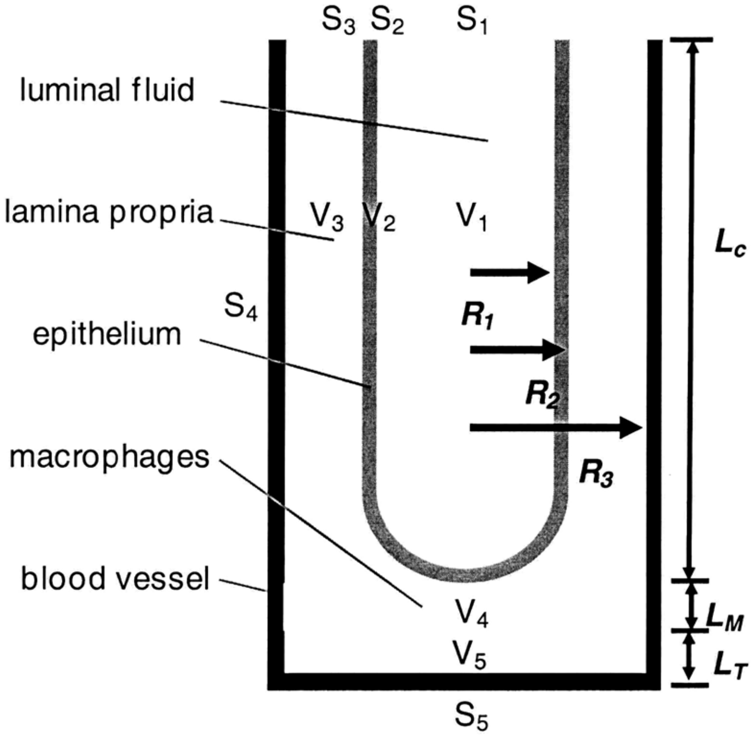

Figure 2.2. Geometrical representation of colonic crypt used in model.

Table 2.1. Linear Dimensions for Murine Colonic Crypt

Variable	**Value**
R_1	15 μm
R_2	20 μm
R_3	45 μm
L_C	100 μm
L_M	15 μm
L_T	10 μm

2.2.2. Reactions of Nitric Oxide in Tissues

The main source of NO in IBD was presumed to be iNOS in the macrophages and epithelial cells. NO production by endothelial cells was assumed to be negligible. Once synthesized, NO diffuses out of the cells, because the cell membrane permeability to NO is very high, similar to that of O_2 [Subczynski et al, 1996]. The following reactions determine the subsequent fate of NO: autoxidation, intracellular consumption, and oxidation by oxyhemoglobin.

The uncatalyzed reaction of NO with molecular oxygen, termed "autoxidation," yields nitrite (NO_2^-) as the end product, with NO_2 and N_2O_3 formed as intermediates [Lewis et al, 1995]. The overall stoichiometry of this multi-step oxidation is

$$4NO + O_2 + 2H_2O \longrightarrow 4NO_2^- + 4H^+ . \qquad (2.1)$$

This reaction will occur both within cells and in extracellular spaces such as intestinal luminal fluid. However, as will be shown, it is too slow to have a significant effect on NO concentrations in intestinal crypts.

Various pathways exist for the intracellular consumption of NO. One involves its rapid reaction with superoxide (O_2^-) to form $ONOO^-$ and (mainly) nitrate (NO_3^-) [Huie and Padmaja, 1993; Ischiropoulos et al, 1992]:

$$NO + O_2^- \rightarrow ONOO^- \xrightarrow{CO_2} NO_3^- . \qquad (2.2)$$

Because O_2^- is a byproduct of respiration and Reaction 2.2 is fast enough to compete with superoxide dismutase, it is expected to occur in virtually all cells. In addition, NO may be consumed via enzymatic pathways. For instance, NO dioxygenase (NOD) is responsible for the oxidation of NO to NO_3^- in certain mammalian cells [Gardner et al, 2000]. NO may also react with oxygen-ligated reduced metals to produce NO_3^- and the oxidized metal [Eich et al, 1996].

Measurements of NO consumption by rat hepatocytes indicate that the overall intracellular NO consumption rate via these various mechanisms can be modeled as being first order in NO concentration [Thomas et al, 2001].

It should be noted that Reaction 2.2 also leads to a certain amount of extracellular consumption of NO. That is, while synthesizing NO via iNOS, activated macrophages also steadily generate extracellular O_2^-, due to a membrane-bound NADPH oxidase [Lewis et al, 1995; Chen and Deen, 2002; Nalwaya and Deen, 2005]. Accordingly, near an activated macrophage, some NO will be converted to $ONOO^-$. However, the diffusion-limited kinetics of Reaction 2.2, together with the fact that NO production exceeds extracellular O_2^- synthesis, makes this an extremely localized process. It has been estimated that the O_2^- produced by a macrophage is fully exhausted within 1 μm of the cell [Chen and Deen, 2002]. Moreover, the rate of O_2^- release into the media by a macrophage has been found to be only 6% of its rate of NO production [Nalwaya and Deen, 2005]. For these reasons, extracellular consumption of NO by O_2^- may be neglected in modeling NO concentrations in crypts.

Any NO that reaches blood vessels is depleted by its very rapid reaction with oxyhemoglobin (HbO_2) to form methemoglobin (metHb) and NO_3^- [Eich et al, 1996]:

$$\mathrm{NO} + \mathrm{HbO_2} \rightarrow \mathrm{metHb} + \mathrm{NO_3^-}. \tag{2.3}$$

Accordingly, capillaries will act as very effective sinks for NO generated within an inflamed tissue.

2.2.3. Conservation Equation for NO

We are concerned with inflammatory processes that persist for weeks or longer. Also, the time required for an epithelial cell to travel from the base to the top of a crypt is 3-8 days in humans and 2-3 days in rodents [Lipkin, 1985]. In contrast, the time required for NO to diffuse over the lengths shown in Table 2.1 is < 1 min. Thus, a steady-state assumption was warranted, and the concentration of NO within each region of the crypt was governed by

$$D_{NO}\nabla^2 C_{NO} + R_{NO} = 0 \qquad \textbf{(2.4)}$$

where C_{NO} is the concentration of NO, D_{NO} is its diffusivity, R_{NO} is its net rate of formation by chemical reaction on a volumetric basis (e.g., mol m^{-3} s^{-1}), and ∇^2 is the Laplacian operator. Equation 2.4 expresses the balance between local rates of production and diffusion of NO, and assumes that the diffusivity is constant within a given region [Deen, 1998]. In subsequent expressions, the diffusivities and concentrations in the luminal fluid (D_{NO}, C_{NO}) are distinguished from those in the epithelium ($\tilde{D}_{NO}, \tilde{C}_{NO}$), the lamina propria tissue ($\hat{D}_{NO}, \hat{C}_{NO}$), and the macrophage layer ($\bar{D}_{NO}, \bar{C}_{NO}$), as needed.

Taking into account NO synthesis and the consumption processes already discussed, the reaction rate for NO is

$$R_{NO} = k_g - k_c C_{NO} - 4k_a C_{NO}{}^2 C_{O_2} \qquad \textbf{(2.5)}$$

where k_g is the generation term (assumed to be constant in a given region), k_c is the overall first-order rate constant for intracellular consumption, and k_a is the rate constant for autoxidation. Implicit in the generation and intracellular consumption terms in Eq. 2.5 is the assumption that O_2 levels are high enough so as not to be limiting. Whereas autoxidation occurs in all the regions defined above, intracellular consumption is absent in the luminal fluid (V_1), and in the baseline model NO synthesis was assumed to be confined to the epithelial and macrophage layers (V_2 and V_4). The reaction of NO with HbO_2 was accounted for in the boundary conditions at S_4 and S_5 (see below), and thus does not appear in Eq. 2.5.

The general governing equations for NO were obtained by using Eq. 2.5 to evaluate the reaction rate in Eq. 2.4. For purposes of simplification and numerical solution, it was advantageous to employ scaled dimensionless concentrations defined as $\theta = C_{NO} / C_{NO}^*$ and $\psi = C_{O_2} / C_{O_2}^*$. The concentration scale for oxygen ($C_{O_2}^*$) is the O_2 concentration in venous blood, whereas that for nitric oxide (C_{NO}^*) was identified as described later. The dimensionless conservation equation was

$$\nabla^2\theta + \left(\frac{k_g L^2}{D_{NO} C_{NO}^*}\right) - \left(\frac{k_c L^2}{D_{NO}}\right)\theta - \frac{4kC_{NO}^* L^2}{D_{NO} C_{O_2}^*}\theta^2\psi = 0 \tag{2.6}$$

where L is the length scale for a particular region (see below). Although the same symbol is used as before, ∇^2 in Eq. 2.6 is now dimensionless (i.e., L^2 times that in Eq. 2.4).

2.2.4. Boundary Conditions

The boundary conditions used in most of the simulations involved specified NO concentrations at all external surfaces. Given the gas-phase intestinal luminal NO concentrations measured in humans (~500 ppb) [Herulf et al, 1998] and the aqueous solubility of NO, the NO concentration in the luminal fluid is ~0.8 nM, which can be considered negligible. Likewise, the fast reaction between NO and HbO_2 [Eich et al, 1996] is expected to yield negligible NO concentrations at the boundaries corresponding to blood vessels. The measured NO concentration in blood plasma is approximately 1-5 nM [Stamler et al, 1992], which is much smaller than the maximum tissue concentrations obtained in our simulations. NO synthesis in endothelial cells may lead to somewhat higher concentrations immediately outside blood vessels, but these have been estimated to be less than 50 nM [Lamkin-Kennerd et al, 2004]. Thus, the endothelial contribution was generally neglected and in most of the calculations the blood vessels were modeled as perfect sinks for NO. Accordingly, the boundary conditions used at each of the surfaces S_1 through S_5 were

$$\theta = 0. \tag{2.7}$$

At all internal boundaries (i.e., where V_1 through V_5 meet one another), the NO concentration and flux were each assumed to be continuous.

2.2.5. Parameter Values

The length scales, diffusivities, and kinetic constants for the regions are discussed now, as their values lead to a significant simplification of Eq. 2.6. The length scales, L, for each of the regions were chosen as the respective radii or layer thicknesses: R_1 for V_1, R_2 - R_1 for V_2, R_3 - R_2 for V_3, L_M for V_4, and L_T for V_5. Each of these lengths was calculated from the dimensions listed in Table 2.1. The other baseline parameter values are given in Table 2.2; unless otherwise stated, all calculations were done using these values. The diffusivity of NO in the luminal fluid was equated with that measured in water [Zacharia and Deen, 2005]. In each of the cellular regions the NO diffusivity was taken to be two-thirds of its aqueous value, which is the intracellular/aqueous diffusivity ratio for O_2 [Ellsworth and Pittman, 1983]. Use of the oxygen diffusivity ratio is justified by the nearly identical diffusional characteristics of NO and O_2 in water [Zacharia and Deen, 2005].

The rates of NO production and consumption for macrophages in Table 2.2 are based on direct measurements in RAW264.7 murine macrophage-like cells activated with recombinant mouse interferon-γ (IFN-γ) and *Escherichia coli* lipopolysaccharide (LPS). Cellular kinetic parameters were determined by monitoring time-dependent NO and O_2 concentrations in a closed chamber and fitting data to a detailed kinetic model [Nalwaya and Deen, 2005]. Reported rates

Table 2.2. Baseline Values of Diffusivities, Rate Constants, and Concentrations

Parameter	**Value**
D_{NO}	3.0×10^{-5} cm^2/s
$\hat{D}_{NO}, \tilde{D}_{NO}, \bar{D}_{NO}$	2.0×10^{-5} cm^2/s
D_{O_2}	2.8×10^{-5} cm^2/s
$\hat{D}_{O_2}, \tilde{D}_{O_2}, \bar{D}_{O_2}$	1.9×10^{-5} cm^2/s
k_a	2.6×10^{6} M^{-2}/s
$\tilde{k}_g$	0.3 μM/s
$\bar{k}_g$	5.6 μM/s
k_c	0.6 s^{-1}
k_r	30 μM/s
C^*_{NO}	0.63 μM
$C^*_{O_2}$	58 μM

of NO production by colonic epithelial cell lines, determined less directly, vary by some two orders of magnitude [Witthoft et al, 1998; Wright et al, 1999]. The value given in Table 2.2 is at the high end of the reported range. Epithelial cell NO synthesis rates were estimated based on data collected by Witthoft et al. (1998), whereby NO production from HT-29 cells was measured 24 hours after stimulation with enteroinvasive *E. coli.* Assuming that all NO was converted to NO_2^- and given that 300 μM of NO_2^- was measured for approximately 10^6 cells in 1 mL of liquid media, a volumetric rate of NO synthesis was calculated. The rates of NO consumption by epithelial and lamina propria cells were assumed to be equivalent to those in macrophages. It has been found, for example, that NO consumption rates in TK6 cells (a human lymphoblastoid cell line) are roughly the same as those in RAW264.7 cells [Nalwaya and Deen, 2005; Wang et al, 2003]. The concentration scale for O_2 corresponds to an average value in venous blood.

Although not used in the calculation of NO concentrations, the intracellular diffusivity of oxygen and the cellular O_2 consumption rates in the crypt are also listed in Table 2.2, and their implications will be discussed later. The intracellular O_2 diffusivity in Table 2.2 corresponds to two-thirds of the aqueous value [Goldstick and Fatt, 1970]. *In vitro* measurements show that oxygen consumption in activated RAW264.7 cells [Nalwaya and Deen, 2005] is similar to rates of consumption in HT-29 colonic epithelial cells [Leschelle et al, 2000]. Moreover, both of these values are approximately equal to the reported average O_2 consumption rate measured for a variety of mammalian cell types (3 nmol/min/10^6 cells) [Ruffieux et al, 1998]. Accordingly, the O_2 consumption rates in the macrophage layer, epithelium, and lamina propria regions are approximated as being equal.

Given that $C_{NO} = 0$ at all external surfaces in the idealized crypt (Eq. 2.7), the concentration scale for NO will be determined primarily by the rate of NO synthesis. Assuming that NO is produced mainly in the macrophage layer, and that NO loss from that layer is largely by diffusion, we set the coefficient of the first reaction term in Eq. 2.6 equal to unity for that region. The result is the value of C_{NO}^* given in Table 2.2. As will be shown, our numerical simulations confirmed that this is a good estimate of the maximum order of magnitude of C_{NO} in the crypt.

2.2.6. Simplified Conservation Equation

The coefficient of the autoxidation term in Eq. 2.6 is a Damköhler number that measures the importance of autoxidation relative to diffusion. It is denoted as

$$\gamma = \frac{4k_a C_{O_2}^* C_{NO}^* L^2}{D_{NO}}. \tag{2.8}$$

It was found that $\gamma << 1$ in each of the five regions, ranging from a minimum of 4.8×10^{-6} in V_2 to 1.2×10^{-4} in V_3. This indicates that autoxidation does not significantly affect the NO concentration in any of the regions. With the autoxidation rate being the only reaction term in Eq. 2.6 that depends on the O_2 concentration, and with that term negligible in all regions, it was unnecessary to compute O_2 concentration variations. That is, it was sufficient to focus on the NO concentration field alone. The simplified conservation equation for NO is

$$\nabla^2 \theta + \alpha - \beta\theta = 0 \tag{2.9}$$

where the remaining Damköhler numbers (for synthesis and intracellular consumption, respectively) are

$$\alpha = \frac{k_g L^2}{D_{NO} C_{NO}^*} \tag{2.10}$$

$$\beta = \frac{k_c L^2}{D_{NO}}. \tag{2.11}$$

As already mentioned, we identified the NO concentration scale by setting $\alpha = 1$ in the macrophage layer (V_4). Also, the assumed absence of NO generation in the luminal fluid (V_1) and lamina propria (V_3, V_5) implies that $\alpha = 0$ there. In the epithelium (V_2) we calculated that $\alpha = 6.9 \times 10^{-5}$, indicating that for our baseline conditions, epithelial NO synthesis was negligible. This conclusion seems conservative because, as already noted, the epithelial synthesis rate in Table 2.2 is at the high end of reported values. Intracellular NO consumption was found to be of marginal importance for the base case, with β ranging from 0.01 in V_2 to 0.28 in V_3.

Although the synthesis and intracellular consumption terms were sometimes negligible, Eq. 2.9 (with region-specific values of α and β) was used for all four cellular regions. Further simplification of Eq. 2.9 for some regions did not provide any computational benefits. Also, retaining the α and β terms in all regions provided the flexibility to consider hypothetical conditions in which one or both were important, such as with higher assumed rates of epithelial synthesis.

2.2.7. Solution Methods

The geometry depicted in Figure 2.1 was defined in a commercial finite element package (COMSOL v.3.0, Stockholm, Sweden) using the graphical user interface. The nondimensional differential equation (Eq. 2.9), boundary conditions (Eq. 2.7), and parameter values (α and β) were specified for each subdomain. The system of equations was solved in the 'Diffusion' multiphysics application mode using a linear solver (UMFPACK) and the default settings. The initial mesh plus one mesh refinement, generating 5316 elements, was found to be adequate; additional refinement to 21,264 elements led to a change of less than 0.01% in the NO concentration values.

To verify the accuracy of the finite element results, a simplified model was solved analytically using an eigenfunction expansion. For this purpose, the crypt geometry was simplified by reducing it to a cylinder with a layer of macrophages at the bottom; the dimensions (crypt radius, crypt depth, macrophage layer thickness) were the same as those listed in Table 2.1. Assuming the analytical results to be exact, the norm of the relative error in the numerical solutions was calculated for this simplified model. This relative error was found to be < 0.4%, indicating that the solution generated by COMSOL was satisfactory.

2.3. Results

2.3.1. NO Concentration Profiles

Figure 2.3 shows NO concentrations as a function of height at three radial positions, as calculated with the baseline model parameters. In this and subsequent plots, z is height relative to the top of the macrophage layer; thus, $z = 0$ at the base of the crypt and $z = L_C$ at the top. The radial positions $r = 0$, 18, and 32 μm correspond to the center of the luminal fluid, the middle of the epithelium, and the middle of the lamina propria region (V_3), respectively. As shown, the predicted NO concentration at each radial position declines rapidly in going from the base of the crypt to the top, the maximum concentration (at $r = 0$ and $z = 0$) being 0.29 μM. Most of the NO generated at the base of the crypt diffuses away radially (into the crypt capillaries) or is consumed by cells in the lamina propria. Thus, at $z = 50$ μm, or halfway up the crypt, there is more than a 90% reduction in the NO concentration. The concentration calculated for the epithelium is very similar to that in the luminal fluid. This is a consequence of the rates of NO synthesis and consumption in the epithelium being negligible. Concentrations in the lamina propria are lowest, because of the NO consumption there and in the blood vessels at S_4.

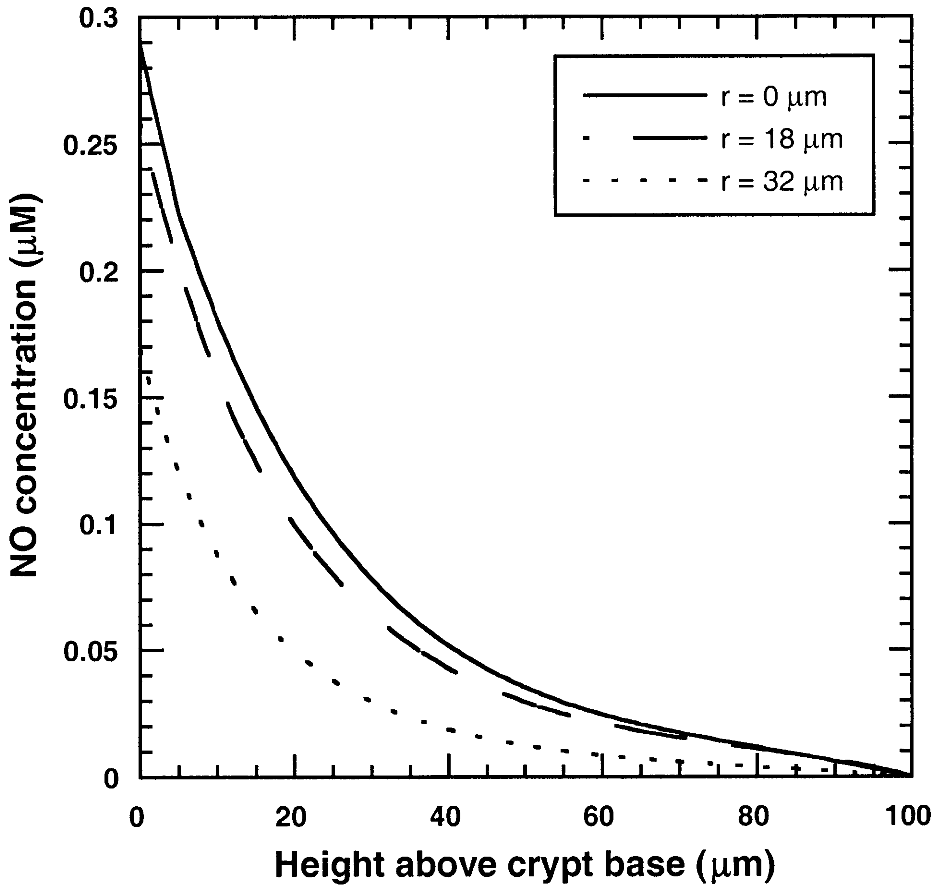

Figure 2.3. NO concentration as a function of height above crypt base (*z*) for baseline model. Axial concentration variations are shown for radial positions r = 0, 18, and 32 μm, which correspond to the center of the luminal fluid, middle of the epithelium, and middle of the lamina propria region, respectively. The calculations employed the baseline parameter values listed in Tables 2.1 and 2.2.

2.3.2. Effect of NO Synthesis Rate of Epithelial Cells

Although the baseline rate of NO synthesis in epithelial cells is a conservatively high value from cell lines *in vitro*, it is conceivable that the rate *in vivo* is much larger. Figure 2.4 shows results obtained by assuming that the rate of NO synthesis per unit volume in epithelial cells equals the baseline rate for macrophages. The arrangement of the plot is the same as in Figure 2.3. The maximum NO concentration in Figure 2.4 is 0.42 μM, a 45% increase from that under baseline conditions. However, the most notable difference from Figure 2.3 is the sigmoidal shape of the concentration profiles for the luminal fluid and epithelium, leading to much higher concentrations in the upper two-thirds of the crypt. The elevated concentrations in the upper part of the crypt in Figure 2.4 reflect the fact that there is now a significant source of NO throughout the crypt length.

2.3.3. Effect of Macrophage Spatial Distribution

In the baseline model, the main source of NO was assumed to be a confluent monolayer of macrophages localized in the region below the crypt base, as suggested by immunohistochemical stains of *Citrobacter rodentium* infection models in mice [Sohn, 2005]. However, similar staining of colons in other infection models in animals has shown macrophage infiltration into the lamina propria as well [Berg et al, 1996; Leithauser et al, 2001]. Accordingly, additional scenarios were considered. In a second model, the macrophages were assumed to be distributed homogeneously throughout regions V_3, V_4, and V_5; as there was no longer a macrophage monolayer, these three regions were assigned identical properties. To maintain the same total rate of macrophage NO synthesis, the source term was evaluated as

$$\hat{k}_g = \frac{\bar{k}_g V_4}{V_3 + V_4 + V_5} \tag{2.12}$$

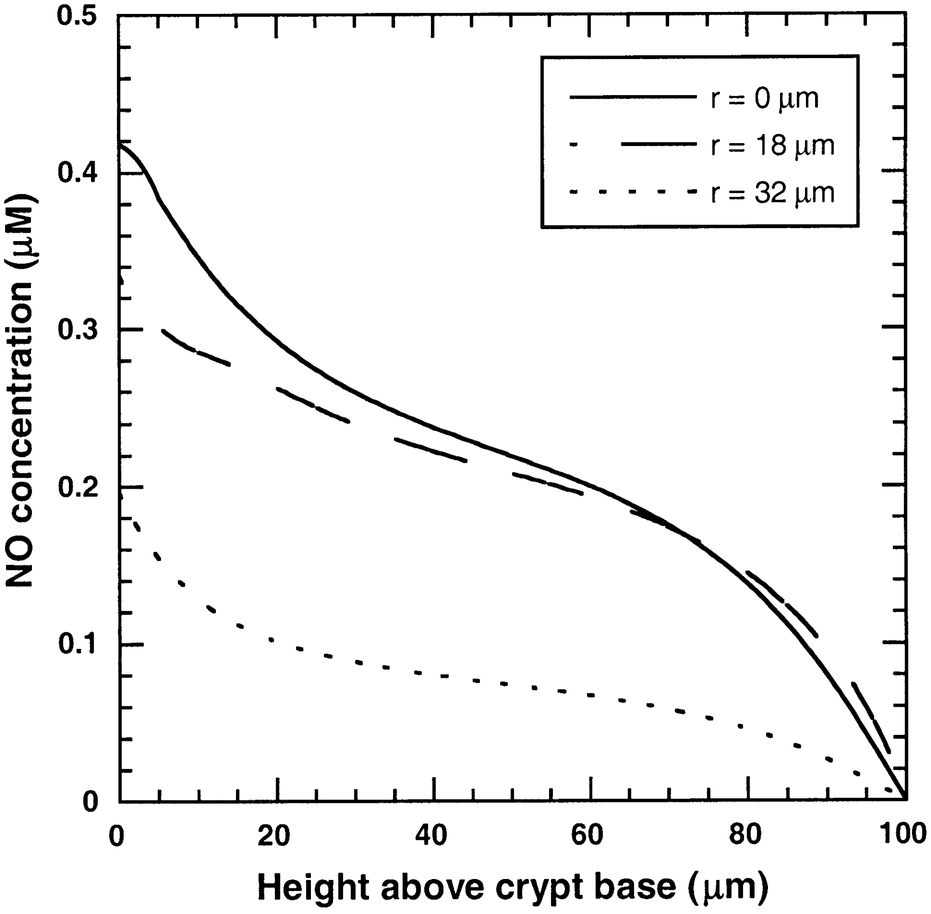

Figure 2.4. NO concentration as a function of height above crypt base for a high rate of NO synthesis in the epithelium. Axial concentration profiles are shown for the same radial positions as in Figure 2.3. The NO synthesis rate per unit volume in epithelial cells was assumed here to be 5.6 μM/s, the same as the baseline rate for macrophages.

where $\hat{k}_g$ is the rate assigned in the new model to volumes V_3 through V_5, and $\bar{k}_g$ is the baseline rate for V_4. In a third model, there was both a macrophage monolayer in V_4 and macrophages distributed throughout V_3 and V_5. In this composite model, it was assumed that the total number of macrophages was twice that in either of the first two scenarios, thereby doubling the overall rate of NO synthesis.

Concentration profiles for the three macrophage arrangements (monolayer, distributed, and monolayer + distributed) are shown in Figure 2.5. Axial variations in NO concentration are depicted once again, but now only for $r = 0$. In comparing the results for the monolayer (baseline) and distributed models, the most striking difference is that the maximum concentration in the latter is only 10% of that in the former. Distributing macrophages throughout the lamina propria is seen to yield a much more uniform NO concentration than in the monolayer model, and slightly higher values in the upper third of the crypt, but the concentrations never exceed 0.03 μM. This indicates that activated macrophages must be spatially concentrated to produce high local concentrations of NO. The NO concentrations in the third (monolayer + distributed) model are, of course, higher than in the other models, because of the increased total rate of synthesis.

The point that macrophages must be co-localized to produce high NO concentrations is further illustrated by calculations done for a simpler situation. In this case we supposed that a spherical macrophage aggregate of radius R was surrounded by an indefinitely large volume of lamina propria tissue. Equation 2.9 was applied to both the macrophage aggregate and the surrounding tissue, with NO synthesis being confined to the former. The NO concentration far from the aggregate was assumed to vanish, due to outward diffusion and to consumption in the

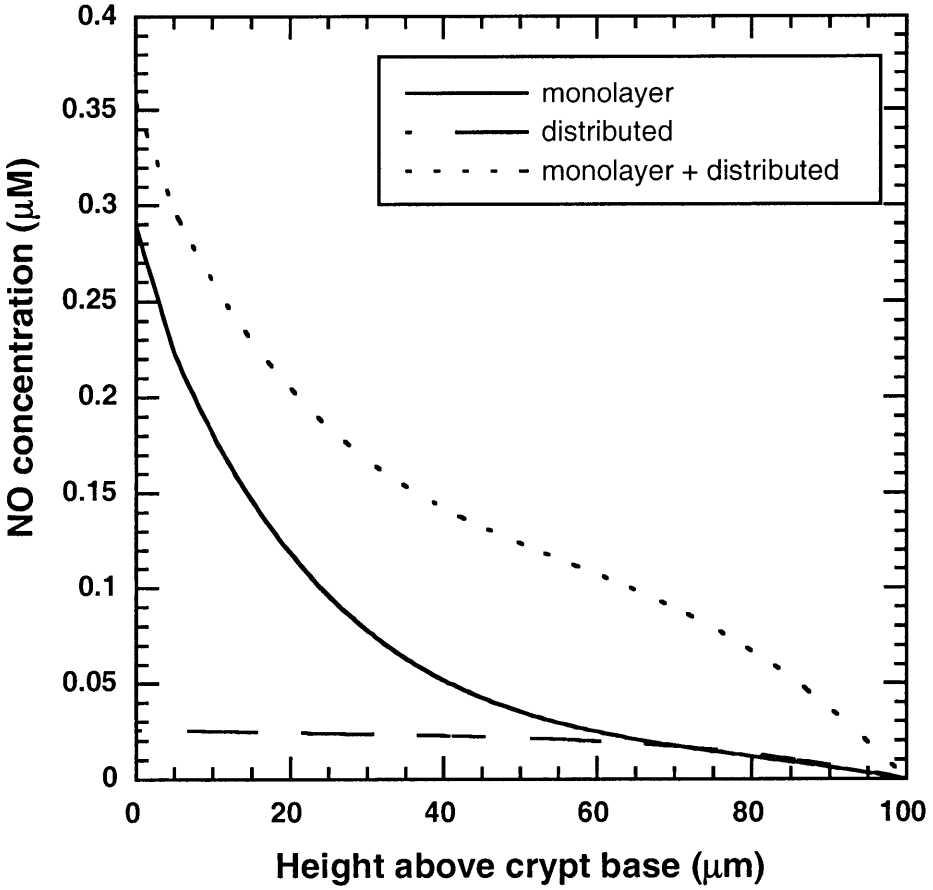

Figure 2.5. NO concentration as a function of height above crypt base for various spatial distributions of macrophages. All results here are for the center of the luminal fluid ($r = 0$). The "monolayer" model used the baseline parameter values; the "distributed" model had no macrophage monolayer and assumed a rate of NO synthesis in the lamina propria regions of $\hat{k}_g =$ 0.8 μM/s; the "monolayer + distributed" model assumed that $\bar{k}_g = 5.6$ μM/s and $\hat{k}_g = 0.9$ μM/s for the macrophage monolayer and lamina propria regions, respectively.

lamina propria cells. An analytical expression was derived for the NO concentration as a function of the radial distance from the aggregate center (r), as given in Appendix A.

Results based on the macrophage aggregate model are shown in Figure 2.6, which depicts concentration profiles for $R = 7.5$, 15, and 22.5 μm. For an isolated macrophage ($R = 7.5$ μm), the maximum NO concentration (at the cell center) was only 0.07 μM for the synthesis rates we employed (Table 2.2). Doubling the aggregate radius (corresponding to 8 tightly packed cells) more than tripled the maximum concentration, to 0.26 μM. Tripling the aggregate radius (corresponding to 27 cells) increased the maximum concentration further, to 0.55 μM. Although higher concentrations might be obtained in theory, there are practical limits on the sizes of hypothetical macrophage aggregates. In our crypt model, for instance, the radius of such an aggregate could not exceed 25 μm, the thickness of the lamina propria region. In addition to limitations in aggregate size, other factors would mitigate against further increases in NO concentration. That is, the larger an aggregate, the more likely it is to be near a blood vessel that is a sink for NO. Moreover, the larger an aggregate, the more prominent is NO consumption relative to diffusion, all other factors being equal. Overall, with synthesis rates as measured in RAW264.7 cells, tissue NO concentrations greater than about 1 μM seem very unlikely, no matter how the macrophages are distributed.

2.3.4. Effect of NO Synthesis Rate of Macrophages

The macrophage NO synthesis rate used in the baseline model ($\bar{k}_g$, Table 2.2) is that measured for murine macrophage-like RAW264.7 cells, which have been shown to synthesize NO_2^- and NO_3^- at rates similar to those of primary macrophages [Stuehr and Marletta, 1987]. Nevertheless, there is uncertainty in the NO generation rate of macrophages *in vivo*. The effect

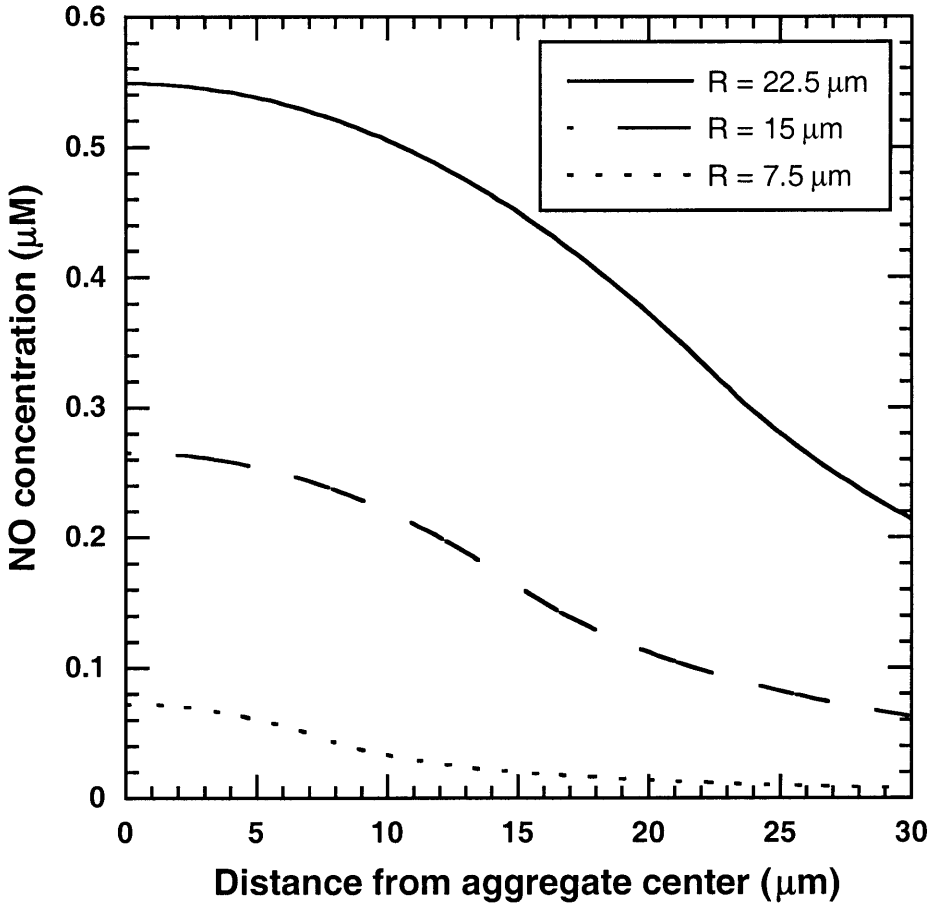

Figure 2.6. Radial NO concentration profiles for hypothetical macrophage aggregates surrounded by lamina propria tissue. Results are shown for macrophage aggregates with radii of 7.5, 15 and 22.5 μm. The calculations were based on macrophage synthesis and cellular consumption rates of $\bar{k}_g$ = 5.6 μM/s and k_c = 0.6 s^{-1}, respectively.

of varying the macrophage NO synthesis rate was simulated for three different cases: the macrophage monolayer (baseline) model, the "monolayer + distributed" model introduced in Figure 2.5, and a scenario in which there is also epithelial synthesis at the same volumetric rate as in the macrophages. In this third case, termed the "monolayer + distributed + epithelium" model, there are three crypt regions synthesizing significant amounts of NO: a layer of macrophages at the crypt base, macrophages distributed in the lamina propria regions, and the epithelial cells.

Figure 2.7 shows maximum NO concentrations in the crypt for each of the three models just described, as a function of the NO synthesis rate. In each case the maximum NO concentration increases linearly with the rate of NO synthesis, which is a consequence of having a linear differential equation with one source term (α in Eq. 2.9) in each region. The macrophage NO synthesis rate in Table 2.2 ($\bar{k}_g$ = 5.6 μM/s) results in maximum NO concentrations of 0.29 μM, 0.35 μM, 0.48 μM, respectively, in the three models. For the NO concentration to exceed 1.0 μM in each of the models, the NO synthesis rates by macrophages must be greater than approximately 20 μM/s, 16 μM/s, and 12 μM/s, respectively. We conclude that, even if tissue macrophages synthesize NO at twice the rate measured with RAW264.7 cells, NO concentrations in the crypt will remain sub-micromolar.

2.3.5. Microvascular Assumptions

The sensitivity of the results to assumptions made about the surrounding blood vessels was examined by comparing the maximum NO concentrations in the epithelium for five situations, as shown in Figure 2.8. Case 1 is the baseline model. In Case 2, the concentrations at S_4 and S_5 were specified as 50 nM (maximum concentration estimated at outside of blood vessels

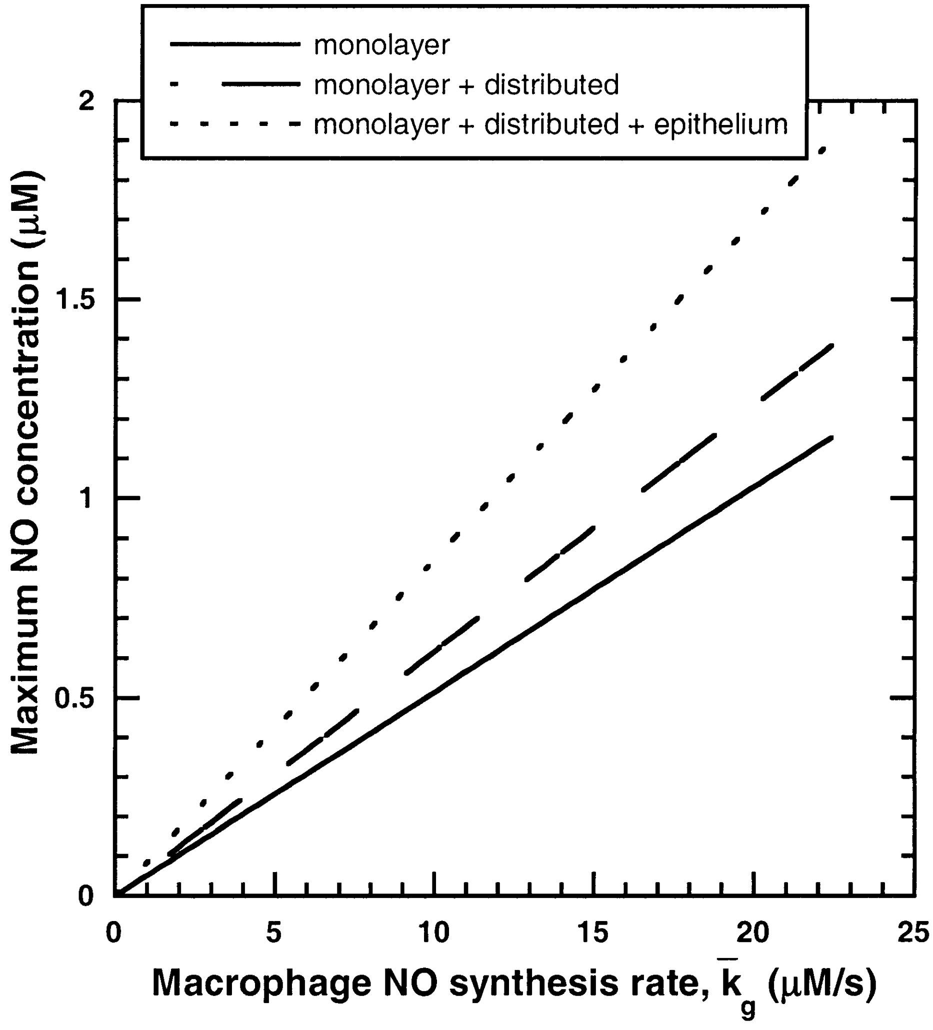

Figure 2.7. Effect of macrophage NO synthesis rate on maximum epithelial NO concentrations for the monolayer (baseline), monolayer + distributed, and monolayer + distributed + epithelium models. The calculations assumed $\bar{k}_g = \hat{k}_g$ in the monolayer + distributed model and $\bar{k}_g = \hat{k}_g = \tilde{k}_g$ in the monolayer + distributed + epithelium model.

[Lamkin-Kennard et al, 2004]), rather than zero. In Case 3, Eq. 2.7 was replaced at surface S_5 by a no-flux boundary condition. This is equivalent to assuming that NO diffusing into the muscularis mucosa encounters a significant resistance (perhaps because the distance L_T is larger than we assumed), and consequently that boundary no longer acts as a sink for NO. In Case 4, R_3 was shortened from 45 to 30 μm, reducing the distance from the epithelial cells to the capillaries from 25 to 10 μm. (It seems unlikely that distance is significantly larger than the baseline value, given that epithelial cells have been reported to be no more than 30 μm from blood vessels in rats [Mohiuddin, 1996]). Case 5 is a composite of the preceding two, with both a no-flux boundary condition at the bottom and capillaries closer to the epithelium.

As seen in Figure 2.8, relaxing the assumption that the NO concentration in blood is zero (Case 2) resulted in a 29% increase in the maximum epithelial NO concentration, relative to the baseline model (Case 1). Eliminating the downward diffusion of NO to S_5 (Case 3) produced a larger (40%) increase, by removing that vascular sink. In contrast, moving the crypt capillaries closer to the epithelium (Case 4) lowered the maximum NO concentration (by 33%), by reducing the resistance to diffusion toward that other sink. Combining the latter two effects (Case 5) gave a result much like that of just repositioning the capillaries, suggesting that the value of R_3 is more crucial than is the boundary condition at the bottom. Overall, we conclude that the results are not highly sensitive to the various simplifications made in representing the microvasculature.

2.4. Discussion

We developed a novel computational model to describe the interplay among the synthesis, consumption, and diffusion of NO in a colonic crypt, and used it to estimate spatially varying NO concentrations during inflammation. Previous models have described NO generated from idealized point sources [Lancaster, 1994; Wood and Garthwaite, 1994], NO diffusion from

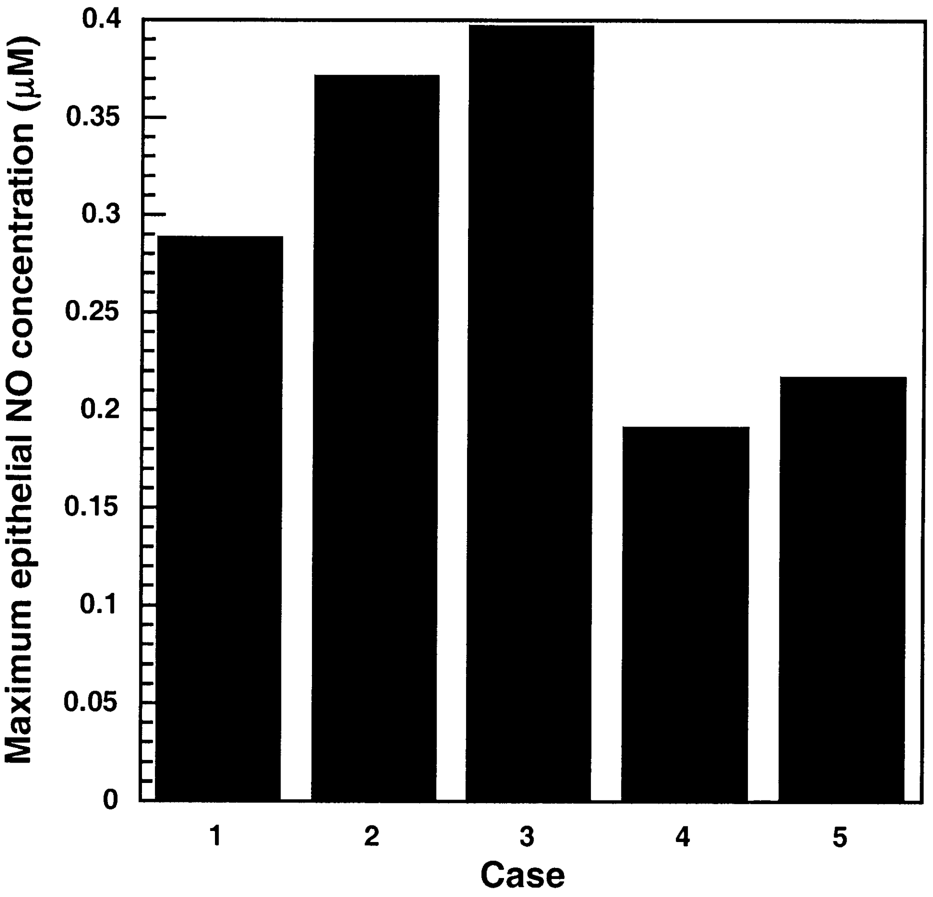

Figure 2.8: Maximum epithelial NO concentrations for several alternative assumptions concerning the crypt microvasculature: Case 1, baseline; Case 2, non-zero (50 nM) NO concentration in blood; Case 3 no-flux boundary condition at the bottom surface (S_5); Case 4, reduced radial distance to capillaries (R_3 = 30 μm); and Case 5, no-flux boundary condition at bottom and R_3 = 30 μm.

spherical neurons in the brain [Phillipides et al, 2000], and NO diffusion from endothelium into surrounding tissue [Vaughn et al, 1998], but this appears to be the first attempt to estimate NO concentrations in any specific, inflamed tissue. The focus here is on colonic crypts, but a similar methodology could be applied to other regions of inflammation. Using known anatomical dimensions and data on the cellular rates of NO synthesis and consumption *in vitro*, we calculated a maximum concentration (near the base of the crypt) of 0.3 μM (Figure 2.3). The results suggest that, under inflammatory conditions, the NO concentration is determined mainly by synthesis in activated macrophages, with epithelial NO synthesis likely to be negligible. Even if epithelial cells were assumed to synthesize NO at rates comparable to macrophages, the NO concentrations in the crypt remained below 0.5 μM (Figure 2.4). Normal NO concentrations, in the absence of inflammation, are unlikely to exceed 50 nM [Lampkin et al, 2004].

We found that, for a colonic crypt, the only important pathways for NO consumption are intracellular reactions (such as with O_2^-, oxygen-ligated metals, and NO dioxygenases) and the reaction with oxyhemoglobin in blood. The reaction of NO with extracellular O_2^- generated by macrophages is expected to be localized to within about 1 μm of the cells, and the rate of O_2^- production is too small for this to be a significant sink for NO [Chen and Deen, 2002; Nalwaya and Deen, 2005]. Likewise, the rate of autoxidation was shown to be negligible in a crypt. This is a consequence mainly of the small length scale, and contrasts with the situation for macrophages cultured on a flat plate covered with medium. The Damköhler number (γ, Eq. 2.8) that measures the importance of autoxidation relative to diffusion depends on the square of the characteristic linear dimension. Thus, for a plate culture with a medium depth of 2 mm, γ is some 400 times larger than in a crypt with a height of ~0.1 mm. Whereas autoxidation was found to be an important factor in analyzing data from macrophage plate cultures [Chen and Deen, 2005] [Chen and Deen, 2002], it could be safely neglected in the present analysis.

The O_2 concentration distribution within a crypt might affect the NO concentration by altering the rate of autoxidation, the rate of NO consumption by intracellular processes, the rate of NO synthesis by iNOS, or some combination of these. As just discussed, autoxidation was found to be a negligible sink for NO in this setting, and as mentioned earlier in connection with Eq. 2.11, intracellular consumption was of only marginal importance. To assess whether or not O_2 might become limiting in NO synthesis, we approximated the rate of O_2 consumption as a constant. The resulting dimensionless conservation equation for O_2, analogous to Eq. 2.9 for NO, was

$$\nabla^2 \psi - \delta = 0 \qquad \textbf{(2.13)}$$

$$\delta = \frac{k_r L^2}{D_{O_2} C_{O_2}^*} \qquad \textbf{(2.14)}$$

where k_r is the rate of O_2 consumption and δ is the corresponding Damköhler number. Using the values listed in Tables 2.1 and 2.2, δ did not exceed 0.17 in any region of the crypt, indicating that the O_2 concentration will be relatively uniform, as assumed. Indeed, the minimum O_2 concentration calculated within the macrophage layer (V_4) using Eqs. 2.13 and 2.14 was 37.8 μM, or 94.5 % of the venous value. The Michaelis constant for oxygen-dependent production of NO by iNOS has been reported to be around 6 μM; iNOS is the least O_2-sensitive NOS isoform at low pO_2 [Rengasamy and Johns, 1996]. Although there is evidence that inflammatory bowel disease is associated with increased oxygen metabolism and tissue hypoxia [Taylor and Colgan, 2007], to reach concentrations as low as 6 μM the rate of respiration would need to be approximately 9.5 times the value of k_r given in Table 2.2. Thus, it seems unlikely that O_2

availability would be a significant factor in NO synthesis. With O_2 apparently not limiting either NO synthesis or NO consumption, NO concentrations could be calculated without evaluating those for O_2. This provided a valuable simplification in formulating the crypt model.

Simulations based on various spatial distributions of cells showed that macrophages grouped closely together are necessary to elicit maximum NO concentrations as large as those calculated in the baseline, monolayer model (Figure 2.5). This conclusion was reinforced by results obtained from a simplified model, in which a spherical aggregate of macrophages was assumed to be surrounded by tissue cells that do not synthesize NO. It was found that increasing the radius of an aggregate of tightly packed cells markedly increased the maximum concentration of NO, which occurred at the center (Figure 2.6). In reality, the size of any macrophage aggregate will be limited by the physical dimensions of the crypt, and the maximum NO concentration will be reduced by the proximity of the macrophages to blood vessels, which act as NO sinks.

The effect of macrophage distribution on the maximum NO concentration may be helpful in interpreting observations on the temporal progression of IBD. In mice, immunohistochemical stains of colonic tissue taken two weeks after infection with *Citrobacter rodentium* depict localization of macrophages below the crypt base (D.B. Schauer, unpublished observations). However, one month after infection, the number of macrophages increases slightly and macrophage infiltration is observed throughout the lamina propria. Thus the distribution and number of macrophages in the inflamed mucosa may change over time. Our results indicate that even if the number of macrophages increases somewhat, if the macrophages are dispersed throughout the lamina propria, the maximum NO concentrations will be lower than in the baseline scenario (macrophage monolayer). These results suggest that it is the earlier stage of the disease which elicits the highest concentrations of NO and therefore inflicts the most damage on cells.

Colonic epithelial cells originate at the crypt base and migrate to the crypt top over several days. Assuming that this movement is undisturbed by inflammation, a given epithelial cell will experience a wide range of NO concentrations during its lifetime, the concentration decreasing as it ages and migrates upward. Given an NO concentration field computed using the crypt model, and an assumed velocity vector for the cell (**v**), the instantaneous NO concentration and the cumulative NO dose experienced by the cell at time t can be calculated as

$$C_C(t) = C_0 + \int_0^t \mathbf{v} \cdot \nabla C_{NO}\, dt \qquad \textbf{(2.15)}$$

$$M(t) = \int_0^t C_C(t)\, dt \qquad \textbf{(2.16)}$$

In these expressions, C_0 is the initial NO concentration (the value at the base of the crypt), $C_C(t)$ is the concentration in an epithelial cell after it has migrated for a time t, and $M(t)$ is its cumulative dose of NO up to that instant ("area under the curve").

Figure 2.9 shows the NO concentration and dose history calculated from Eqs. 2.15 and 2.16 using results obtained with the baseline (macrophage monolayer) model or the "monolayer + distributed" model (introduced in connection with Figure 2.5). The migration time in each case was assumed to be 4 days. The maximum NO concentration is experienced at $t = 0$, when the epithelial cell is located at the base of the crypt. As the epithelial cell migrates away from the macrophage layer, the concentration that it is exposed to decreases, whereas the cumulative dose increases. By the time the epithelial cell has finished migrating at $t = 96$ hr, it has been exposed

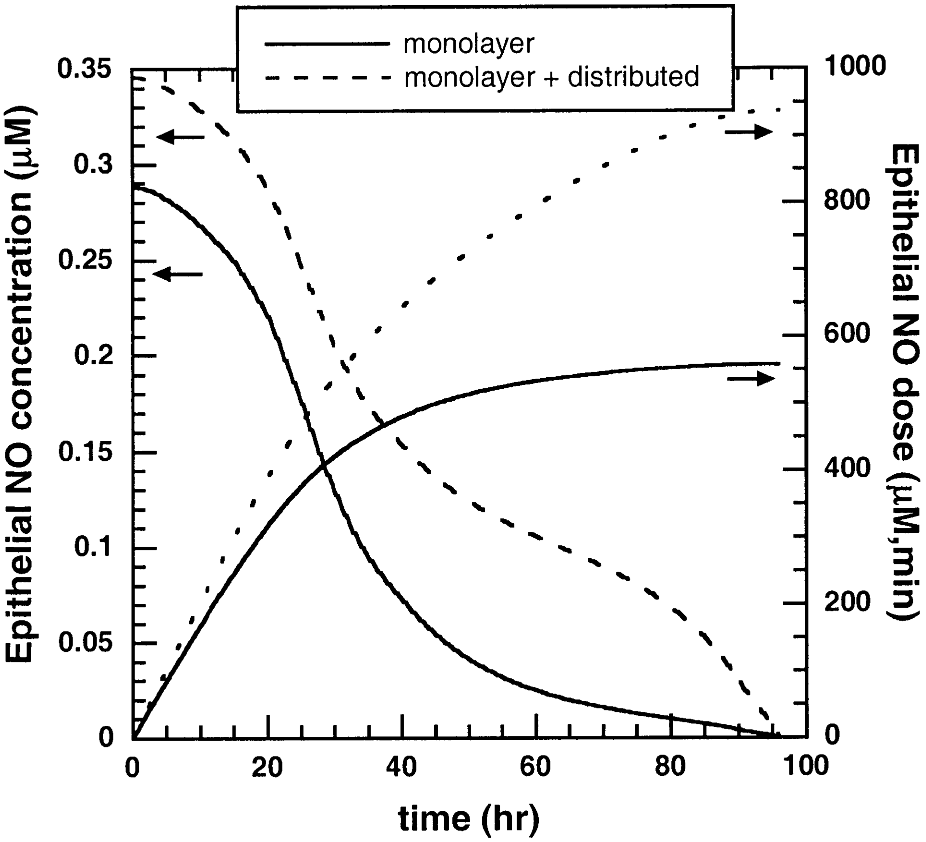

Figure 2.9. Time-dependent NO concentration and cumulative NO dose experienced by an epithelial cell as it migrates from the crypt base to the mucosal surface. The total time for migration was assumed to be 96 hr. Results are shown for the monolayer and monolayer + distributed models.

to doses of 560 μM·min and 940 μM·min in the monolayer and monolayer + distributed models, respectively.

Is the NO exposure depicted in Figure 2.9 toxic? In studies involving carefully controlled exposure to NO over 24 hr, toxicity thresholds for human lymphoblastoid (TK6) cells were found to occur at an NO concentration of 0.5 μM and a dose of 150 μM·min [Thomas et al, 2001; Li et al, 2006]. Both of these thresholds (concentration and dose) had to be exceeded for the number of viable cells to decline in a dose-dependent manner, relative to controls; if neither or just one was exceeded, the cells proliferated normally. Other cell types, including p53-null human lymphoblastoid (NH32), human colon cancer (HCT116), and melanoma cell (A375) lines have been shown to be more resistant to NO [Li et al, 2006; Li et al, 2009]. Even if colonic epithelial cells are as sensitive to NO as TK6 cells, the results in Figure 2.9 suggest that they will remain viable, because even the maximum predicted concentration does not exceed the corresponding threshold. Cell viability is, of course, a prerequisite for mutations leading to oncogene activation or suppressor gene inactivation.

At sub-toxic concentrations comparable to those predicted by our baseline model, NO has been shown to influence specific sets of signal transduction pathways. In breast cancer cells (MCF7) it was found that at steady-state NO concentrations of 0.1 to 0.3 μM, hypoxic inducible factor-1α (HIF-1α) accumulates, and that p53 serine-15 phosphorylation occurs at NO concentrations above 0.3 μM [Thomas et al, 2004]. HIF-1α is associated with tumor proliferation and differentiation. When activated by phosphorylation, p53 regulates the cell cycle through growth arrest or apoptosis; p53 inactivity results in a loss of this protective effect and can lead to tumorigenesis [Thomas et al, 2004]. Thus, depending on concentration and duration of exposure, NO may regulate signal transduction cascades in cancer cells with either tumor-promoting or tumor-suppressing effects.

NO may also be linked to mutational events in the different cell populations within the colonic crypt. In a healthy mucosa, proliferating epithelial cells are predominantly found in the lower two-thirds of the crypt. However, *in vitro* labeling studies for patients with colitis showed that DNA-synthesizing cells are located mainly in the upper third of the crypt, suggesting an upward shift in the proliferation zone [Lipkin, 1974]. Thus, at the concentration and dose levels predicted by our model, exposure to NO and related reactive nitrogen species may initiate a mutagenic change in the population of migrating epithelial cells, allowing them to develop irregular proliferative behavior and additional abnormal properties that enable them to be retained in the mucosa. These dysplastic cells may expand laterally and downwards, eventually displacing the normal crypt epithelium, as hypothesized in 'top-down' models of tumorigenesis in the colon [Shih et al, 2001]. While mutational changes may occur in epithelial daughter cells, it has also been argued that any genetic alteration will be lost in these cells as they will invariably move out of the crypt [Potten and Lowffler, 1990]. Our model predicts that putative stem cells, which remain at or near the base of the crypt, are exposed to the highest concentrations of NO. In contrast to migrating epithelial cells, any oncogenic mutations in the stem cell population could accumulate and persist over time. For instance, alterations in the stem cells could result in dysplastic progeny, eventually giving rise to the formation of dysplastic crypts that continue to divide as the lesions spread from the bottom of the crypt [Preston et al, 2003]. For either scenario of tumorigenesis in the colonic crypts, our model can be used to estimate NO concentrations at which possible mutational events may occur, irrespective of where these genetic changes take place (at the top or the base of the crypt). Thus, although the molecular biological linkage between NO exposure and carcinogenesis in IBD remains unclear, continuing efforts to elucidate the underlying mechanisms should benefit from having estimates of NO concentrations in inflamed crypts.

Chapter 3. Nitric Oxide, Oxygen, and Superoxide Formation and Consumption in Macrophages and Colonic Epithelial Cells

3.1. Introduction

Chronic increases in the rates of endogenous synthesis of NO have been implicated in the development of several human diseases, including cancer [Tamir and Tannenbaum, 1996]. In the gastrointestinal tract, NO or its metabolites have been linked to the pathogenesis of inflammatory bowel diseases (IBD), which often precede colon cancer [Levin, 1993; Farrell and Peppercorn, 2002] . Immunohistochemical staining of samples from patients with active ulcerative colitis show that significant inducible nitric oxide synthase (iNOS) activity is localized in the crypt epithelium and in macrophages aggregated around crypt abscesses [Singer et al., 1996; Kimura, et al., 1998]. However, it remains unknown what concentrations of NO in the colon are pathophysiological. The rates at which macrophages and epithelial cells synthesize NO is critical for predicting NO concentrations in a colonic crypt during inflammation [Chin, et al., 2008], and the levels of NO are needed to estimate the intracellular concentrations of other reactive nitrogen species [Lim, et al., 2008]. Thus, a knowledge of the synthetic capacities of macrophages and epithelial cells is needed to improve the design of experiments to probe the cytotoxic and mutatgenic effects of NO, and thereby clarify the mechanisms by which NO exposure is linked to carcinogenesis in IBD.

Two strategies have been used previously to measure cellular rates of NO production. Usually, the rate of NO synthesis is inferred from the rates of accumulation of stable end products of NO oxidation [Wiffhoft, et al., 1998; Wright, et al., 1999; Chen and Deen, 2002]. In a typical plate culture system (Figure 3.1), NO produced by cells will experience one of four principal fates: consumption by cells, reaction with O_2 in the media to form NO_2^-, reaction with

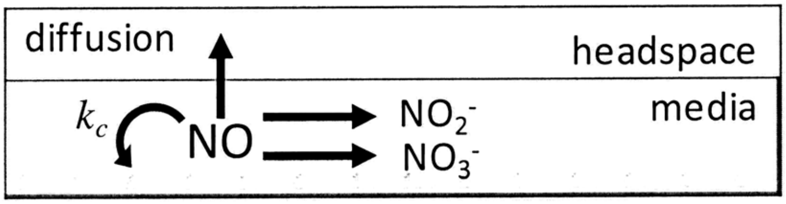

Figure 3.1. The three major fates of NO generated by cells in a typical plate culture experiment: diffusion through the media to the headspace, oxidation to NO_2^- via Reaction 1, or oxidation to NO_3^- via Reaction 2.

O_2^- in the media to form NO_3^-, or escape to the headspace by diffusion. The relatively slow, multistep reaction with O_2, termed autoxidation, is written overall as [Lewis and Deen, 1994].

$$4NO + O_2 \rightarrow 2N_2O_3 \xrightarrow{+2H_2O} 4NO_2^- + 4H^+ . \qquad (3.1)$$

The very fast reaction of NO with O_2^- is [Ischiropoulos, et al., 1992; Huie and Padmaja, 1993]

$$NO + O_2^- \rightarrow ONOO^- \xrightarrow{CO_2} NO_3^- . \qquad (3.2)$$

As indicated, the rearrangement of peroxynitrite ($ONOO^-$) to NO_3^- is catalyzed by CO_2 [Lymar and Hurst, 1996]. In an open system, the extent to which the diffusional loss of NO competes with Reactions 3.1 and 3.2 is determined by the liquid depth and the availability of O_2 and O_2^- in the medium. Extracellular O_2^- is synthesized by macrophages via a membrane-bound NADPH oxidase [Babior, 1984; Berton, et al., 1988], and may also be generated photochemically in culture media [Keynes, et al., 2003]. The fraction of the NO lost to the headspace can be significant, so that using NO_2^- and NO_3^- accumulation rates without correcting for NO loss can greatly underestimate NO production rates [Chen and Deen, 2001]. The second strategy is to continuously monitor NO and O_2 concentrations in a closed chamber [Nalwaya and Deen, 2005]. There is no physical loss of NO in this case, but extracellular Reactions 3.1 and 3.2 still must be considered when calculating cellular rates of NO synthesis. With either approach, separate experiments are needed to quantify extracellular O_2^- production, and the cellular consumption rate for O_2 also must be measured or estimated to obtain reliable results.

Another consideration in measuring rates of NO synthesis is that cells also consume NO. Reaction 3.2 is fast enough to allow NO to compete with superoxide dismutase for O_2^- [Nalwaya and Deen, 2003], so that it will occur to some extent in virtually all cells. Other pathways for intracellular consumption of NO involve nitrogen dioxygenases [Gardner, et al., 2000] and reactions with oxygen-ligated reduced metals [Eich, et al., 1996]. Each of these reaction pathways involves NO oxidation to NO_3^-, so a 1:1 stoichiometry can be assumed for O_2 usage in the intracellular consumption of NO. In NO-producing cells the net rate is the difference between the rates of synthesis and consumption, whereas in other cells there will be consumption only. This motivates experiments to measure NO consumption rates.

Reported here are rates of formation and consumption of NO, O_2, and O_2^- for macrophage-like RAW264.7 cells, primary bone marrow-derived macrophages (BMDM), and HCT116 colonic epithelial cells under simulated inflammatory conditions. A combination of open-system and closed-system experiments was used to determine the rates of NO synthesis. With the former, a diffusion-reaction model was used to correct for NO losses to the headspace, and with the latter a batch reactor model was used to account for the various NO consumption pathways. Cellular rates of O_2 consumption, NO consumption, and O_2^- production were measured in separate experiments. The open-system method with loss corrections and the more direct closed-system method have both been applied previously to RAW264.7 cells [Nalwaya and Deen, 2005], but not to BMDM or HCT116 cells. Inflammatory conditions were simulated either by the addition of cytokines or by infection with *Helicobacter cinaedi*. *H. cinaedi* colonizes the lower bowel of various hosts, inducing intestinal inflammation with a pathology similar to that in human IBD, and has been found to upregulate iNOS expression in the cecum of mice [Shen, et al., 2009]. The NO synthetic capacity of HCT116 cells was tested also by exposing them to resveratrol and capsaicin; resveratrol has been shown to increase NOS expression in human adenoma carcinoma cells (SNU-1) [Holian, et al., 2002] and the injection of capsaicin into Sprague Dawley rats was found to upregulate all three NOS isoforms in the subnucleus caudalis [Lee, et al., 2008]. The cellular kinetic results were combined with a previously described model for NO diffusion and reaction in colonic crypts [Chin, et al., 2008] to provide improved estimates of NO concentrations in inflamed crypts.

3.2. Experimental Methods

3.2.1. Mammalian Cell Culture

Cells of the mouse macrophage-like RAW264.7 line (ATCC No. TIB-71), obtained from the American Type Culture Collection (Rockville, MD), were cultured in Dulbecco's modified Eagle's medium (DMEM) containing L-glutamine supplemented with 100 U/mL penicillin, 100 μg/mL streptomycin, and 10% (v/v) heat-inactivated fetal bovine serum (FBS) (BioWhittaker, Walkersville, MD). Cells of the human colon cancer HCT116 line (ATCC No. CCL-247, courtesy of G. N. Wogan, Department of Biological Engineering, MIT) were cultured in McCoy's 5A medium (BioWhittaker, Walkersville, MD) and supplemented with 10% heat-inactivated FBS and one per cent each of 100 U/mL penicillin and 100 μg/mL streptomycin. All cells were maintained at 37 °C in a humidified 5% CO_2 atmosphere.

3.2.2. Growth of Helicobacter cinaedi

H. cinaedi, obtained from the Culture Collection, University of Göteborg, Sweden (CCUG 18818),were plated from freezing stock onto blood agar plates (Remel, Lenexa, KS). Bacteria were maintained in microaerobic chambers that were evacuated to -20 mm Hg and then equilibrated with a gas mixture consisting of 80% N_2, 10% H_2, and 10% CO_2. After 72 hr, bacteria were gently loosened from the plate, transferred to a shaker flask containing 20 mL of Brucella broth (BD Diagnostics, Franklin Lakes, NJ) with 10% FBS, and grown to log-phase. The concentration of *H. cinaedi* was determined by optical density measurements. Bacterial suspensions were centrifuged at 3000 g for 10 min and resuspended in antibiotic-free McCoy's media with 10% FBS. Cells cultured in antibiotic-free media for at least one week were infected by adding 1 mL of appropriately concentrated bacterial suspensions (see below).

Killed bacteria were prepared by treating the *H. cinaedi* (grown as described above) with 0.5% formalin for 24 h and storing them at 4°C. On the day of the experiment, the formalin-killed bacteria were washed three times with PBS and resuspended in antibiotic-free McCoy's media with 10% FBS.

3.2.3. Isolation of Primary Macrophages

Primary bone-marrow-derived macrophages (BMDM) were isolated from mice as described in Tomczak et al. (2003). Approximately 98% of the cultured cells obtained by this method are macrophages, as assessed by flow cytometry. Briefly, BMDM were obtained from C57/Bl6 mice (Jackson Laboratories, Bar Harbor, ME), two to four months old. After flushing the femurs with cell culture media, single-cell suspensions were incubated on tissue culture plates in bone marrow macrophage medium, consisting of DMEM with 10% fetal bovine serum, 5% horse serum, penicillin 100 U/mL, streptomycin 100 μg/mL, 2 mM L-glutamine, and 10% L cell-conditioned medium. Macrophages were cultured for 5 days before use in experiments and were removed from plates by scraping.

3.2.4. Materials

Additional reagents used include recombinant mouse IFN-γ from R&D Systems (Minneapolis, MN) as well as recombinant human IFN-γ and TNF-α from Invitrogen (Camarillo, CA). Escherichia coli lipopolysaccharide (LPS), bovine erythrocyte superoxide dismutase (SOD), capsaicin, resveratrol, rotenone, cytochrome c from horse heart, HEPES buffer solution (pH 7.4), and trypan blue (4% in saline) were all from Sigma Aldrich (St. Louis, MO). N-methyl-L-arginine monoacetate (NMA) was from CalBiochem Research (Salt Lake City, UT), and beef liver catalase was from Roche Molecular Biochemicals (Indianapolis, IN).

3.2.5. Closed Chamber for Measurement of NO and O_2 Concentrations

The apparatus shown in Figure 3.2, similar to that described in Nalwaya and Deen (2005), was used to continuously monitor NO and O_2 concentrations. A polycarbonate insert equipped with a stirring motor (Instech Laboratories, Plymouth Meeting, PA), NO electrode (World Precision Instruments, Sarasota, FL), and fiberoptic O_2 sensor (Instech Laboratories, Plymouth Meeting, PA) was machined to fit within standard 60 mm polystyrene tissue culture dishes. After assembly, the chamber had a total liquid volume of 8.8 mL. All measurements were conducted in a 37°C warm room in the dark, to eliminate NO consumption by light-sensitive riboflavin-derived O_2^- in the medium.

3.2.6. O_2 Consumption by Unactivated Cells in Closed Chamber

Cells (RAW264.7, BMDM, or HCT116) were detached from stock plates and resuspended in media into a homogeneous suspension through vigorous pipetting. The number of viable cells was determined by trypan blue exclusion. Between 5×10^6 and 8×10^6 cells were plated on 60 mm dishes and allowed to adhere for 2-3 h. To begin an experiment, the medium in a given dish was replaced with 15 mL of DMEM with 25 mM HEPES preheated to 37 °C and the dish was assembled with the closed-chamber insert. The O_2 concentration was then monitored for 20-30 min and the rate of consumption calculated from the slope of the curve.

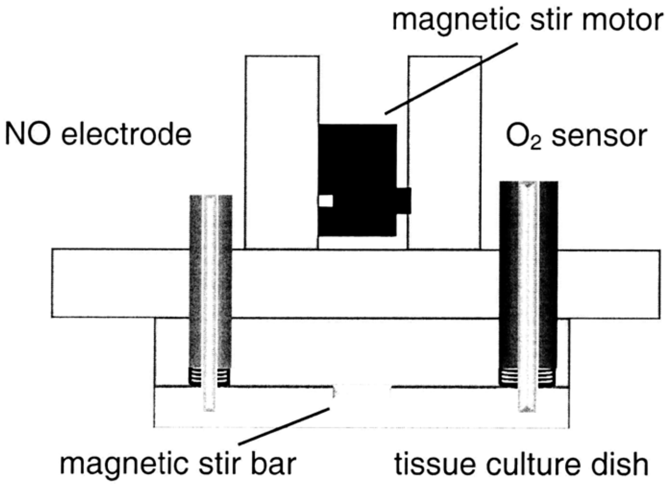

Figure 3.2. Schematic of apparatus used to measure NO and O_2 concentrations in culture media. The polycarbonate insert formed an air-tight seal with a 60 mm tissue culture dish, with adherent cells on the bottom. The enclosed liquid volume was 8.8 mL.

3.2.7. NO Synthesis and O_2 and NO Consumption by Activated Cells in Closed Chamber

Between 5×10^6 and 8×10^6 cells were seeded onto 60 mm dishes. After the cells were allowed to adhere for 2-3 h, the media in plates containing RAW264.7 or BMDM was replaced with fresh DMEM containing LPS (20 ng/mL) and IFN-γ (20 U/mL); HCT116 cultures were replenished with McCoy's media containing capsaicin (100 μM) and resveratrol (50 μM). Because it takes ~6-8 h after the addition of LPS and IFN-γ for macrophages to produce NO [Lewis, et al., 1995], the concentration measurements to determine rates of NO production and consumption for RAW264.7 and BMDM were performed after 12 h. Experiments with HCT116 cells were performed at 24 h after the addition of capsaicin and resveratrol. At the start of each experiment, fresh, preheated media with 25 mM HEPES was added to the dish and the apparatus was sealed. The NO and O_2 concentrations were monitored until a steady NO concentration was achieved, typically 15-20 min. Calculations were done using the kinetic model described below. O_2 concentrations were also monitored for activated RAW264.7 cells in the presence of rotenone, a respiratory inhibitor. After the 12 h stimulation with IFN-γ and LPS, 2 μM of rotenone was added to the media and cells were exposed to the respiratory inhibitor for 1h.

3.2.8. NO Synthesis in Open System

To avoid bacterial contamination of the NO electrode, rates of NO synthesis by RAW264.7 or HCT116 cells infected with *H. cinaedi* were assessed by measuring concentrations of NO_2^- and NO_3^- as a function of time in an open system. The number of viable cells was determined by trypan blue exclusion and cells were seeded at concentrations of 1×10^6 cells/well into 6-well plates. RAW264.7 cells were infected by adding 1 mL of *H. cinaedi* suspension containing either 2×10^7 cells/mL or 2×10^8 cells/mL to each well, giving a multiplicity of infection (MOI, the ratio of bacteria number to mammalian cell number) of 10 or 100, respectively. HCT116 cells were subjected to a pre-treatment of TNF-α (50 ng/mL) and of IFN-γ (100 U/mL) for 24 h prior to infection, and then were infected using the same procedure with either live or killed *H. cinaedi*. The concentration of killed bacteria corresponded to an MOI of 100. Bacteria-free media was added to the control cells (total liquid volume of 2 mL/well).

Supernatant samples (1 sample per well) were collected at 24 and 48 h after infection and centrifuged at 12,000 rpm before analysis. Nitrite and nitrate accumulation was quantified using a Griess assay kit (R&D Systems, Minneapolis, MN). Briefly, 50 μL of culture supernatant was allowed to react with 100 μL of Griess reagent and incubated at room temperature for 10-30 min. For measurement of NO_3^-, NADH and nitrate reductase were added before reaction with the Griess reagents. Absorbance was measured at 540 nm using a microplate reader.

Nitrite and nitrate production was also measured for BMDM and RAW264.7 cells activated with IFN-γ (20 U/mL) and LPS (20 ng/mL). This allowed NO production rates in the open system to be compared with those in the closed chamber. Between 2×10^5 and 4×10^5 macrophages were seeded into each well of a 24-well plate with or without IFN-γ and LPS (total liquid volume of 1 mL/well) and supernatant samples were collected at 0, 4, 8, 12, 24, 36, 48, 60, and 72 hr for Griess analysis.

3.2.9. Superoxide Synthesis

Net cellular O_2^- synthesis of activated and unactivated macrophages was quantified using a cytochrome c assay. After seeding macrophages (RAW264.7 or BMDM) into 24-well plates as described above, 1 mL of media with or without IFN-γ (20 U/mL), LPS (20 ng/mL) was added to each well. NMA (2 mM), an iNOS inhibitor, was added to wells containing macrophages stimulated with IFN-γ and LPS because NO competes very effectively with ferricytochrome c for O_2^- [Deen, et al., 2002]. After stimulation of the macrophages with IFN-γ and LPS for 4 or 8 h, cytochrome c solution (80 μM) was added to the cell supernatant and the mixture was centrifuged at 4000 g for 1 minute. Absorbance at 550 nm was measured on 0.5 mL samples and converted to nanomoles of ferrocytochrome c concentrations using the molar extinction coefficient for the reduction of cytochrome c with ascorbic acid (21.0×10^3 M^{-1} cm^{-1} [Massey, et al., 1959]). Plots of nanomoles of ferrocytochrome c vs. time were fitted linearly. The difference in the slopes between samples incubated with SOD (1000 U/mL) and without SOD was used to calculate the SOD-inhibitable O_2^- production rates for activated and unactivated cells (k_s and k_s^o, respectively).

3.2.10. Model for Closed Chamber

The closed chamber in Figure 3.2 was modeled as a well-stirred batch reactor, as described previously [Nalwaya and Deen, 2005]. The variation in NO concentration (C_{NO}) with time (t) was given by

$$\frac{dC_{NO}}{dt} = \frac{m}{V}\left(k_g - vk_c C_{NO} - k_s\right) - 4k_a C_{NO}^2 C_{O_2} - k_m \qquad \textbf{(3.1)}$$

where m is the number of viable cells, V is the liquid volume, v is the volume of a single cell, (modeled as a hemisphere with radius = 7.5 μm), k_s is the rate of extracellular NO consumption by macrophage-generated O_2^- (which equals the cellular rate of O_2^- synthesis), k_a is the rate constant for autoxidation of NO, and k_m is the rate of extracellular NO consumption by culture medium-generated O_2^-. The values used for V, v, k_a, and k_m are given in Table 3.1. Separate experiments (described above) yielded k_s. The kinetic parameters for NO that were evaluated

Table 3.1. Parameters used in the kinetic model for the closed chamber apparatus and in the reaction-diffusion model for the open system

Parameter	Value	Reference
V	8.8×10^{-3} L	see text
v	8.8×10^{-13} L	see text
a	1.77×10^{-10} m^2	see text
k_a	2.6×10^{6} M^{-2} s^{-1}	[Lewis and Deen, 1994]
k_m	0.4×10^{-9} M s^{-1}	[Nalwaya and Deen, 2005]
K_M	7×10^{-6} M	[Nalwaya and Deen, 2005]
K_I	18×10^{-9} M	[Nalwaya and Deen, 2005]
D_{NO}	3.0×10^{-5} cm^2 s^{-1}	[Zacharia and Deen, 2004]
D_{O_2}	2.8×10^{-5} cm^2 s^{-1}	[Goldstick and Fatt, 1970]
C_O	223 μM	[Chen and Deen, 2002]

Symbols: V, liquid volume in the closed chamber; v, volume of a single cell; a, area of a flat surface occupied by a single cell; k_a, rate constant for autoxidation of NO; k_m, rate of NO consumption by media-generated O_2^-; K_M, the O_2 concentration at which respiration is halved in the absence of NO; K_I, constant describing inhibition of respiration by NO; D_{NO} and D_{O_2}, aqueous diffusivities of NO and O_2 respectively; C_O, liquid-phase O_2 concentration in equilibrium with the incubator.

from the closed-chamber experiments were k_g, the rate of generation of NO, and k_c, the rate constant for intracellular consumption of NO.

The O_2 concentration was described by:

$$\frac{dC_{O_2}}{dt} = -\frac{m}{V}\left[2k_g + vk_c C_{NO} + \frac{R_{\max} C_{O_2}}{C_{O_2} + K_M\left(1 + C_{NO} / K_I\right)}\right] \tag{3.2}$$

The bracketed quantity is the rate of O_2 consumption per cell. The first term is the rate at which O_2 is consumed by iNOS in synthesizing NO, assuming a 2:1 stoichiometry [Stuehr, 1999], and the second term is the rate of O_2 usage during intracellular consumption of NO, with a 1:1 stoichiometry as discussed earlier. In the third term, which corresponds to O_2 consumption from respiration, R_{max} is the maximum rate, K_M is the O_2 concentration at which respiration is halved (in the absence of NO), and K_I accounts for the inhibition of respiration by NO [Brown, 1999]. The one O_2 parameter obtained from the closed-chamber experiments was R_{max}. The values of K_M and K_I used (Table 3.1) were those determined previously from data for RAW264.7 cells [Nalwaya and Deen, 2005]. Because they are intrinsic properties of the respiratory enzymes, they were assumed to be the same for all cells (macrophages and epithelial). In applying Equations 3.3 and 3.4 to NO and O_2 measurements for HCT116 cells, the radius of a single cell was assumed to be the same as that for macrophages [Galle, et al., 2009; Swietach, et al., 2009]. The k_s term was omitted because epithelial cells do not synthesize O_2^- extracellularly (discussed later).

The NO and O_2 kinetic parameters (k_g, k_c, and R_{max}) were calculated by fitting the NO and O_2 concentration data for RAW264.7, BMDM, and HCT116 cells from appropriate sets of experiments; the root-mean-square-difference between the measured concentrations and those predicted by Equations 3.3 and 3.4 was minimized using the simplex method in MATLAB (MathWorks, Natick, MA).

3.2.11. Model for Open System

In the open-system experiments the rate of accumulation of NO_2^- was used to infer cellular rates of NO production for macrophages and epithelial cells. A model like that previously described [Chen and Deen, 2001; Nalwaya and Deen, 2004] was used to account for extracellular reactions, rates of diffusion, and the effects of liquid depth. Because the duration of these experiments was long enough to achieve steady-state levels of NO and O_2, the concentrations were assumed to depend only on height within the liquid (z). In this model the bottom of the well and the gas-liquid interface correspond to $z = 0$ and $z = L$, respectively. The NO concentration in the liquid is governed by

$$D_{NO}\frac{d^2C_{NO}}{dz^2} = 4k_a C^2_{NO} C_{O_2} + k_m \tag{3.3}$$

$$\frac{dC_{NO}}{dz}(0) = -\frac{\alpha}{D_{NO}} N_{NO}(1-\beta) \tag{3.4}$$

$$N_{NO} = \frac{1}{a}\left[k_g - vk_c C_{NO}(0)\right] \tag{3.5}$$

$$C_{NO}(L) = 0 \tag{3.6}$$

The parameters not already defined are: D_{NO}, the diffusivity of NO in water (Table 3.1); α, the fraction of the plate area covered by cells (based on the initial number of cells seeded into a well); β, the ratio of the O_2^- to the NO flux; and N_{NO}, the rate of NO release per unit area from a hypothetical confluent monolayer of cells (units of mol m^{-2} s^{-1}). The cellular flux of NO is equivalent to the net rate of NO synthesis per cell divided by the planar area per cell ($a = \pi r^2$, with $r = 7.5$ μm). The NO consumption rate from media-generated O_2^- (k_m) was assumed to be the same as that used in the closed chamber model (Table 3.1). The value of k_m is determined largely by exposure of the culture medium to light [Nalwaya and Deen, 2005], which was minimal in the open-system experiments and absent in the closed-chamber experiments.

The autoxidation reaction is too slow to have a significant effect on the O_2 concentration [Chen and Deen, 2002], which is given by

$$C_{O_2}(z) = C_0 - \frac{\alpha N_{O_2} L}{D_{O_2}}\left(1 - \frac{z}{L}\right) \tag{3.7}$$

$$N_{O_2} = \frac{1}{a}\left[2k_g + \nu k_c C_{NO} + \frac{R_{\max} C_{O_2}}{C_{O_2} + K_M\left(1 + C_{NO} / K_I\right)}\right] \tag{3.8}$$

Here, C_0 is the liquid-phase O_2 concentration in equilibrium with the incubator (Table 3.1), D_{O_2} is the diffusivity of O_2 (Table 3.1), and N_{O_2} is the rate of O_2 consumption per unit area for a confluent monolayer (units of mol m^{-2} s^{-1}). Similar to the closed chamber model, O_2 consumption in Equation 3.9 includes consumption by iNOS, O_2 usage during intracellular consumption of NO, and competitive inhibition of respiration by NO. The other parameters are as defined for the chamber model. The NO flux and k_g are related by Equation 3.7 and k_c and R_{max} were obtained from the closed-chamber experiments. Thus, the one unknown parameter in this model was N_{NO}.

Equation 3.5 (with Equations 3.6-10) was solved using a commercial finite element package (COMSOL v.3.0, Stockholm, Sweden). Rates of NO_2^- accumulation were calculated by numerically integrating the local rate of NO_2^- formation $\left(\text{given by } 4k_a C_{NO}^2 C_{O_2}\right)$ over the entire solution volume. The value of N_{NO} was adjusted until the fractional difference between the calculated and measured rates of NO_2^- accumulation was $<10^{-6}$.

3.3. Results

3.3.1. Oxygen Consumption by Unactivated Cells

A representative plot of O_2 concentration as a function of time for unactivated BMDM cells in the closed chamber is shown in Figure 3.3. The linear decline implies that the rate of O_2 consumption was constant over the range of concentrations examined. Nearly identical plots were generated for unactivated RAW264.7 and HCT116 cells (Figures 3.4 and 3.5). In each of these experiments NO was undetectable, so that respiratory inhibition was absent. The average rates of O_2 consumption calculated from the slopes of such plots for RAW264.7, BMDM, and HCT116 cells were $R_{max}^{o} = 37.7 \pm 4.3$, 30.2 ± 3.4 and 26.0 ± 6.8 pmol s^{-1} 10^6 cells^{-1}, respectively. As indicated in Table 3.2, oxygen consumption rates for HCT116 cells were not statistically different from those of BMDM, and R_{max} values for BMDM and RAW264.7 cells were also statistically indistinguishable from one another.

3.3.2. NO Synthesis and O_2 and NO Consumption by Activated Cells in Closed Chamber

Figure 3.6 shows NO concentrations in a typical closed-chamber experiment, begun 12 h after stimulation (i.e. addition of IFN-γ and LPS to the media). In this plot, t = 0 is the moment the test chamber was fully assembled and readings were begun. As seen, there was an initial increase in C_{NO} that leveled off at 0.45 μM at ~800 s. At early times (t < ~200 s), when lower concentrations of NO were present, the decline in O_2 concentration was nearly linear. The initial slope for O_2 shown in Figure 3.6 is greater than that observed for unactivated cells (Figure 3.3) and is reflected in the higher rates of oxygen consumption by activated cells (R_{max}, Table 3.2). As NO concentrations increased, the inhibitory effects of NO on respiration were observed, the rate of O_2 consumption gradually decreasing. Similar plots were generated for NO and O_2

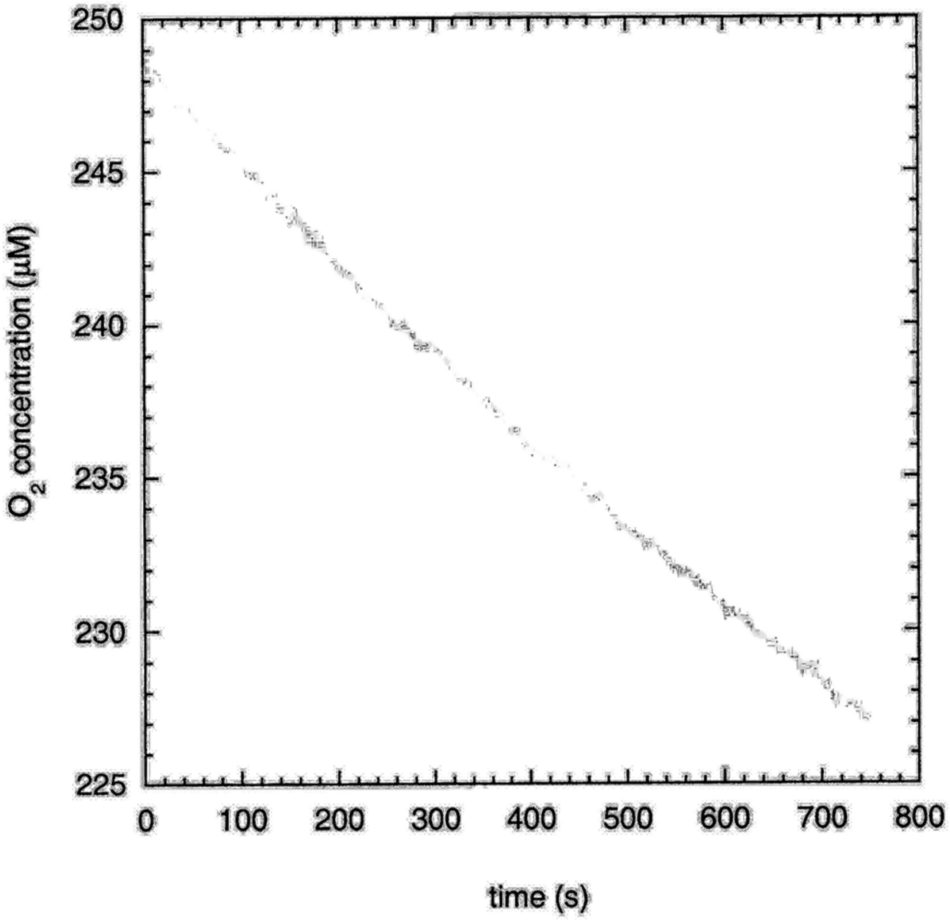

Figure 3.3. Respiration by bone marrow-derived macrophages (BMDM). Shown is a plot of O_2 concentration as a function of time for a representative closed-chamber experiment with 8×10^6 unactivated macrophages. The linear decline in concentration indicates that the rate of O_2 consumption in the absence of NO is constant. Measurements with unactivated RAW264.7 and HCT116 cells resulted in similar plots (not shown).

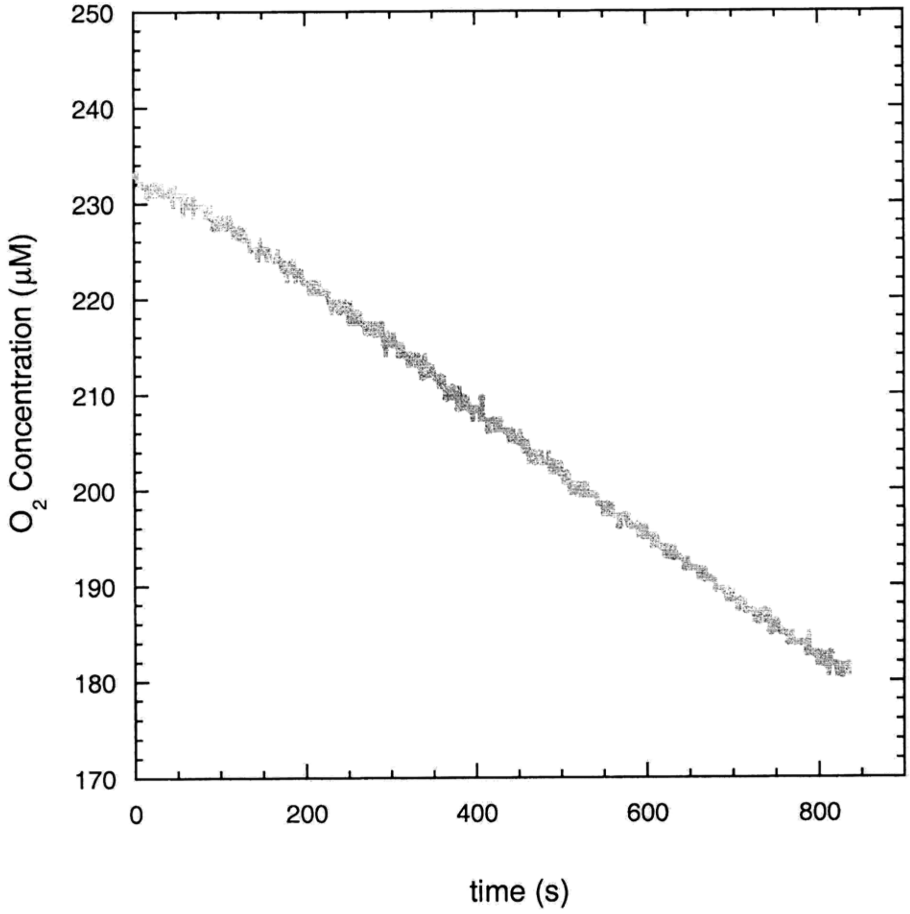

Figure 3.4. Respiration by unactivated RAW246.7 cells (12 $\times 10^6$ cells). Shown is a plot of O_2 concentration as a function of time for a representative closed-chamber experiment.

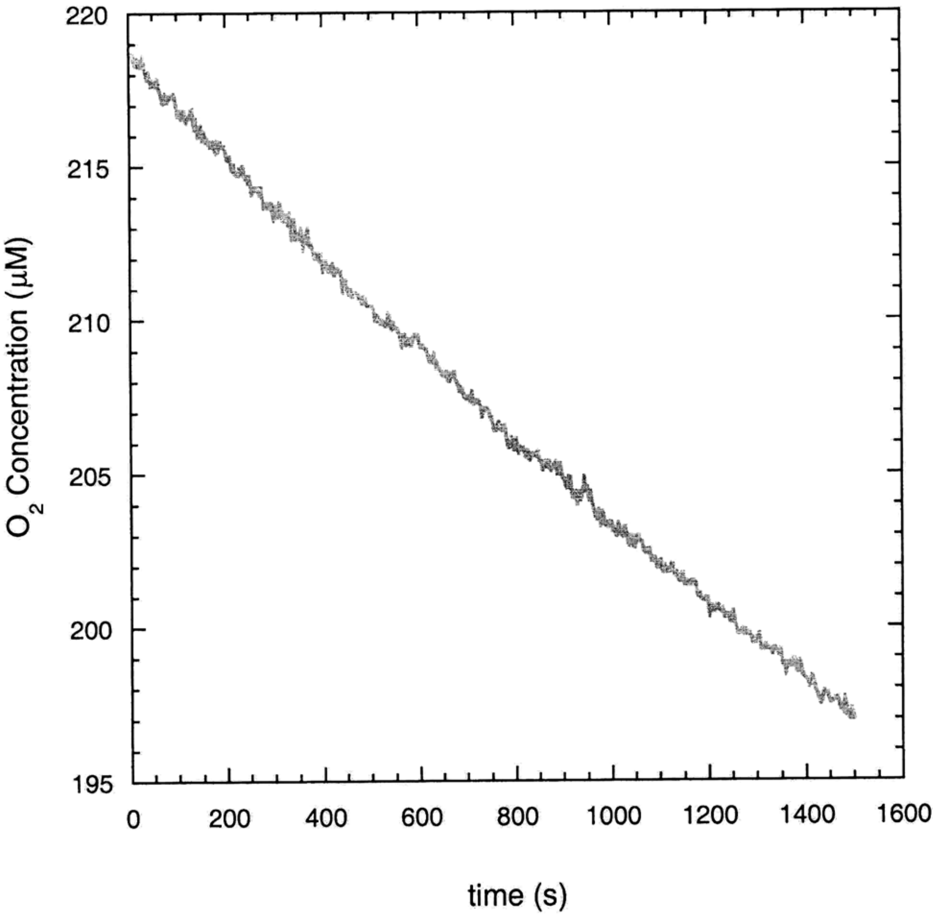

Figure 3.5. Respiration by HCT116 colonic epithelial cells. Shown is a plot of O_2 concentration as a function of time for a representative closed-chamber experiment with 8×10^6 unactivated HCT 116 cells.

measurements with RAW264.7 cells (Figure 3.7). As seen in Figure 3.6, the addition of rotenone (2 μM), a respiratory inhibitor, to activated RAW264.7 cells significantly decreased the rate of O_2 consumption . Applying the kinetic model to the data from such experiments, we calculated that $k_g = 2.3 \pm 0.6$ pmol s^{-1} $(10^6 \text{ cells})^{-1}$, $k_c = 1.3 \pm 0.3$ s^{-1}, and $R_{max} = 58.8 \pm 17$ (n = 6) for activated BMDMs (Table 3.2), all of which were not statistically different from the same kinetic parameters measured for RAW264.7 cells.

A representative plot of NO and O_2 concentrations for HCT116 cells measured 24 h after incubation with capsaicin and resveratrol is shown in Figure 3.8. Similar to the experiments with macrophages, a steady NO concentration was reached ~800 s after the experiment started, the value in this case being 0.16 μM. Again, inhibition of respiration by NO was observed in the plot of C_{O_2} versus time. Applying the kinetic model, $k_g = 1.1 \pm 0.$ pmol s^{-1} $(10^6 \text{ cells})^{-1}$, $k_c = 4.1 \pm 2.3$ s^{-1}, and $R_{max} = 40.8 \pm 11.4$ (n = 6) for activated HCT116 cells. For the HCT116 cells k_g was lower and k_c was higher than for macrophages ($p < 0.05$).

3.3.3. Nitrite and Nitrate Accumulation for Activated Cells

Figure 3.9 shows NO_2^- and NO_3^- concentrations measured for HCT116 cells pretreated with TNF-α (50 ng/mL) and IFN-γ (100 U/mL) and infected with live *H. cinaedi* bacteria. In this plot, 24 and 48 h correspond to the length of time that the cells were exposed to *H. cinaedi.* The NO_3^- concentrations in all samples remained nearly constant and were statistically indistinguishable from those detected in media alone. Likewise, uninfected cells and HCT116 infected with *H. cinaedi* at MOI = 10 yielded NO_2^- concentrations which were not different from those in the absence of cells. In contrast, a 4-fold increase in NO_2^- concentrations was measured after 24 h for HCT116 cells infected with *H. cinaedi* at MOI = 100, 18.5 ± 1.0 μM as compared

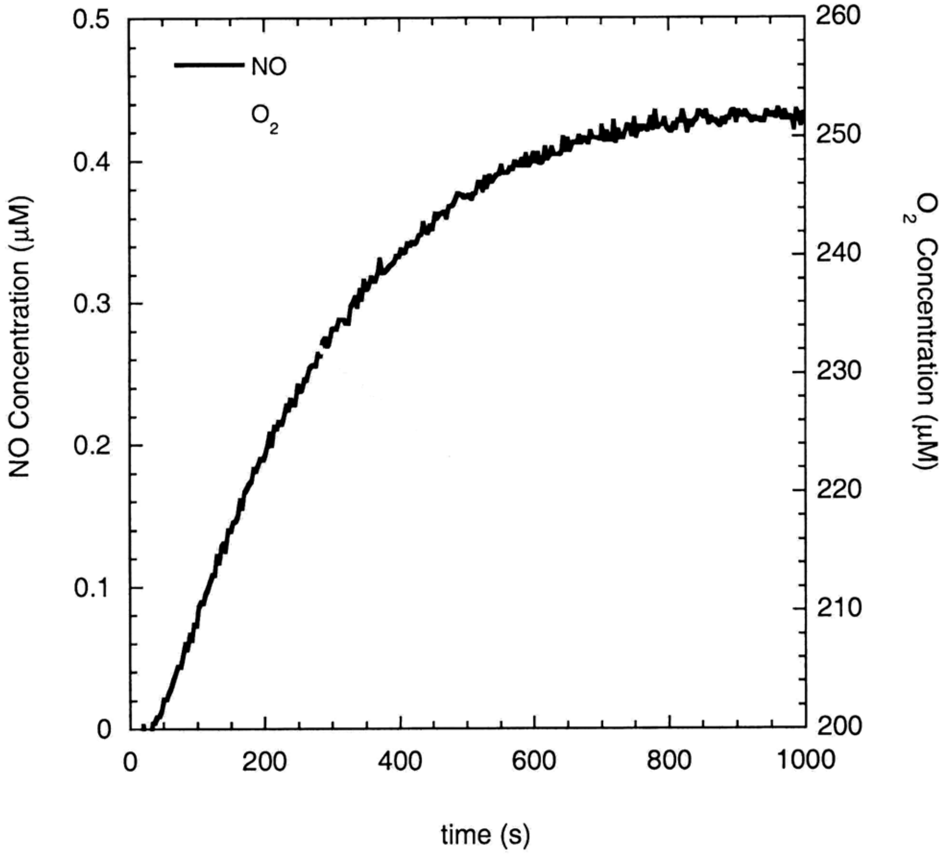

Figure 3.6. Measurement of NO synthesis, NO consumption, and O_2 consumption by activated primary macrophages (BMDM). After activation by 12 h exposure to IFN-γ and LPS, 8×10^6 cells were placed in the closed chamber at $t = 0$. As seen in this representative plot of NO and O_2 concentrations, the rate of O_2 consumption slowed as the NO concentration increased. The kinetics of NO synthesis and consumption are reflected in the plateau concentration for NO and the rate at which the plateau is reached.

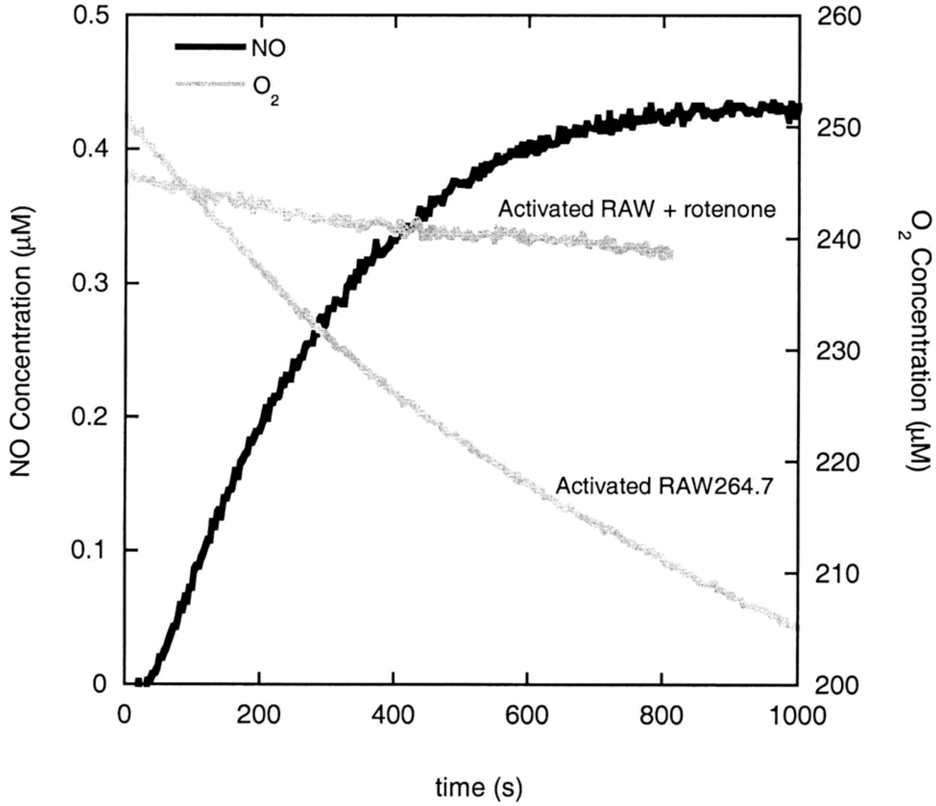

Figure 3.7. Representative plot of NO and O_2 concentrations for activated RAW264.7 cells in closed chamber experiments (8×10^6 cells), as described for BMDMs. O_2 concentrations were also monitored for activated RAW264.7 cells (9×10^6 cells) after a 1 h exposure to 2 μM rotenone, a respiratory inhibitory.

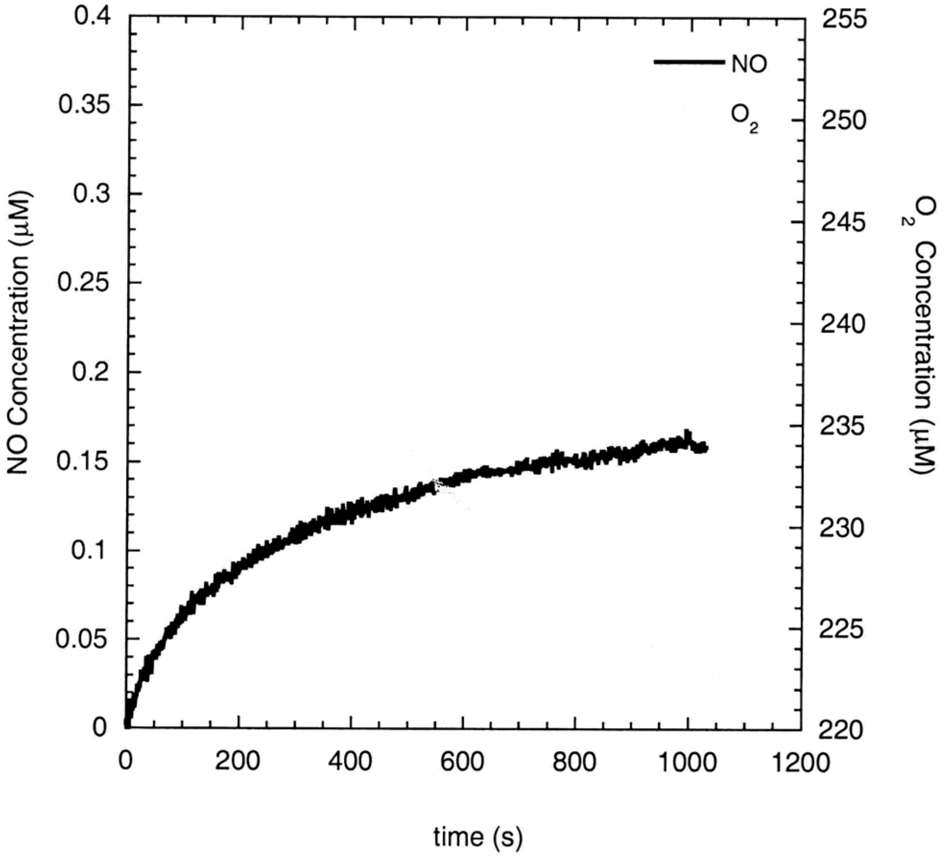

Figure 3.8. Measurement of NO synthesis, NO consumption, and O_2 consumption by activated HCT116 cells stimulated with capsaicin and resveratrol. Results are shown for 7 × 10^6 cells in the closed chamber. Induction of NO synthesis, as reflected by the increasing NO concentration, inhibited respiration in a manner similar to that seen with macrophages in Figures 3.4 and 3.5.

Table 3.2. Cellular kinetic parameters for NO, O_2, and O_2^- measured in the closed-chamber experiments.

Kinetic Parameter	RAW264.7	BMDM	HCT116
R_{max}^{o} (pmol s^{-1} 10^6 $cells^{-1}$)	37.7 ± 4.3 (n = 4)	30.2 ± 3.4 (n = 4)	26.0 ± 6.8 (n = 4)†
R_{max} (pmol s^{-1} 10^6 $cells^{-1}$)	61.9 ± 14 (n = 6)	58.8 ± 16.7 (n = 6)	40.8 ± 11.4 (n = 6)‡
k_g (pmol s^{-1} 10^6 $cells^{-1}$)	2.1 ± 0.3 (n = 6)	2.3 ± 0.6 (n = 6)	1.1 ± 0.2 (n = 6)†‡
k_c (s^{-1})	1.6 ± 0.4 (n = 6)	1.3 ± 0.3 (n = 6)	4.1 ± 2.3 (n = 6)†‡
k_s^o (pmol s^{-1} 10^6 $cells^{-1}$)	0.07 ± 0.02 (n = 4)	0.05 ± 0.01(n = 4)	-
k_s (pmol s^{-1} 10^6 $cells^{-1}$)	0.3 ± 0.09 (n = 4)	0.3 ± 0.08 (n = 4)	-

Symbols: R_{max}^{o} and R_{max}, maximum respiration rates for unactivated and activated cells, respectively; k_g, rate of generation of NO; k_c, rate constant for intracellular consumption of NO for activated cells; k_s^o and k_s, rates of extracellular O_2^- generation by unactivated and activated macrophages, respectively. All values are mean ± SD for the number of experiments indicated. † $p < 0.05$ versus RAW264.7 values, ‡ $p < 0.05$ versus BMDM values.

to 4.7 ± 0.6 μM for uninfected cells. The rate of NO_2^- accumulation for MOI = 100 was lower for 24-48 h than for 0-24 h, probably due to a reduced number of viable cells. Experiments in which HCT116 cells were exposed in the same manner to killed bacteria did not result in NO_2^- accumulation. Moreover, Griess assays on suspensions containing only *H. cinaedi* at concentrations corresponding to MOI = 10 or 100 were negative, indicating that the bacteria were not the source of NO_2^- accumulation in the media.

Figure 3.10 shows NO_2^- accumulation for RAW264.7 cells infected with *H. cinaedi* for 24 h at MOI = 10 or 100. The 24 h data for infected HCT116 cells are shown again for comparison. The NO_2^- concentrations measured for RAW264.7 cells infected at MOI = 100 (20.1 ± 2.7 μM and 27.7 ± 1.9 μM for samples collected at 24 and 48 h, respectively) were not statistically different from those measured for HCT116 cells. However, unlike HCT116 cells, which were unresponsive to *H.Cinaedi* infections at MOI = 10, samples collected from infected RAW264.7 cells showed increased NO_2^- accumulation after 48 h (17.0 ± 3.0 μM) when compared to uninfected cells (5.1 ± 0.7 μM).

The NO_2^- concentrations measured 24 h after infection with *H. cinaedi* at MOI = 100 were used to infer rates of NO production for macrophages and epithelial cells, using the open-system model. NO synthesis rates for HCT116 cells and RAW264.7 cells were found to be 3.9 ± 0.1 and 2.6 ± 0.1 pmol s^{-1} 10^6 $cells^{-1}$, respectively (Table 3.3). Thus, under these conditions, the rate of NO synthesis of HCT116 cells was 50% higher than that of RAW264.7 cells.

Similarly, rates of NO synthesis were calculated from NO_2^- accumulation data for BMDM and RAW264.7 cells stimulated with IFN-γ and LPS. After 8 h, NO_2^- and NO_3^- concentrations increased continuously and were approximately linear in time for t = 8 – 48 h (see

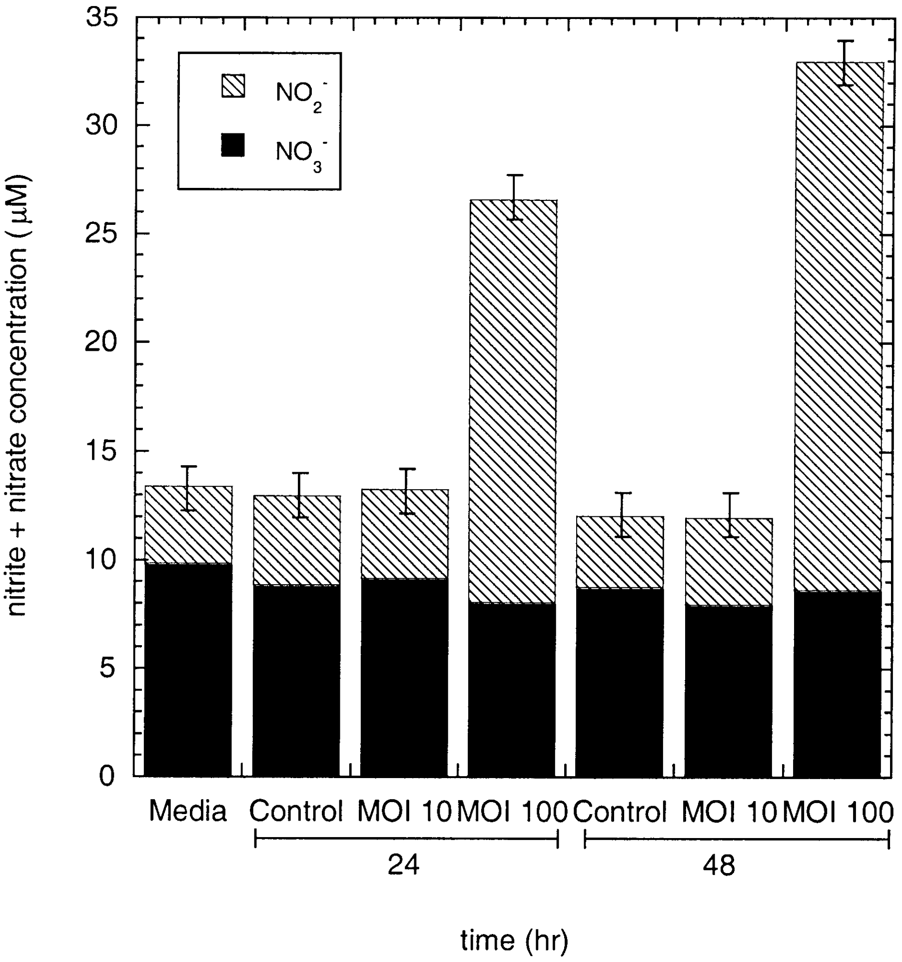

Figure 3.9. Nitrite and nitrate concentrations in the supernatant of HCT116 cells which were infected with *H. cinaedi*. Means ± SD are shown for $n = 5$. The initial cell numbers were 1×10^6 for HCT116 and 1×10^7 or 1×10^8 for *H. cinaedi*, yielding multiplicity of infections (MOI) of 10 or 100. The times (24 or 48 h) correspond to the duration of exposure to the bacteria. The increased NO_2^- concentrations for MOI = 100 are evidence of NO synthesis by the HCT116 cells.

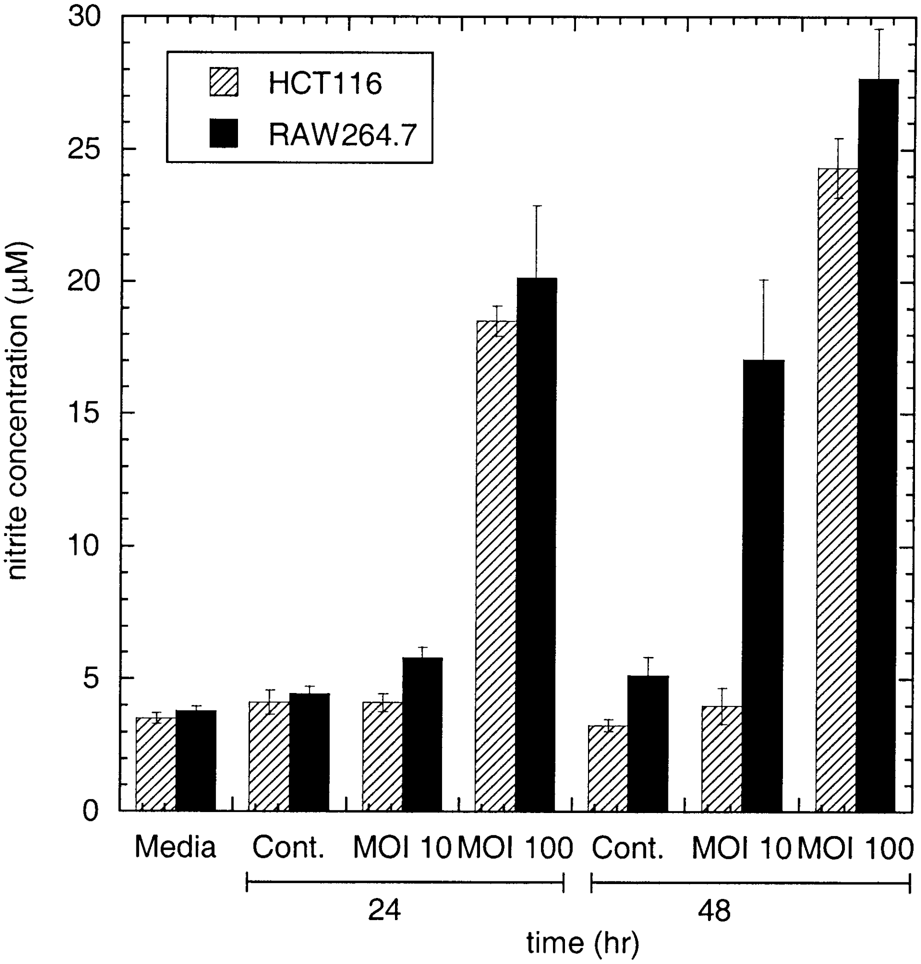

Figure 3.10. Comparison of NO_2^- concentrations for RAW264.7 cells and HCT116 cells infected with *H. cinaedi*. Means ± SD are shown for *n* = 5. See Figure 3.7 for additional explanation.

Table 3.3. Conditions and measured rates of NO synthesis for the open-system experiments.

Parameter	RAW264.7	BMDM	HCT116	RAW264.7
Stimulant	IFNγ + LPS	IFNγ + LPS	TNF-*α* + IFN-γ, *H.Cinaedi*	*H.Cinaedi*
α	0.35	0.2	0.2	0.2
β	0.15	0.15	0	0.15
L	5 mm	5 mm	2 mm	2 mm
Fraction NO lost	0.32	0.43	0.82	0.71
k_g . pmol s^{-1} (10^6 cells)$^{-1}$)	2.5 ± 0.6 (n = 2)	2.3 ± 0.9 (n = 2)	3.9 ± 0.1 (n = 5)	2.6 ± 0.1 (n = 5)

Symbols: α, fraction of plate area covered by cells; β, ratio of O_2^- to NO flux at cells; L, liquid depth; k_g, rate of NO generation by cells. Values for k_g are mean ± SD.

Appendix C.10-11). The average slopes obtained by linear regression over that interval were used to determine the accumulation rates of NO_2^-. The calculated rates of NO synthesis (k_g) for RAW264.7 cells in the open system were indistinguishable from those for BMDM (Table 3.3), and the rates for either type of macrophage in the open system agreed with those in the closed chamber (compare with Table 3.2).

3.3.4. Superoxide Synthesis

Figure 3.11 shows a representative plot of ferrocytochrome c concentration as a function of time in experiments designed to measure rates of O_2^- synthesis for BMDM. Data are shown for unactivated and activated BMDM as well as for culture medium alone (with and without SOD present), with $t = 0$ being the time at which fresh medium with or without NMA, SOD, LPS, and IFN-γ was added. The linear increase in the concentration of ferrocytochrome c with time indicates that O_2^- synthesis occurred at a constant rate throughout the 8 h period. Samples containing SOD (either with unactivated cells, activated cells, or media alone) were indistinguishable from one another and had significantly lower slopes of ferrocytochrome c vs. time compared to samples without SOD. The difference in the slopes between experiments conducted in the absence or presence of SOD was used to calculate the O_2^- production rates for activated and unactivated macrophages (k_s and k_s^o) listed in Table 3.2. Similar results were obtained for RAW264.7 cells (Figure 3.12). Unactivated macrophages yielded slopes that were indistinguishable from those for medium alone, implying that little or no O_2^- is produced at their outer membrane surface, which is consistent with previous work showing low NADPH oxidase activity in untreated macrophages [Sasada, et al., 1983]. As shown in Table 3.2, the net cellular superoxide synthesis rate is only 13% of the rate of NO synthesis by activated BMDM.

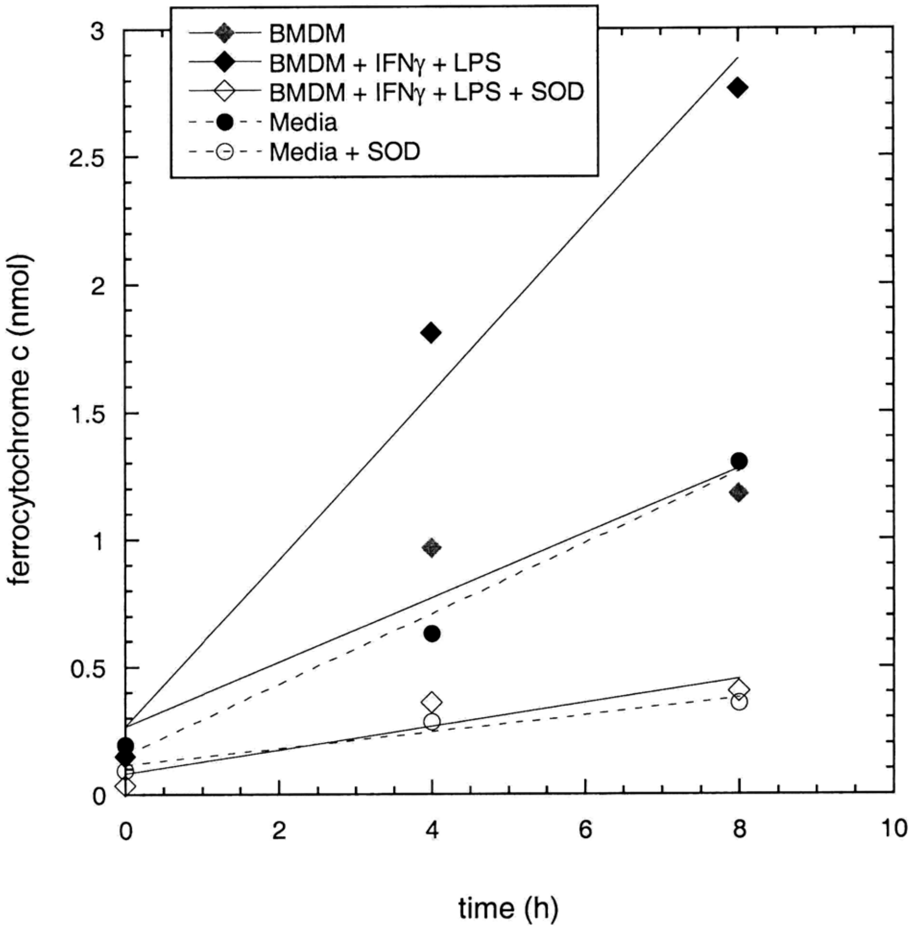

Figure 3.11. Rate of O_2^- production by primary macrophages (BMDM). Plotted are nmol of ferrocytochrome *c* detected as a function of time for representative experiments with 5×10^5 cells and with culture medium only. Results are shown for cells activated by incubation with IFN-*γ* and LPS beginning at *t*= 0 in the absence or presence of SOD, unactivated cells, untreated medium, and medium with SOD. The rate of cellular O_2^- production was calculated from the difference in slopes between the data for activated or unactivated cells and that for medium with SOD. The results for unactivated cells and untreated medium were nearly identical. The addition of SOD eliminated most of the ferrocytochrome c formation associated with the media.

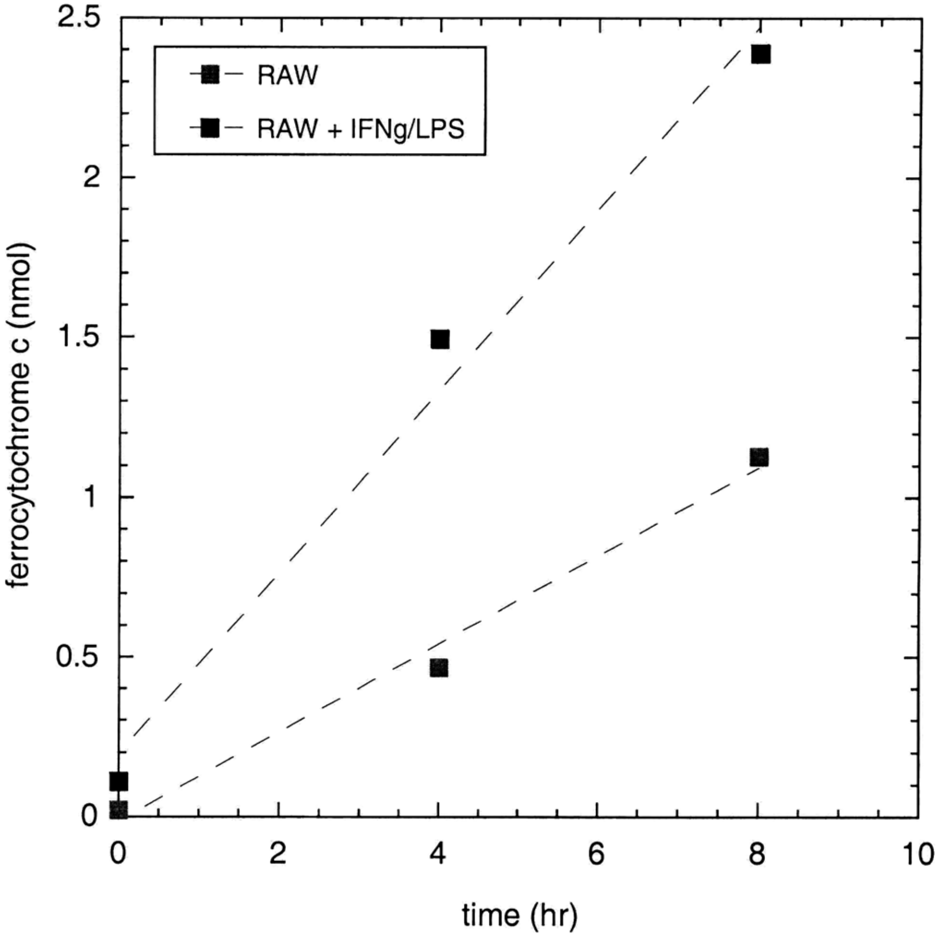

Figure 3.12. Rate of O_2^- production by RAW264.7 cells. Plotted are nmol of ferrocytochrome *c* detected as a function of time for representative experiments with 5×10^5 cells. The rate of cellular O_2^- production was calculated from the difference in slopes between the data for activated (with IFNγ + LPS) or unactivated cells and that for medium with SOD (from Figure 3.9).

Similar experiments to determine whether or not HCT116 cells are capable of producing extracellular O_2^- were also conducted. Supernatant samples collected from HCT116 cells, incubated with and without capsaicin and resveratrol, yielded ferrocytochrome c concentrations that were not statistically different from medium alone, confirming that activated and unactivated epithelial cells produce little or no extracellular O_2^-.

3.4. Discussion

The present study provides the first relatively direct measurements of the rates of NO, O_2, and O_2^- production and consumption by primary macrophages (BMDM) and a colonic epithelial cell line (HCT116) under simulated inflammatory conditions. Included also are new data for a macrophage-like cell line (RAW264.7) that had been studied previously using the same methodology. The results for activated RAW264.7 cells in the closed chamber (Table 3.2) are comparable to the previously reported values of $k_g = 4.9 \pm 0.6$ pmol s^{-1} $(10^6 \text{ cells})^{-1}$, $k_c = 0.6 \pm 0.8$ s^{-1}, $k_s = 0.32 \pm 0.07$ pmol s^{-1} $(10^6 \text{ cells})^{-1}$, $R_{max} = 108 \pm 17$ pmol s^{-1} $(10^6 \text{ cells})^{-1}$ [Nalwaya and Deen, 2005], although there are some differences. The present rates of NO generation (k_g) and respiration (R_{max}) are each about one-half the previous values, and the rate constant for NO consumption (k_c) is about twice that reported before, whereas the cellular rate of O_2^- generation (k_s) is nearly identical to the previous value. The maximum NO concentrations generated by RAW264.7 cells in the closed chamber (0.2 – 0.4 μM) were also very similar to those found before [Nalwaya and Deen, 2005]. With one-half the rate of NO synthesis and the same rate of O_2^- generation, the present O_2^-/NO synthesis ratio is twice the previous value (0.14 vs. 0.07). The numerical differences aside, the present results confirm that NO is synthesized by RAW264.7 cells in large excess relative to O_2^-.

Respiration in unactivated RAW264.7 cells was similar to that in BMDM and HCT116 cells. The O_2 consumption rates for each equaled R_{max}^{o}, the measured values of that parameter (Table 3.2) being within the range reported for other mammalian cells [Yamada, et al., 1985; Balis, et al., 1999]. Also consistent with findings for other cells is that the rate of O_2 consumption in the absence of NO was constant [Yamada, et al., 1985; Balis, et al., 1999], as exemplified by the linear plot in Figures 3.3-3.5. Activation of macrophages (both RAW264.7 and BMDM) did not change their overall rates of O_2 consumption, an approximate doubling of the maximum rate of respiration (R_{max}, Table 3.2) compensating almost exactly for the inhibitory effects of NO. Despite the added demand for O_2 associated with NO synthesis and NO consumption, O_2 consumption by activated macrophages remained mostly respiratory. Assuming C_{O_2} = 200 μM and C_{NO} = 0.5 μM, which are representative of concentrations measured in the closed chamber experiments, the NO synthesis and consumption terms in Equation 3.4 account for only about 10% of total O_2 consumption. The remarkable constancy of total O_2 consumption suggests that iNOS expression may be linked to the respiratory needs of the cell. That is, the rate of NO synthesis, and therefore the NO concentration, may be capped at a level which does not depress the respiration rate below that of an unactivated cell.

Although it is possible that lower, physiological O_2 concentrations could affect iNOS gene expression and thus the rates of NO synthesis reported here, the available findings concerning O_2 are contradictory. Otto and Baumgardner (2001) determined that iNOS activity paralleled the O_2 levels over a wide range, whereas Palmer *et al.* (1998) found an increase in iNOS protein when P_{O_2} was lowered. McCormick *et al.* (2000) reported that the amount of iNOS protein was unaffected by P_{O_2}. Thus, more data are needed to examine the possible effects of O_2 and NO on total iNOS activity.

The rate constant for NO consumption by either type of macrophage ($k_c = 1.3 - 1.6\ s^{-1}$, Table 3.2) is in the range of reported values for other cell types, including NH32 ($0.1\ s^{-1}$) and βTC3 cells ($1.7\ s^{-1}$) [Wang, 2003]. Our results support the possibility that NO can also be consumed by iNOS due to NO rebinding to form NO_3^- via the 'futile pathway' of iNOS. As discussed by Nalwaya and Deen (2005), k_c can be interpreted as the sum of the NO consumption rate for unactivated macrophages ($k_c°$) and an additional term for iNOS NO consumption (k_g/K), where K is the hypothetical upper bound for C_{NO} that would be achieved at steady state by iNOS acting alone. Using previously measured rates for NO consumption by unactivated RAW264.7 cells ($0.9\ s^{-1}$), the value of k_g from Table 3.2 for BMDM, and the value of K (3.4 μM) determined from the modeling results of Santolini *et al.* (2001), the calculated rate for NO consumption rate by activated macrophages with consideration of NO consumption by iNOS is $1.7\ s^{-1}$, which is in good agreement with our measured values of k_c,(Table 3.2).

Nevertheless, consumption of NO by macrophages is only marginally significant relative to NO synthesis. For instance, at $C_{NO} = 0.5$ μM, the cellular rate of NO consumption by BMDM would be 0.5 pmol s^{-1} (10^6 cells)$^{-1}$, which is about 20% of the rate for NO synthesis (k_g, Table 3.2). At higher NO concentrations, or with higher values for k_c, as is the case with colonic epithelial cells, NO consumption becomes a larger fraction of NO synthesis and therefore has more impact on net synthesis. The rate constant for NO consumption by HCT116 cells (k_c, Table 3.2) is approximately double that of macrophages, but still in the range of reported rates for other cell types including NH32 human lymphoblast ($0.1\ s^{-1}$) , βTC3 pancreatic beta cells ($1.7\ s^{-1}$) [Wang, 2003] , and MLE murine lung epithelial cells ($9\ s^{-1}$) [Gardner *et al.*, 2001]; NO consumption rates for another colonic epithelial cell line (Caco-2) are even higher ($37.7\ s^{-1}$) [Gardner, et al., 2001], suggesting a great degree of variability amongst cell-lines. As suggested by the values of k_g for HCT116 in Tables 3.2 and 3.3, the rate of NO synthesis by epithelial cells can be similar to that of macrophages. Thus, depending on the value of k_c, colonic epithelial cells may consume half or more of the NO that they synthesize.

Plots of NO and O_2 concentrations (Figure 3.6) and superoxide synthesis (Figure 3.11) for BMDM activated with IFN-γ and LPS were nearly identical to those of activated RAW264.7 cells (Figures 3.7 and 3.12). Accordingly, the NO, O_2, and O_2^- synthesis and consumption rates for primary bone marrow-derived macrophages and RAW264.7 cells (Table 3.2) were statistically indistinguishable. This similarity in cellular kinetics complements early work showing comparable rates of NO_2^- and NO_3^- formation in primary peritoneal macrophages and macrophage cell lines [Stuehr and Marletta, 1987]. The nearly identical kinetic behavior of RAW264.7 cells and primary macrophages confirms the suitability of the former for *in vitro* NO toxicity studies. In other words, co-culture of target cells with RAW264.7 should yield realistic concentrations of reactive nitrogen species. It should be noted, however, that RAW264.7 cells may differ from primary macrophages derived using other methods; for instance, LPS-treated RAW264.7 cells produce much greater quantities of TNF-α than resident peritoneal macrophages [Rouzer, et al., 2005].

Monitoring closed-chamber NO and O_2 concentrations for HCT116 cells treated with capsaicin and resveratrol (as in Figure 3.8) demonstrated that colonic epithelial cells are capable of synthesizing NO at rates comparable to macrophages, quantified the ability of this cell line to consume NO, and confirmed the expected inhibitory effect of NO on respiration. To create conditions that would more closely mimic intestinal inflammation, additional experiments were performed in which HCT116 cells were infected with *H. cinaedi*. Due to potential contamination of the NO electrode by the bacteria, rates of NO synthesis by infected cells were calculated from

NO_2^- concentrations measured by Griess assays in an open system. At a bacterium-to-mammalian cell ratio (MOI) of 100, NO_2^- concentrations measured in the supernatant of HCT116 cells pretreated with TNF-α and IFN-γ and infected were four-fold higher than with uninfected HCT116 cells (Figure 3.9). Samples infected at MOI = 10 did not show increased NO_2^- accumulation, indicating that a minimum cell number ratio is needed to stimulate NO production by epithelial cells. The use of killed *H. cinaedi* in the infection protocol did not induce NO production in HCT116 cells, suggesting that viable, motile bacteria are necessary.

Without IFN-γ and TNF-α pretreatment, live *H. cinaedi* infection did not elicit NO synthesis from HCT116 cells, indicating that one or more signaling components must be recruited in advance of bacterial exposure. The toll-like receptors (TLRs) serve as receptors for various microbial products; in particular, TLR4 functions as the main receptor for LPS from gram-negative bacteria and thus is required for effective LPS signal transduction. HCT116 cells have been shown to be non-responsive to LPS stimulation in terms of IL-8 production largely because of their limited TLR4 expression [Suzuki, et al., 2001]. Consequently, HCT116 cells may respond to LPS from *H. cinaedi* through a mechanism independent of surface expression of TLR4. In a murine small-intestinal epithelial cell line, Hornef et al. found TLR4 in the Golgi apparatus which colocalized with internalized LPS [Hornef, et al., 2002]. Thus the combination of TNF-α/IFN-γ pretreatment and live, motile bacteria may augment the incorporation of LPS into cytoplasm in HCT116 cells, which can provide signals for NO production through intracellular TLR4 complexes. Additional studies are needed to clarify the mechanisms by which bacteria induce NO production in colonic epithelial cells during infection.

Infection with *H. cinaedi* also elicited NO production by macrophages. The rates of NO synthesis for infected RAW264.7 cells were remarkably similar to those obtained by using just

IFN-γ and LPS to activate the macrophages in the open system (k_g, Table 3.3). Also, the rates for RAW264.7 cells activated with IFN-γ and LPS were found to be the same in the open system as in the closed chamber (k_g, Tables 3.2 and 3.3). Although NO_2^- accumulation after 24 h was nearly identical for infected RAW264.7 cells and infected HCT116 cells (Figure 3.10), the rate of NO synthesis by the latter was calculated to be about 50 % greater than by the former. This is a reflection of the higher rate constant for NO consumption in HCT116 cells, measured in separate experiments (k_c, Table 3.2). Previous estimates of epithelial NO synthesis rates span some two orders of magnitude, ranging from 0.9 fmol s^{-1} (10^6 cells)$^{-1}$ to 0.2 pmol s^{-1} (10^6 cells)$^{-1}$ [Wright, et al., 1999; Witthoft, et al., 1998]. Our rate of 3.9 pmol s^{-1} (10^6 cells)$^{-1}$ for infected HCT116 cells is much higher than any of the reported values. Contributing to this is that our open-system calculations accounted for NO loss to the headspace, which is commonly neglected. As shown in Table 3.3, the fraction of NO lost was calculated to range from 30% to 80% of that synthesized, depending on the liquid depth and cell type. The cell type is influential because cellular consumption of NO combines with extracellular autoxidation to compete with NO diffusion to the headspace. If the reaction-diffusion model had not been used to correct for NO losses, the rates of NO production in the open-system experiments would have been underestimated by as much as five-fold. The excellent agreement found between the closed-chamber and open-system values of k_g for RAW264.7 cells provides confidence in the corrections made for NO loss.

A computational model designed to predict NO concentrations in a colonic crypt during inflammation was developed previously [Chin, et al., 2008]. By using differential equations to describe rates of diffusion and reaction of NO and O_2 in an idealized representation of the crypt anatomy, concentrations are obtained as a function of position. In addition to the crypt shape and

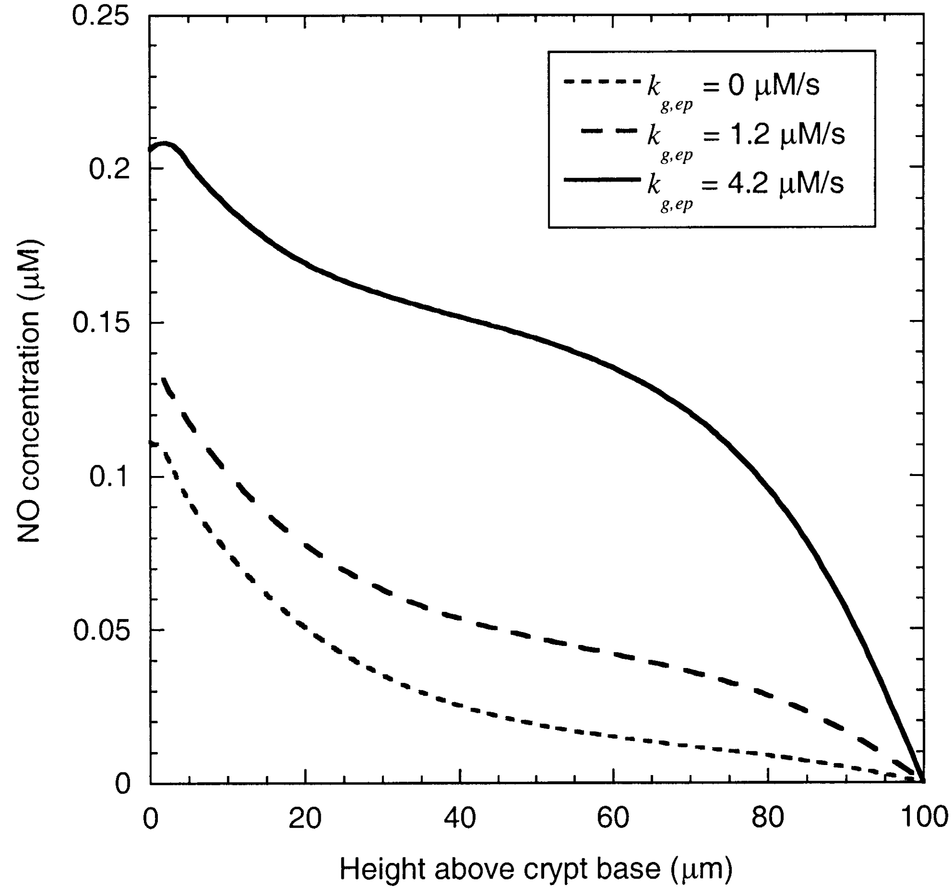

Figure 3.13. Predicted NO concentrations in an inflamed colonic crypt. Concentrations at the crypt center are plotted as a function of height above the base. The calculations assumed that k_c = 1.3 s^{-1} for macrophages and 4.1 s^{-1} for epithelial cells, based on the BMDM and HCT116 data in Table 3.2. The rate of NO synthesis used for macrophages was 2.3 pmol s^{-1} $(10^6 \text{ cells})^{-1}$ (Table 3.2); using the cell volume (*v*) in Table 3.1, this corresponds to a volumetric rate of 2.4 μM/s. Results are shown for three assumed rates of NO synthesis by epithelial cells: 0, 1.2, 4.2 μM/s. The latter values correspond to the HCT116 data for capsaicin-resveratrol in Table 3.2 and *H. cinaedi* in Table 3.3, respectively, again using *v* from Table 3.1. All other parameter values were as given in Chapter 2.

dimensions, key inputs in that model are the rates of NO synthesis and consumption by macrophages and epithelial cells. The rate constants for NO synthesis and consumption by BMDM and HCT116 cells in Tables 3.2 and 3.3 yield the results shown in Figure 3.13, in which the NO concentration is plotted as a function of height above the base of a crypt. Three cases are considered: (i) NO synthesis by macrophages only; (ii) NO synthesis by both macrophages and epithelial cells, using for the latter the capsaicin-resveratrol k_g for HCT116 cells; and (iii) NO synthesis by both cell types, using for epithelial cells the k_g for infected HCT116 cells. The localization of macrophages near the base of the crypt causes the NO concentration to be largest there, whether or not there is epithelial synthesis of NO. The greater the total rate of NO synthesis (macrophage plus epithelial), the larger the maximum NO concentration, which ranges from 0.11 μM to 0.21 μM for the three cases. Because epithelial cells line the entire crypt, their synthesis of NO tends to cause elevated NO concentrations to persist even in the upper part.

Even using the highest measured rates of epithelial NO synthesis (corresponding to infected HCT116 cells), the concentrations in Figure 3.13 are below the cytotoxic thresholds found when NO concentrations have been precisely controlled. The minimum NO concentration at which loss of viability was detected in human lymphoblastoid (TK6) cells was 0.5 μM [Wang, eta l., 2003; Li, et al., 2006], and other cell types, including HCT116, have been shown to be more resistant to NO [Li, et al., 2009]. Thus, even if epithelial cells *in vivo* are as sensitive to NO as TK6 cells, our model predicts that they will remain viable. At these sub-cytotoxic concentrations, exposure to NO and related reactive nitrogen species may initiate a mutagenic change in the population of epithelial cells within the colonic crypt that causes irregular proliferative behavior and ultimately leads to cancer. Alternatively, at the sub-micromolar NO concentrations, NO may act synergistically with low oxygen to induce cell death; due to reversible binding to cytochrome oxidase, even low (nM) concentrations of NO are sufficient to inhibit electron transport at physiological oxygen levels [Brown and Cooper, 1994]. In either case, the concentration estimates for colonic crypts that we have obtained from cellular kinetic measurements and modeling provide guidance in selecting experimental conditions that should be useful in elucidating the molecular biological linkage between NO exposure and carcinogenesis in IBD.

Chapter 4. Predicting Nitric Oxide Concentrations in Melanoma

4.1. Introduction

Nitric oxide may play a role in the growth and metastasis of melanoma, the most malignant of skin cancers [Grimm, 2008; Balch, *et al.*, 2001]. The presence of inducible nitric oxide synthase (iNOS) and nitrotyrosine provides evidence of NO production within some human melanomas, and these two markers for NO are correlated with poor survival rates of patients [Ekmekcioglu *et al.*, 2000]. Studies with melanoma cells suggest that NO derived from iNOS may stimulate proliferation as well as promote resistance to apoptosis [Tang and Grimm, 2004]. However, efforts to establish mechanistic links have been hampered by the absence of information on NO concentrations. Our objective was to provide concentration estimates by combining cell kinetic data with a mathematical model designed to describe reactions and diffusion of NO in cutaneous melanomas.

Metastatic melanomas are typically in the vertical-growth phase and can penetrate more than 4 mm into the dermis, sometimes reaching the subcutaneous tissue before spreading to regional lymph nodes [Morton *et al.*, 2006]. A network of blood vessels and capillaries extends upwards from the subcutaneous tissue into the dermis, as shown schematically in Figure 4.1a. The tumor stroma, or interposing region between malignant melanoma cells and normal dermal tissue, consists of fibrillated extracellular matrix components to form the interstitial connective tissue that accommodates the expansion of the tumor mass as it invades surrounding tissue. In cutaneous melanomas, the stroma often includes inflammatory cells such as macrophages and the infiltration of macrophages has also been linked to tumor growth [Torisu *et al.*, 2000]. Thus, synthesis and consumption of NO by macrophages as well as melanoma cells must be taken into account when estimating NO concentrations. Nitric oxide synthesized within a cell can readily

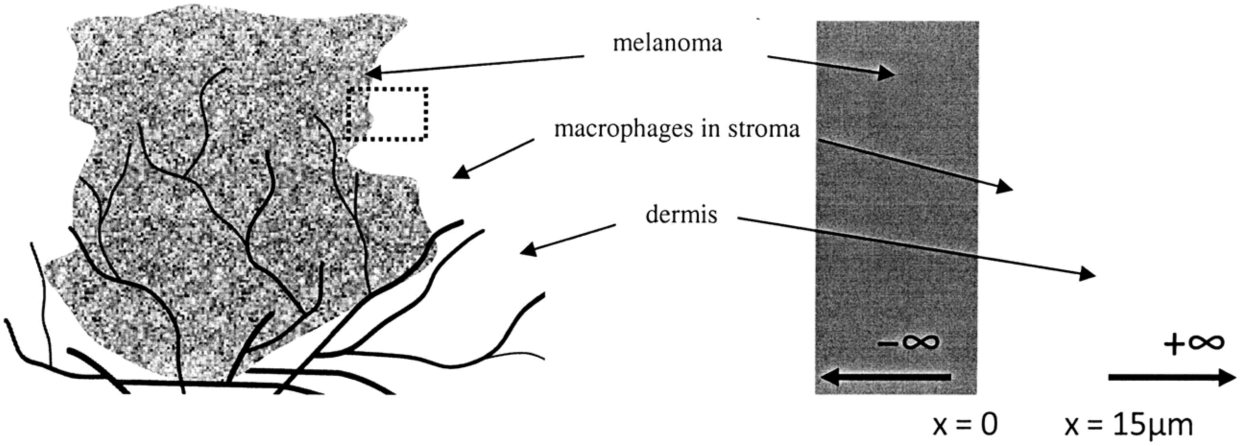

(a) (b)

Figure 4. 1. (a) Schematic representation of a cutaneous melanoma. **(b)** An enlargement of the area enclosed in the dashed box in Figure 4.1a that represents the edge of a melanoma tumor.

cross cell membranes and diffuse to neighboring cells. Its permeation through lipid bilayers and diffusion through water are both very similar to that of O_2 [Subczynski *et al.,* 1996; Zacharia and Deen]. Nitric oxide is consumed by autoxidation, intracellular pathways which are both enzymatic and non-enzymatic, and oxidation by oxyhemoglobin. Each of these rate processes requires consideration when simulating NO levels in melanomas.

The uncatalyzed reaction of NO with O_2 (autoxidation) yields NO_2^- as the end-product, with NO_2 and N_2O_3 formed as intermediates [Lewis *et al.,* 1995]. The overall stoichiometry of this multi-step oxidation is

$$4NO + O_2 \rightarrow 2N_2O_3 \xrightarrow{+2H_2O} 4NO_2^- + 4H^+ . \qquad (4.1)$$

This reaction will occur both within cells and in extracellular spaces. However, although it is important in culture media and was taken into account in the experiments to be reported, it is too slow to have a significant effect on NO concentrations within a melanoma, as will be shown. One pathway for the intracellular consumption of NO involves its rapid reaction with O_2^- to form peroxynitrite ($ONOO^-$) and NO_3^- [Ischiropoulos *et al.,* 1992; Huie and Padmaja, 1993]:

$$NO + O_2^- \rightarrow ONOO^- \xrightarrow{CO_2} NO_3^- . \qquad (4.2)$$

Because O_2^- is a byproduct of respiration and this reaction is fast enough to compete with superoxide dismutase, it is expected to occur in virtually all cells. Other pathways for intracellular consumption of NO involve nitrogen dioxygenases [Gardner *et al.,* 2000], and reactions with oxygen-ligated reduced metals [Eich *et al.,* 1996]. Measurements of NO consumption by rat hepatocytes indicate that the overall intracellular NO consumption rate can be modeled as being first-order in NO concentration [Thomas *et al.*, 2001], which is consistent also with data from our laboratory for various cell types [Nalwaya and Deen, 2005; Chin and

Deen, 2010]. Lastly, any NO that reaches blood vessels is depleted by its rapid reaction with oxyhemoglobin (HbO_2) to form methemoglobin (metHb) and NO_3^- [Eich *et al.*, 1996]:

$$\mathrm{NO} + \mathrm{HBO_2} \rightarrow \mathrm{metHB} + \mathrm{NO_3^-} \qquad (4.3)$$

Accordingly, capillaries act as very effective sinks for NO in tissues.

It should be mentioned that Reaction 4.2 can also lead to a certain amount of NO consumption outside cells, because activated macrophages synthesize extracellular O_2^- via a membrane-bound NADPH oxidase [Babior, 1984; Berton *et al.,* 1988]. However, the diffusion-limited kinetics of Reaction 4.2, together with the fact that NO production exceeds extracellular O_2^- synthesis, makes this an extremely localized process. It has been estimated that the O_2^- produced by a macrophage is fully exhausted within 1 μm of the cell [Chen and Deen, 2002]. Moreover, the rate of sustained O_2^- release into the surrounding media by a macrophage has been found to be only about 10% of its rate of NO production [Chin *et al.*, submitted 2009]. For these reasons, extracellular consumption of NO by O_2^- can be neglected when modeling NO concentrations in tissues.

To provide the cell kinetic data needed for a reaction-diffusion model, NO synthesis and consumption were studied in a melanoma cell line, A375. Studies involving A375 cells suggest that endogenous NO is responsible for melanoma growth; A375 cells have been shown to constitutively express iNOS [Zheng, et al., 2004] and treatment of A375 cells with a NO scavenger (c-PTIO) has resulted in decreased cell growth [Grimm, et al., 2008]. Complementing the A375 data were previous measurements of NO synthesis and consumption in a macrophage cell line and in primary mouse macrophages, as described in Chapter 3. This cellular information was combined with other data on the rates of NO diffusion and reaction in aqueous media and with the anatomical length scales to simulate steady-state NO concentrations within a melanoma.

4.2. Materials and Methods

4.2.1. Cell Culture

A375 melanoma cells were obtained from American Type Culture Collection and were cultured in Dulbecco's modified Eagle's medium (DMEM) containing L-glutamine supplemented with 100 U/mL penicillin, 100 μg/mL streptomycin, and 10% (v/v) heat-inactivated fetal bovine serum (FBS) (BioWhittaker, Walkersville, MD). All cells were maintained at 37 °C in a humidified 5% CO_2 atmosphere.

4.2.2. NO Synthesis by A375 Cells

To assess the synthesis of NO by A375 cells under simulated inflammatory conditions, the supernatant of cells incubated in media with and without TNF-α (50 ng/mL) and IFN-γ (100 U/mL) was assayed for NO_2^- accumulation. The number of viable cells was determined by trypan blue exclusion and cells were seeded at concentrations of 1×10^6 cells/well into 6-well plates. Supernatant samples (1 sample per well) were collected at 24 and 48 hours after stimulation and centrifuged at 12,000 rpm before analysis. Nitrite accumulation was quantified using a Griess assay kit (R&D Systems, Minneapolis, MN). Briefly, 50 μL of culture supernatant was allowed to react with 100 μL of Griess reagent and incubated at room temperature for 10-30 min. Absorbance was measured at 540 nm using a microplate reader.

4.2.3. NO Consumption by Culture Medium and A375 Cells

For studies with culture medium alone, saturated NO solutions were prepared by equilibrating PBS with 10% NO gas. Oxygen was first purged from the PBS by bubbling the solution with Ar in a septum-sealed bottle. The NO gas, passed through a soda-lime column to remove any NO_x impurities, was then bubbled into the deoxygenated PBS. A 50 mL septum-sealed glass flask with a magnetic stir bar was used to determine the rate of NO consumption in DMEM with 25 mM HEPES (pH 7.4). After the vial was filled with the test liquid, NO was introduced by injecting 50 to 200 μL of the saturated PBS solution through the septum, to give a mixture concentration of 1-5 μM. The rate of NO consumption was calculated as described below from the decay of the NO concentration, which was monitored continuously with an electrode (World Precision Instruments, Sarasota, FL) inserted through the septum. The experiments were carried out in a warm room at 37 °C and in the dark to minimize light-sensitive O_2^- generation from the riboflavin in the media [Keynes *et al.,* 2003].

Rates of NO consumption by A375 cells were measured in a similar manner, but using a different closed chamber. A polycarbonate insert was machined to fit within standard 60 mm polystyrene tissue culture dishes and equipped with a stirring motor (Instech Laboratories, Plymouth Meeting, PA), NO electrode, and fiberoptic O_2 sensor (Instech Laboratories, Plymouth Meeting, PA), as depicted in Figure 3.2. After assembly the chamber had a total liquid volume of 8.8 mL. The number of viable cells was determined by trypan blue exclusion and between 3×10^6 and 5×10^6 cells were seeded onto 60 mm dishes. After the cells were allowed to adhere for 2-3 h, fresh, preheated media with 25 mM HEPES was added to the dish and the insert was attached. Between 50 and 100 μL of NO in PBS was introduced through an injection port in the apparatus, giving initial NO concentrations of 1-5 μM. The NO concentration was monitored until it approached zero, typically 10-15 min. To check an assumption made in the kinetic model (see below), O_2 concentrations were also measured in some of the cell experiments.

4.2.4. Kinetic Model for NO Consumption in Vitro

The closed chambers were modeled as well-stirred batch reactors, as described previously in Chapter 3. In general, the variation in NO concentration (C_{NO}) with time (t) is governed by

$$\frac{dC_{NO}}{dt} = \frac{m}{V}\left(k_g - vk_c C_{NO}\right) - 4k_a C_{NO}{}^2 C_{O_2} - k_m \tag{4.4}$$

where m is the number of viable cells, V is the liquid volume, v is the volume of a single cell, (modeled as a hemisphere with radius = 7.5 μm [Sheriden *et al.,* 1981]), k_g is the rate of generation of NO, k_c is the rate constant for intracellular consumption of NO, k_a is the rate constant for autoxidation of NO, and k_m is the rate of extracellular NO consumption by culture-medium-generated O_2^-. The values for V, v, and k_a are given in Table 4.1, and the number of cells was known for each experiment. The experiments were designed to evaluate k_g, k_c, and k_m.

In the absence of cells, Eq. 4.4 reduces to

$$\frac{dC_{NO}}{dt} = -4k_a C_{NO}{}^2 C_{O_2} - k_m \tag{4.5}$$

and the corresponding O_2 balance is

$$\frac{dC_{O_2}}{dt} = -k_a C_{NO}^2 C_{O_2} \tag{4.6}$$

Preliminary calculations in which Eqs. 4.5 and 4.6 were solved together numerically showed that O_2 consumption by autoxidation is negligible for the NO and O_2 concentration ranges in our experiments with media. Accordingly, Eq. 4.6 was discarded and C_{O_2} in Eq. 4.5 was approximated by the liquid-phase O_2 concentration in equilibrium with air ($C_{O_2}^o$). The value used (Table 4.1) was based on the solubility of O_2 in water at 37°C [Lange, 1967]. For this circumstance with constant C_{O_2}, the solution of Eq. 4.5 is

$$C_{NO}(t) = \frac{\sqrt{k_m k_a C_{O_2}^o}}{2k_a C_{O_2}^o} \tan\left(-2t\sqrt{k_m k_a C_{O_2}^o} + \arctan\left(C_{NO}^o \frac{2k_a C_{O_2}^\circ}{\sqrt{k_m k_a C_{O_2}^o}}\right)\right) \tag{4.7}$$

where C_{NO}^{o} is the initial NO concentration. With k_a being known (Table 4.1), k_m was found by minimizing the root-mean-square difference between the measured and calculated NO concentrations, using Microsoft Excel (Microsoft, Redmond, WA).

With cells present, there was a 5-8% decline in O_2 concentration during the four experiments in which it was measured. Two approaches were compared for evaluating the O_2 concentration when calculating k_c from the cellular NO data. In one, the measured, time-dependent values of C_{O_2} were used in the differential equation for NO. In the other, C_{O_2} was approximated as a constant, equal to 97% of $C_{O_2}^{\circ}$. Because the values of k_c obtained using the two methods differed by less than 1%, the second (simpler) method was adopted. With constant C_{O_2}, the solution of Eq. 4.4 is

$$C_{NO}(t) = \frac{B}{8k_a C_{O_2}^{o} V}\left[\tanh\left(\frac{tB}{2V} + \operatorname{arctanh}\left(\frac{8Vk_a C_{O_2}^{o} C_{NO}^{o} + mvk_c}{B}\right)\right)\right] - \frac{mvk_c}{8k_a C_{O_2}^{o} V} \qquad (4.8)$$

$$B = \sqrt{16mVk_g k_a C_{O_2}^{o} - 16V^2 k_m k_a C_{O_2}^{o} + m^2 v^2 k_c^2} \qquad (4.8b).$$

Given m (as determined for each experiment), the values for v, V, and k_a listed in Table 4.1, and with k_g and k_m evaluated from separate experiments, k_c was calculated by minimizing the root-mean-square difference between the measured and calculated NO concentrations using the simplex method in MATLAB (MathWorks, Natick, MA).

4.2.5. Melanoma Model

The modeling of chronically elevated NO concentrations in body tissues differs from that in the in vitro experiments in three ways. First, the concentrations are nearly time-independent. A steady-state assumption is justified for melanoma by the fact that the time required for NO to

Table 4.1. Parameters used in the kinetic model for the closed chamber apparatus to fit k_c

Parameter	**Value**	**Reference**
V	8.8×10^{-3} L	see text
v	8.8×10^{-13} L	see text
k_a	2.6×10^{6} M^{-2} s^{-1}	Lewis and Deen, 1994
$C^{o}_{O_2}$	223 μM	Lange, 1967

Symbols: V, liquid volume in the closed chamber; v, volume of a single cell; k_a, rate constant for autoxidation of NO; $C^{o}_{O_2}$, liquid-phase O_2 concentration in equilibrium with air.

diffuse within a tumor is much shorter than the weeks to months required for significant tumor growth. The time for diffusion over a distance d with diffusivity D_{NO} is approximately d^2/D_{NO}, or about 2 h for $L = 4$ mm and $D_{NO} = 2.0 \times 10^{-5}$ cm^2/s. Second, the NO concentration will vary with position, declining with increasing distance from sites of NO synthesis, according to the competition between rates of diffusion and consumption. Third, anatomical dimensions and the locations of different cell types must be taken into account.

In general, the simultaneous synthesis, diffusion, and consumption of NO under steady-state conditions in a given tissue is described by

$$D_{NO}\nabla^2 C_{NO} + k_g - k_c C_{NO} - 4k_a C_{NO}{}^2 C_{O_2} = 0 \tag{4.9}$$

where ∇^2 is the Laplacian operator. The application of this conservation equation to melanoma is simplified by the fact that NO consumption by cells is rapid enough to localize the elevations in NO concentration. The length scale which results from the competition between diffusion and cellular consumption is $(D_{NO}/k_c)^{1/2}$, and our results for melanoma indicate that this is only a few tens of μm, as will be shown. For this reason, and because NO synthesis appears to occur mainly in a thin layer of macrophages surrounding the tumor, only the edges of the melanoma had to be modeled. Moreover, for length scales less than about 100 μm, autoxidation is too slow to compete with diffusion and cellular consumption, so that the k_a term in Eq. 4.9 could be neglected. Because the O_2 concentration appears only in the autoxidation term, it was unnecessary to solve a second differential equation for O_2. The rationale for these approximations is discussed further in Appendix B.

Based on the foregoing, the modeling could be confined to three adjacent regions at the periphery of the tumor. As depicted in Figure 4.1b, the regions correspond to tumor cells, stroma with macrophages, and dermal tissue, respectively. Because the thickness of the regions modeled is much smaller than the dimensions of invasive melanomas (typically on the order of several mm), tumor shape is unimportant and position (*x*) could be measured relative to the tumor-macrophage boundary, as shown. The simplified form of Eq. 4.9 is

$$D_{NO}\frac{d^2C_{NO}}{dx^2}+k_g-k_cC_{NO}=0 \tag{4.10}$$

In subsequent expressions, the concentrations in the melanoma (C_{NO}) are distinguished from those in the stroma region ($\tilde{C}_{NO}$) and dermal tissue ($\bar{C}_{NO}$). In particular, in the stroma, where macrophages and stromal tissue cells are present, Eq. 4.10 becomes:

$$D_{NO}\frac{d^2\tilde{C}_{NO}}{dx^2}+\phi\tilde{k}_g-\tilde{k}_c\tilde{C}_{NO}=0 \tag{4.11}$$

where ϕ is the volume fraction of macrophages in the region and all other parameters are the same as those previously defined. The baseline model assumes the tumor stroma is composed entirely of macrophages (ϕ = 1), and represents an upper bound for NO concentrations in melanomas. Inherent in Equation 4.11 is the assumption that stromal tissue cells do not synthesize NO but that they consume NO at the same rate as macrophages. The general solutions to Eq. 4.10 for the three regions are:

$$C_{NO}(x)=Ae^{x\sqrt{k_c/D_{NO}}}+k_g/k_c \qquad (-\infty\le x\le 0) \tag{4.12}$$

$$\tilde{C}_{NO}(x)=B\cosh\left(\sqrt{\tilde{k}_c/D_{NO}}\,x\right)+C\sinh\left(\sqrt{\tilde{k}_c/D_{NO}}\,x\right)+\phi\tilde{k}_g/\tilde{k}_c \qquad (0\le x\le L) \tag{4.13}$$

$$\bar{C}_{NO}(x)=De^{-x\sqrt{\bar{k}_c/D_{NO}}} \qquad (L\le x\le\infty) \tag{4.14}$$

The constants *A*, *B*, *C*, and *D* were evaluated by matching NO concentrations and fluxes at the melanoma-macrophage and macrophage-dermal tissue interfaces. The somewhat lengthy expressions are given in Appendix B.

4.2.6. Parameter Values

The baseline parameter values are given in Table 4.2; unless otherwise stated, all calculations were done using these values. The diffusivity of NO was taken to be two-thirds of its aqueous value, which is the intracellular/aqueous diffusivity ratio for O_2 [Ellsworth and Pittman, 1983]. Use of the oxygen diffusivity ratio is justified by the nearly identical diffusional characteristics of NO and O_2 in water [Zacharia and Deen, 2005]. The thickness of the macrophage region, *L,* assumes a single layer of cells with average diameters of 15 μm [Leskovar, *et al.,* 2000].

Whereas intracellular consumption takes place in all three domains, synthesis is assumed to occur only in the macrophage region for the baseline model. As indicated in the Results, we were unable to detect NO production by A375 melanoma cells. The rates of NO production and consumption for macrophages ($\tilde{k}_g$, $\tilde{k}_c$) in Table 4.2 are based on direct measurements in primary bone marrow-derived macrophages activated with recombinant mouse interferon-γ (IFN-γ) and *Escherichia coli* lipopolysaccharide (LPS). As described in Chapter 3, cellular kinetic parameters were determined by monitoring time-dependent NO and O_2 concentrations in a closed chamber and fitting data to a kinetic model, similar to what was done in the present study. The rates of NO consumption by melanoma cells, measured using the method described earlier, are described fully in the Results. Cellular NO consumption in the dermal tissue was assumed to be equivalent to that in macrophages. It has been found, for example, that NO consumption rates in TK6 cells (a human lymphoblastoid cell line) are roughly the same as those in RAW264.7 cells [Nalwaya and Deen, 2005] and [Wang et al., 2003].

Table 4.2. Baseline Values of Diffusivities, Rate Constants, Concentrations and Length Scales for Melanoma Model

Parameter	Value	Reference
$D_{NO}, \tilde{D}_{NO}, \bar{D}_{NO}$	2.0×10^{-5} cm^2/s	See text
L	15 μm	Leskovar, et al., 2000
k_g	0	This work, see text
$\tilde{k}_g$	2.4 μM/s	Chapter 3
k_c	7.1 s^{-1}	This work, see text
$\tilde{k}_c, \bar{k}_c$	1.3 s^{-1}	Chapter 3

4.3. Results

4.3.1. NO Synthesis by A375 Cells

NO production by A375 melanoma cells was not detected using Griess assays, even with the addition of systemic inflammatory factors, TNF-α (50 ng/mL) and IFN-γ (100 U/mL), which induce iNOS expression in various other cell types [Maciejewski, et al. 1995; Bogdan, 2001]. Moreover, previous works have measured nitrite accumulation, as assessed with the Griess assay, for other NO-producing cell types [Gellar, et al., 1993; Chan et al., 1999]. Thus, because melanoma cells appear to generate NO at rates low enough to be considered negligible compared to macrophages, NO synthesis by melanoma cells (k_g) was assumed to be zero for the baseline case.

4.3.2. NO Consumption in Media

Figure 4.2 shows representative results for NO concentrations as a function of time in DMEM with HEPES, measured in the absence of cells and in the dark. After the injection of saturated NO solution at $t = 0$, the NO concentration decreased due to consumption from the autoxidation reaction and from media-generated O_2^-. The NO decline from autoxidation alone (in a separate experiment) is also shown; the difference between these curves represents NO consumption from media-generated O_2^-. Averaged over all experiments, the consumption of NO by DMEM in the dark (k_m), attributable to O_2^- production from HEPES [Keynes *et al.,* 2003], was found to be 0.5 ± 0.3 nM s^{-1} (n = 3) and is in good agreement with previously reported values [Nalwaya and Deen, 2005]. As shown by a comparison of the curves corresponding to the calculated and measured NO concentrations, the kinetic model accurately fit the measured data.

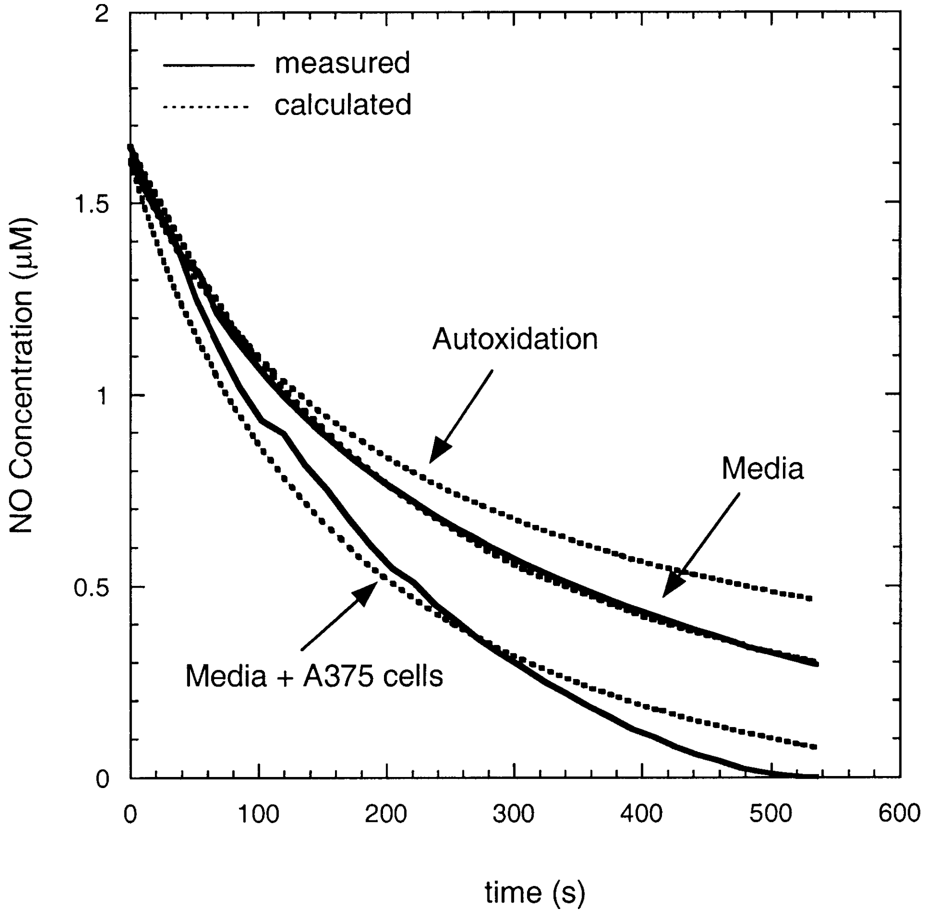

Figure 4.2. NO consumption by culture media (DMEM with HEPES) in the absence or presence (solid black) of A375 melanoma cells (4.5 × 10^6 cells) at 37°C in the dark. Shown is a representative plot of NO concentration as a function of time after an injection of ~ 1 μM of saturated NO solution (at t = 0). Also shown is the predicted NO decay from autoxidation reaction alone. The dashed curves were calculated using the kinetic model, using the best-fit values of k_{m} and k_c for the respective experiments.

4.3.3. NO Consumption by A375 cells

Figure 4.2 also shows the NO concentration in a representative experiment designed to determine the rate constant for NO consumption by A375 cells. The concentration decrease following injection of the saturated NO solution was more rapid than with media alone, the difference being attributable to cellular NO consumption. The rate constant for intracellular NO consumption by A375 melanoma cells was determined to be $7.1 \pm 0.8\ s^{-1}$. (The mean value is that given already as k_c in Table 4.2.)

4.3.4. Predicted NO Concentration Profiles

Figure 4.3 shows NO concentrations, calculated with the baseline model parameters, as a function of position (relative to the edge of the tumor) within the melanoma, macrophage, and dermal regions. In this and subsequent plots, the macrophage monolayer extends from $x = 0$ to $x = 15\ \mu m$. As shown, the NO concentration reaches a maximum of 0.22 μM in the macrophage region and declines rapidly in the melanoma and dermal regions; in the melanoma tumor, roughly 90% of the NO is consumed within 30 μm of the macrophage layer. In the dermis, NO decays slightly slower due to the lower rates of NO consumption assumed in the tissue, and gives rise to a NO profile that is not symmetrical about the macrophage layer.

4.3.5. Effect of Varying Macrophage Density

Although there are limited data on macrophage counts, the assessment of tumor-infiltrating macrophages appears to be subject to great inter-observer variability [Busam *et al.*, 2001]. Moreover, in malignant melanoma, the pattern of the macrophage population changes in the course of tumor progression [Bröcker *et al.,*1988]. Given the uncertainty of the number and distribution of macrophages within the stroma, the effect of varying macrophage density on NO concentrations in the melanoma was also modeled. Macrophages were assumed to be distributed homogeneously in a layer of stromal tissue (of thickness, L) and the volume fraction of macrophages (ϕ) within the region was varied.

Concentration profiles for three different macrophage volume fractions (with $\phi = 1$ corresponding to the baseline monolayer model) are also depicted in Figure 4.3. Decreasing the volume fraction of macrophages from 1 to 0.5 and 0.1 has the effect of decreasing the overall volumetric NO synthesis rate, resulting in maximum NO concentrations of 0.1 and 0.02 μM respectively. Maximum NO concentrations increase linearly with increasing ϕ, which is a consequence of having a linear differential equation with one source term ($\phi\, \tilde{k}_g$ in Eq. 4.11).

4.3.6. Effect of Melanoma NO synthesis

Although the baseline model assumes NO is not generated within the melanoma, it is conceivable that melanoma cells synthesize NO at low rates. In modeling intratumoral NO production, the melanoma NO synthesis rate is assumed to be a fraction of the macrophage NO synthesis rate ($\tilde{k}_g$, Table 4.2). Thus, instead of decaying to zero, as seen in the baseline model, the NO concentration far from the macrophage monolayer is a balance of melanoma NO synthesis and intracellular consumption. The NO concentration profiles for the intratumoral synthesis model are compared with the baseline model in Figure 4.4, where the volumetric rate of NO synthesis in the tumor region (k_g) was assumed to be 10%, or 20% that of macrophages. NO concentrations as a function of position are depicted once again. As seen, the maximum NO concentration remains unchanged in the macrophage monolayer (0.22 μM), but with intratumoralNO synthesis, NO levels far from the macrophage layer are sustained at 35 and 70

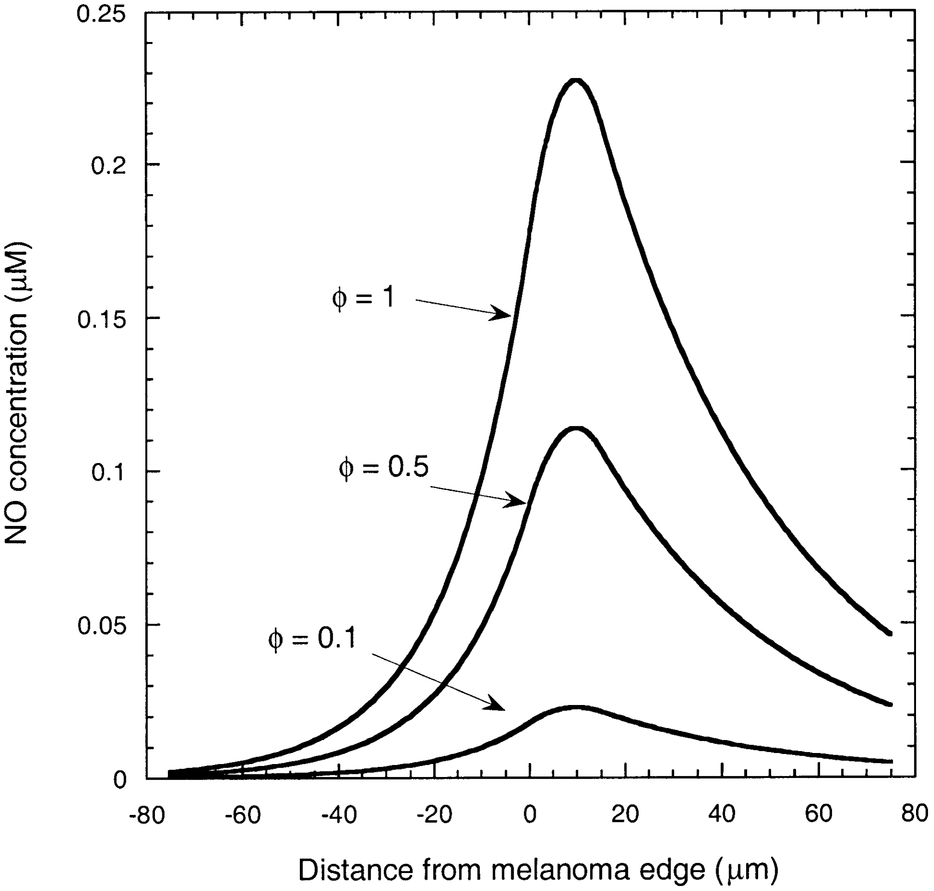

Figure 4.3. Predicted NO concentrations in the periphery of a tumor for the melanoma, macrophage, and dermis regions depicted in Figure 4.1b. Macrophage volume fractions are varied in the region extending from $x = 0$ to $x = 15$ μm. The baseline model assumes that this space was fully occupied by macrophages (i.e. $\phi = 1$, where ϕ is the volume fraction of macrophages) and two other macrophage densities are also depicted. All calculations employed the baseline parameter values listed in Table 4.2.

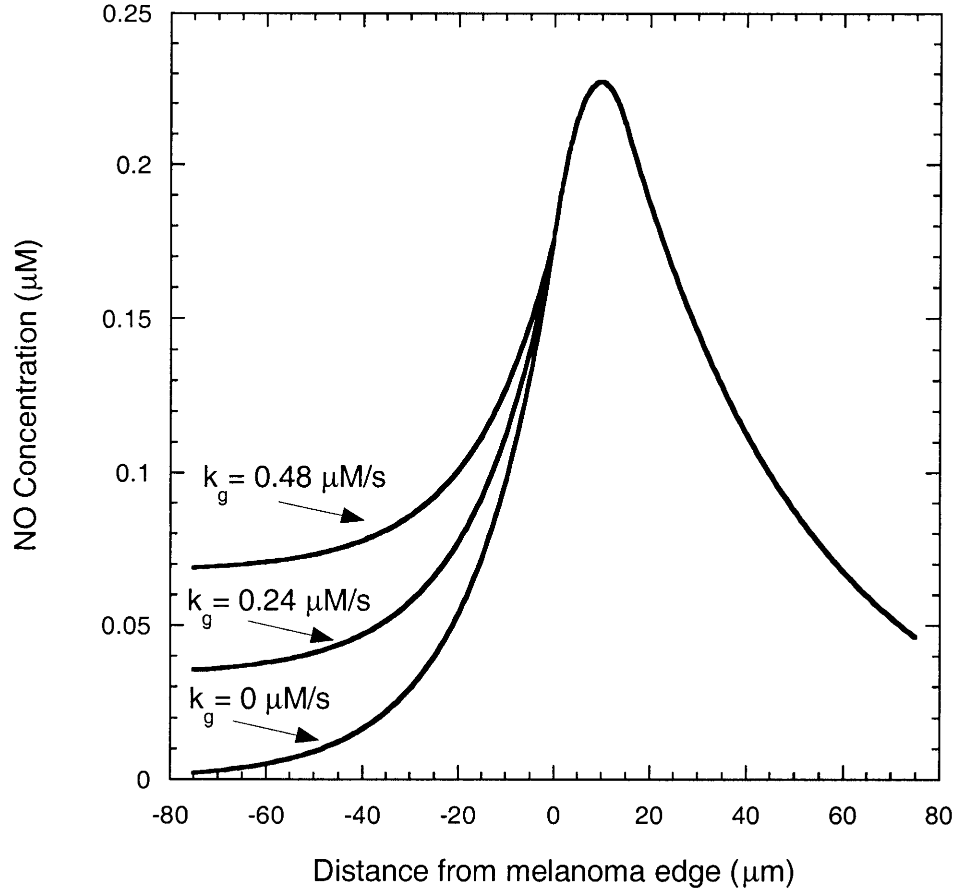

Figure 4.4. NO concentration as a function of distance from the edge of a melanoma with intratumoral NO synthesis. NO profiles in the melanoma, macrophage, and dermis are shown for various melanoma synthesis rates that correspond to 0% (same as baseline), 10%, or 20% of the macrophage NO synthesis rate.

Table 4.3. Comparison of rate constants for intracellular NO consumption by various mammalian cell types

Cell	Cell Type	k_c (s^{-1})	Reference
NH32	Human lymphoblast	0.1	Wang, 2003
TK6	Human lymphoblast	0.3	Wang, 2003
βTC3	Murine pancreatic β	1.7	Wang, 2003
RAW264.7	Murine macrophage	0.6-1.6	Nalwaya and Deen, 2005, Chin, et al., submitted 2009
BMDM	Murine macrophage	1.3	Chin, et al., submitted 2009
HCT116	Human colonic epithelial	4.1	Chin, et al., submitted 2009
A375	Human melanoma	7.1	this work
K9	Rat hepatocyte	2	Gardner et al., 2001
PC12	Rat adrenal pheochromocytoma	4	Gardner et al., 2001
K562	Human myelogenous leukemia	5	Gardner et al., 2001
MLE	Murine lung epithelial	9	Gardner et al., 2001
A549	Human lung adenocarcinoma	9	Gardner et al., 2001
Caco-2	Human colonic epithelial	38	Gardner et al., 2001

nM within the melanoma for $k_g = 0.24$ and 0.48 μM/s respectively.

4.4. Discussion

We developed a mathematical model to estimate spatially varying NO concentrations in a cutaneous melanoma. By using differential equations to describe rates of diffusion and reaction of NO in an idealized representation of a melanoma tumor, concentrations are obtained as a function of position. Key inputs in the model were the rates of NO synthesis and consumption by macrophages (previously determined [Nalwaya and Deen, 2005; Chin and Deen, 2010]) and melanoma cells. NO synthesis by A375 melanoma cells was not detected using Griess assays, which is consistent with previously published results. Although iNOS expression in A375 and MeWo cells has been demonstrated, NO levels in those studies were barely detectable in liquid culture [Zheng *et al.,* 2004]. Others have also reported negative Griess results for K-1735 C4 murine metastatic melanoma cells [Xie et al., 1995] and G361, a human melanoma cell line [Andrews et al., 1995]. The rate constant for cellular NO consumption by A375 was found to be 7.1 s^{-1} (k_c, Table 4.2), which is more than five-times the consumption rate for macrophages ($\tilde{k}_c$, Table 4.2) and on the upper end of reported values for other cell types including NH32 human lymphoblast (0.1 s^{-1}) , βTC3 pancreatic beta cells (1.7 s^{-1}) [Wang, 2003] , HCT116 (4.1 s^{-1}) [Chin et al., *submitted 2009*] and MLE murine lung epithelial cells (9 s^{-1}) [Gardner *et al.*, 2001] (see Table 4.3).

Given the diffusivity of NO and measured values for k_c, the length scale which results from the competition between diffusion and consumption (~20 μm) is small enough that intracellular reactions (such as with O_2^-, oxygen-ligated metals, and NO dioxygenases) are the only important pathways for NO consumption. NO consumption via reactions with oxyhemoglobin (Eq.4.3) was neglected because the average distance between blood vessels

[Dadras *et al.,* 2003; Kiss *et al.,* 2007] is large enough that NO is likely to be consumed intracellularly before it reaches any blood vessels. Extracellular consumption of NO by O_2^- was also omitted in modeling NO concentrations, for the reasons discussed earlier.

Autoxidation was also too slow to compete with diffusion and cellular NO consumption, allowing for NO concentrations to be uncoupled from local O_2 levels. Although the O_2 concentration distribution could potentially affect the rate of NO synthesis by iNOS, the Michaelis constant for oxygen-dependent production of NO by iNOS has been reported to be around 6 μM; iNOS is the least O_2-sensitive NOS isoform at low pO_2 [Rengasamy and Johns, 1996]. Even with the diffusion and cellular consumption of O_2 in tissue, given the supply of oxygen from proximity of the macrophages to blood vessels (~ 40 μm [Dadras et al, 2003; Kiss et al, 2007]), the rate of cellular respiration would need to be approximately 5-times the reported rate for macrophages [Nalwaya and Deen, 2005] for concentrations in the peritumoral region to be as low as 6 μM. Thus, it seems unlikely that O_2 availability would be a significant factor in iNOS-produced NO. Melanoma cells have also been shown to express the other constitutive isoforms of nitric oxide synthase (eNOS and nNOS) [Salvucci et al., 2001; Ahmed and Van Den Oord, 1999]. Although NO production from the other NOS isoforms may be more O_2-sensitive, eNOS and nNOS generate low levels of NO relative to iNOS [MacMicking, et al., 1997], so the overall NO concentrations are still unlikely to be significantly affected by variations in O_2 concentrations.

Incorporating these approximations into our mathematical model, NO concentrations were calculated for the edge of a melanoma, with maximum NO concentration (0.22 μM) occurring in the macrophage monolayer (Figure 4.3), and quickly decaying to zero within the tumor. Although the specific configuration of macrophages surrounding a tumor is unclear, the highest NO concentrations are elicited by macrophages grouped closely together so a stroma region comprised entirely of macrophages was used as our baseline model to represent the upper bound for NO exposure in a melanoma. The degree of macrophage infiltration in the tumor stroma has been shown to correlate with increased tumor depth and metastatic potential [Torisu *et al.,* 2000], and our model suggests that the volume fraction of macrophages in the stroma (within a 15 μm periphery of a tumor) must exceed 50% for melanoma NO concentrations to exceed 0.1 μM.

Intratumoral NO synthesis was also considered by assuming the volumetric rate of NO synthesis by melanoma cells was 10% or 20% of the macrophage NO synthesis rate. Alternatively, these results can also represent a scenario whereby 10% or 20% of the intratumoral cells are comprised of macrophages that have infiltrated and are distributed uniformly within the tumor mass. Unlike the baseline model, including melanoma NO synthesis results in NO concentrations that decay to non-zero levels in the tumor. Instead, the melanoma NO concentration far from the macrophage layer is a balance between the rates of synthesis and consumption (k_g/k_c). With autoxidation unimportant, the melanoma NO concentration is independent of local O_2 levels, and potential hypoxic conditions which can develop in the center of the tumor would not affect the predicted intratumoral melanoma NO concentrations.

On the other hand, increasing the hypothetical intratumoral NO synthesis rate proportionally increases the NO concentrations that persist in the tumor. Given that NO levels in liquid culture are low or undetectable with Griess assays, melanoma NO synthesis is likely to be much less than that of macrophages. Nevertheless, even if melanoma NO synthesis is 20% that of macrophages (equivalent to a synthesis rate of 0.5 μM/s), NO concentrations in the tumor are only 70 nM (Figure 4.4). Normal tissue NO concentrations are unlikely to exceed 50 nM

[Lamkin-Kennard *et al.*, 2004]. Thus, whether or not melanoma cells themselves synthesize NO, our model predicts that only cells at the periphery of the tumor are exposed to significantly elevated NO concentrations.

Including blood vessels as NO sinks in the intratumoral synthesis model also had a negligible effect on the melanoma NO concentrations far from the macrophage monolayer (~ 1% change). In fact, in applying a Krogh-type approach to represent homogeneously vascularized tissue, incorporating NO depletion by blood vessels only increased the effective NO consumption rate by 1.4%, as compared to intracellular NO consumption alone (see Appendix C for detailed analysis). This is because of the distance between blood vessels (~70 μm) based on reported intratumoral vascular densities [Dadras *et al.,* 2003; Kiss *et al.,* 2007].

The predicted NO concentrations are similar to results obtained by modeling NO in an inflamed colonic crypt [Chin *et al.*, 2008]. Despite the two different geometries and the different cell types involved, the small length scales and proximity to a monolayer of macrophages resulted in concentration predictions of ~0.2 μM in both models. Our model may offer some insight into the role NO plays in cutaneous melanoma tumor progression metastasis, which preferentially spreads via the lymphatic route [Giorgadze *et al.,* 2004]. Tumor cell proliferation has been shown to be most pronounced at the periphery of melanomas [Straume *et al.,* 2003]. Thus elevated NO levels may inhibit apoptosis in melanoma cells, leading to tumor growth along the edge and facilitating the invasion of lymphatics to eventually form distant metastases. In addition, the presence of iNOS has been correlated to lymphatic vessel densities in metastatic melanomas, with higher vessel densities occurring in the peritumoral areas [Massi *et al.,* 2009]. At the concentration levels predicted by our model, NO may also contribute to lymphatic vascular formation in melanomas. NO has been shown to act as a lymphangiogenic factor through interaction with VEGF-C in breast cancer and head and neck squamous cell carcinomas [Franchi *et al.,* 2006; Nakamura *et al.,* 2006]. Facilitating lymphatic spread through pre-existing lymphatics or by *de novo* lymphangiogenesis are just two of the many possible mechanisms by which NO may contribute to the metastasis of melanomas. With NO concentration predictions, the intracellular concentrations of other reactive nitrogen species can also be calculated [Lim *et al.,* 2008], which should facilitate efforts to probe the effects of NO and its reactive products on the pathophysiological progression of melanomas.

Appendix A: Analytical Solution for NO Concentrations near Spherical Macrophage Aggregates

Following is a derivation of expressions that describe the steady-state NO concentration in a situation in which a spherical macrophage (or spherical aggregate of tightly packed macrophages) of radius *R* is surrounded by a large volume of lamina propria tissue. It is assumed that NO is synthesized in the macrophage (or aggregate) at a constant rate, and is consumed in both regions by first-order reactions. Given the symmetry, the concentration in each region is a function only of the spherical radial coordinate *r*, measured from the aggregate center. Defining the dimensionless radial position as $\eta = r/R$, and dimensionless concentrations in the macrophage and lamina propria regions as $\bar{\theta} = \bar{C}_{NO} / C^*_{NO}$ and $\hat{\theta} = \hat{C}_{NO} / C^*_{NO}$, respectively, Eq. 2.9 for the two regions becomes

$$\frac{1}{\eta^2}\frac{\partial}{\partial r}\left(\eta^2 \frac{\partial \bar{\theta}}{\partial \eta}\right) + 1 - \beta\bar{\theta} = 0 \qquad (0 \leq \eta \leq 1) \qquad \text{(A1)}$$

$$\frac{1}{\eta^2}\frac{\partial}{\partial r}\left(\eta^2 \frac{\partial \hat{\theta}}{\partial \eta}\right) - \beta\hat{\theta} = 0 \qquad (\eta \geq 1) \qquad \text{(A2)}$$

where $\beta = k_c R^2 / D_{NO}$ and $C^*_{NO} = k_g R^2 / D_{NO}$. Equations A1 and A2 are each particular forms of the modified spherical Bessel equation. Their general solutions are

$$\bar{\theta}(\eta) = \frac{A \sinh\sqrt{\beta}\eta}{\eta} + \frac{1}{\beta} \qquad \text{(A3)}$$

$$\hat{\theta}(\eta) = \frac{B \sinh\sqrt{\beta}\eta}{\eta} + \frac{C \cosh\sqrt{\beta}\eta}{\eta} \qquad \text{(A4)}$$

where A, B, and C are constants. Imposed already in Eq. A3 is the requirement that the concentration be finite at $\eta = 0$. The constants were evaluated by requiring that $\bar{\theta} = \hat{\theta}$ and $d\bar{\theta}/d\eta = d\hat{\theta}/d\eta$ at $\eta = 1$, and that $\hat{\theta} = 0$ at $\eta = \infty$. The results are

$$A = -\frac{\left(1+\sqrt{\beta}\right)}{\beta^{3/2}\left(\sinh\left(\sqrt{\beta}\right)+\cosh\left(\sqrt{\beta}\right)\right)} \tag{A5}$$

$$B = -\frac{\beta\left(1+\sqrt{\beta}\right)\sinh\left(\sqrt{\beta}\right)+1}{\beta^{5/2}\left(\sinh\left(\sqrt{\beta}\right)^2-\cosh\left(\sqrt{\beta}\right)^2\right)} \tag{A6}$$

$$C = \frac{\beta\left(1+\sqrt{\beta}\right)\sinh\left(\sqrt{\beta}\right)+1}{\beta^{5/2}\left(\sinh\left(\sqrt{\beta}\right)^2-\cosh\left(\sqrt{\beta}\right)^2\right)}. \tag{A7}$$

To obtain dimensional concentrations (as plotted in Figure 2.9), the concentrations in Eqs. A3 and A4 were each multiplied by $k_g R^2 / D_{NO}$.

Appendix B: Analytical Solution for NO Concentrations at the Edge of a Melanoma

The magnitude of physical dimensions relative to NO consumption length scales $\left(D_{NO} / k_c\right)^{1/2}$ allowed for the melanoma and dermis regions to be modeled as infinite domains. As such, the geometry of the melanoma tumor itself was unimportant and a simplified 1-dimensional reaction-diffusion model comprised of three adjacent domains was used to calculate NO concentrations at the tumor edge. Following is a derivation of expressions that were used to calculate the steady-state NO concentrations in the melanoma regions depicted in Figure 4.1b. For purposes of simplification, scaled dimensionless variables were defined, $\theta = C_{NO} / C_{NO}^*$, $\psi = C_{O_2} / C_{O_2}^*$, and $\chi = x/L$. The concentration scale for oxygen ($C_{O_2}^*$) is the O_2 concentration in venous blood (58 μM), whereas the concentration scale for nitric oxide (C_{NO}^*) will be defined subsequently. The length scale, *L*, is the thickness of the macrophage monolayer (15 μm, Table 4.2). The dimensionless form of Eq. 4.9 is thus:

$$\nabla^2\theta + \left(\frac{k_g L^2}{D_{NO} C_{NO}^*}\right) - \left(\frac{k_c L^2}{D_{NO}}\right)\theta - \frac{4 k_a C_{O_2}^* C_{NO}^* L^2}{D_{NO}} \theta^2 \psi = 0 \qquad \text{(B1)}$$

Although the same symbol is used as before, ∇^2 in Eq. (B1) is now dimensionless (i.e., L^2 times that in Eq. 4.9. The concentration scale for NO was determined primarily by the rate of NO synthesis. Since NO is assumed to be produced mainly in the macrophage layer, the coefficient of the first reaction term in Eq. B1 was set equal to unity for that region. The resultant NO concentration scale was thus $C_{NO}^* = 0.27$ μM; our analytical solutions confirmed that this is a good estimate of the maximum order of magnitude of C_{NO}.

The coefficient of the autoxidation term in Eq. B1 is a Damköhler number that measures the importance of autoxidation relative to diffusion. It is denoted as

$$\gamma = \frac{4k_a C^*_{O_2} C^*_{NO} L^2}{D_{NO}} \tag{B2}$$

Substituting the corresponding values from **Tables 4.1** and 4.2 into Eq. B2, $\gamma << 1$, implying that autoxidation does not significantly affect the NO concentration and is justification for neglecting the autoxidation in our calculations. Eq. B1. thus becomes:

$$\frac{d^2\theta}{d\chi^2} + \alpha - \beta\theta = 0 \tag{B3}$$

where the α and β are the Damköhler numbers for NO synthesis and intracellular consumption, respectively, given by:

$$\alpha = \frac{k_g L^2}{D_{NO} C^*_{NO}} \tag{B4}$$

$$\beta = \frac{k_c L^2}{D_{NO}} \tag{B5}$$

Equation B3 was solved analytically for all three regions in Figure 4.1b using region-specific values of α and β. The general solution to B3 (dimensionless form of Eqs. 4.10-4.12) is:

$$\theta = Ae^{\sqrt{\beta}\chi} + \alpha/\beta \qquad (-\infty \le \chi \le 0) \tag{B6}$$

$$\tilde{\theta} = B\cosh\left(\sqrt{\tilde{\beta}}\chi\right) + C\sinh\left(\sqrt{\tilde{\beta}}\chi\right) + \phi\tilde{\alpha}/\tilde{\beta} \qquad (0 \le \chi \le 1) \tag{B7}$$

$$\bar{\theta} = De^{-\sqrt{\bar{\beta}}\chi} \qquad (1 \le \chi \le \infty) \tag{B8}$$

As before, ϕ represents the volume fraction of macrophages in the stroma; in the baseline model, ϕ was assumed to be 1. The constants *A, B, C, D* were evaluated by requiring that $\theta = \tilde{\theta}$,$d\theta / d\chi = d\tilde{\theta} / d\chi$ and $\tilde{\theta} = \bar{\theta}$, $d\tilde{\theta} / d\chi = d\bar{\theta} / d\chi$ at $\chi = 0$ and $\chi = 1$, respectively (i.e. matching concentrations and fluxes across the melanoma/macrophage and macrophage/dermal tissue interfaces). The results are:

$$A=\frac{\left(\frac{-\phi\tilde{\alpha}\sqrt{\beta}\sinh\left(\sqrt{\tilde{\beta}}\right)}{\tilde{\beta}^{3/2}}+\frac{\phi\tilde{\alpha}}{\tilde{\beta}}\right)\sqrt{\bar{\beta}}-\frac{\phi\tilde{\alpha}\sqrt{\beta}\cosh\left(\sqrt{\tilde{\beta}}\right)}{\tilde{\beta}}}{\left(\cosh\left(\sqrt{\tilde{\beta}}\right)+\frac{\sqrt{\beta}\sinh\left(\sqrt{\tilde{\beta}}\right)}{\sqrt{\tilde{\beta}}}\right)\sqrt{\bar{\beta}}+\sqrt{\tilde{\beta}}\sinh\left(\sqrt{\tilde{\beta}}\right)+\sqrt{\beta}\cosh\left(\sqrt{\tilde{\beta}}\right)}+\frac{\phi\tilde{\alpha}}{\tilde{\beta}}-\frac{\alpha}{\beta} \qquad \text{(B9)}$$

$$B=\frac{\left(\frac{-\phi\tilde{\alpha}\sqrt{\beta}\sinh\left(\sqrt{\tilde{\beta}}\right)}{\tilde{\beta}^{3/2}}+\frac{\phi\tilde{\alpha}}{\tilde{\beta}}\right)\sqrt{\bar{\beta}}-\frac{\phi\tilde{\alpha}\sqrt{\beta}\cosh\left(\sqrt{\tilde{\beta}}\right)}{\tilde{\beta}}}{\left(\cosh\left(\sqrt{\tilde{\beta}}\right)+\frac{\sqrt{\beta}\sinh\left(\sqrt{\tilde{\beta}}\right)}{\sqrt{\tilde{\beta}}}\right)\sqrt{\bar{\beta}}+\sqrt{\tilde{\beta}}\sinh\left(\sqrt{\tilde{\beta}}\right)+\sqrt{\beta}\cosh\left(\sqrt{\tilde{\beta}}\right)} \qquad \text{(B10)}$$

$$C=\frac{\sqrt{\beta}\left(\frac{-\phi\tilde{\alpha}\sqrt{\beta}\sinh\left(\sqrt{\tilde{\beta}}\right)}{\tilde{\beta}^{3/2}}+\frac{\phi\tilde{\alpha}}{\tilde{\beta}}\right)\sqrt{\bar{\beta}}-\frac{\phi\tilde{\alpha}\sqrt{\beta}\cosh\left(\sqrt{\tilde{\beta}}\right)}{\tilde{\beta}}}{\sqrt{\tilde{\beta}}\left(\cosh\left(\sqrt{\tilde{\beta}}\right)+\frac{\sqrt{\beta}\sinh\left(\sqrt{\tilde{\beta}}\right)}{\sqrt{\tilde{\beta}}}\right)\sqrt{\bar{\beta}}+\sqrt{\tilde{\beta}}\sinh\left(\sqrt{\tilde{\beta}}\right)+\sqrt{\beta}\cosh\left(\sqrt{\tilde{\beta}}\right)}+\frac{\phi\tilde{\alpha}\sqrt{\beta}}{\tilde{\beta}^{3/2}} \qquad \text{(B11)}$$

$$D=\frac{\left(\cosh\left(\sqrt{\tilde{\beta}}\right)\frac{\sqrt{\beta}\sinh\left(\sqrt{\tilde{\beta}}\right)}{\sqrt{\tilde{\beta}}}\right)+\left(\frac{-\phi\tilde{\alpha}\sqrt{\beta}\sinh\left(\sqrt{\tilde{\beta}}\right)}{\tilde{\beta}^{3/2}}+\frac{\phi\tilde{\alpha}}{\tilde{\beta}}\right)\sqrt{\bar{\beta}}-\frac{\phi\tilde{\alpha}\sqrt{\beta}\cosh\left(\sqrt{\tilde{\beta}}\right)}{\tilde{\beta}}}{e^{-\sqrt{\bar{\beta}}}\left(\cosh\left(\sqrt{\tilde{\beta}}\right)+\frac{\sqrt{\beta}\sinh\left(\sqrt{\tilde{\beta}}\right)}{\sqrt{\tilde{\beta}}}\right)\sqrt{\bar{\beta}}+\sqrt{\tilde{\beta}}\sinh\left(\sqrt{\tilde{\beta}}\right)+\sqrt{\beta}\cosh\left(\sqrt{\tilde{\beta}}\right)} \qquad \text{(B12)}$$

$$+\frac{\frac{\phi\tilde{\alpha}\sqrt{\beta}\sinh\left(\sqrt{\tilde{\beta}}\right)}{\tilde{\beta}^{3/2}}+\frac{\phi\tilde{\alpha}}{\tilde{\beta}}}{e^{-\sqrt{\tilde{\beta}}}}$$

To obtain dimensional concentrations (as plotted in Figures 4.3 and 4.4), the concentrations in Eqs. B6-B8 were each multiplied by C_{NO}^*.

Appendix C: Modeling Intratumoral Blood Vessels for Melanoma Model

To probe the effects of including blood vessels in the intratumoral NO synthesis model, a Krogh-type approach was used to solve for an effective volumetric first-order rate constant for total NO consumption in a vascularized tumor (k_c'). This approximation is only appropriate for considering bulk or average properties of tissue on larger length scales, as is the case with the intraumoral NO synthesis model. Briefly, two concentric cylinders were used to represent a single blood vessel (inner cylinder) surrounded by a unit cell of tumor tissue (outer cylinder). The governing equation and boundary conditions for NO concentrations in an annulus of (extravascular) melanoma tissue is thus:

$$\left[\frac{1}{r}\frac{\partial}{\partial r}\left(r\frac{\partial C_{NO}}{\partial r}\right)\right]-\frac{k_c C_{NO}}{D_{NO}}=0 \tag{C1}$$

$$C_{NO}\left(R_1\right)=0 \tag{C2}$$

$$C_{NO}\left(R_2\right)=X \tag{C3}$$

Where k_c is the first-order rate constant for intracellular NO consumption (as previously defined), R_1 is the radius of a capillary (approximated as 5μm [Tufto and Rofstad, 1999], and R_2 is the distance between blood vessels (70 μm [Dadras et al, 2003; Kiss et al, 2007]). The boundary conditions are such that NO is assumed to be consumed instantaneously at the surface of the blood vessel (the inner radius of the annulus) due to the fast reaction with oxyhemoglobin (Eq. C2), and the NO concentration at the outer boundary of the annulus is an arbitrary constant (Eq. C3).

The solution to Eq. C1 is:

$$C\left(r\right)=A_1 I_o\left(mr\right)+A_2 K_o\left(mr\right) \tag{C4}$$

$$A_1 = \frac{X}{I_o(mR_2) - \frac{I_o(mR_1)K_o(mR_2)}{K_o(mR_1)}} \tag{C5}$$

$$A_2 - \frac{XI_o(mR_1)}{K_o(mR_1)\left(I_o(mR_2) - \frac{I_o(mR_1)K_o(mR_2)}{K_o(mR_1)}\right)} \tag{C6}$$

Where $m = (k_c / D_{NO})^{1/2}$, I_0 and I_1, K_0, and K_1 are the modified Bessel functions of the first and second kind, respectively. With an expression for NO concentrations in the annulus, the average volumetric NO consumption rate for a cylinder of vascularized tumor tissue is given by:

$$\frac{(2\pi R_2 L) D \left.\frac{\partial C}{\partial r}\right|_{R_2}}{\pi(R_2^{\,2} - R_1^{\,2})L} = k_c' C_{NO}' \tag{C7}$$

Where the left hand side of Eq. C7 represents the total flux of NO into the cylinder at R_2 and C_{NO}' is the average extravascular NO concentration (i.e. A16 averaged over the entire annulus volume). Thus, the effective first-order rate constant for total NO consumption, k_c', is given by:

$$k_c' = \frac{k_c R_2\left[K_o(mR_1)I_1(mR_2) + I_o(mR_1)K_1(mR_2)\right]}{K_o(mR_1)\left(R_2 I_1(mR_2) - R_1 I_1(mR_1)\right) + I_o(mR_1)\left(R_2 K_1(mR_2) - R_1 K_1(mR_1)\right)} \tag{C8}$$

From Eq. C8, it is seen that embedded in the effective rate for NO consumption for vascularized tumor tissue is k_c, the intracellular NO consumption rate; the additional terms capture the additional consumption from having NO sinks/blood vessels distributed homogeneously throughout the region. Note that the arbitrary constant, X, which appears in Eq. C4-C6 is canceled out in solving for k_c'.

Plugging in values of R_1, R_2, m, and k_c (for A375 cells listed in Table 3.2) into Eq. C8, the value for k_c' in the melanoma is 7.2 s^{-1}, which is only 1.4% larger than k_c (7.1 s^{-1}). As such, using k_c' instead of k_c has a negligible effect on the calculated intratumoral NO concentration (k_g/k_c).

Appendix D: Experimental Data

Summary of Experimental Data Plots

Figures	Description	Corresponding Chapter
D.1-D.3	O_2 consumption by unactivated RAW264.7 cells	Chapter 3 (Figure 3.3)
D.4-D.6	O_2 consumption by unactivatd BMDM	Chapter 3 (Figure 3.4)
D.7-D.9	O_2 consumption by unactivatd HCT116 cells	Chapter 3 (Figure 3.5)
D.10-D.11	Nitrite/nitrate accumulation for IFNγ/LPS-treated macrophages	Chapter 3
D.12-D.16	NO and O_2 measurements for IFNγ/LPS-activated BMDM	Chapter 3 (Figure 3.6)
D.17-D.21	NO and O_2 measurements for IFNγ/LPS-activated RAW264.7 cells	Chapter 3 (Figure 3.7)
D.21-D.26	NO and O_2 measurements for capsaicin/resveratrol-activated HCT116 cells	Chapter 3 (Figure 3.8)
D.27-D.29	Superoxide production by IFNγ/LPS-activated BMDM	Chapter 3 (Figure 3.11)
D.30-D.32	Superoxide production by IFNγ/LPS-activated RAW264.7 cells	Chapter 3 (Figure 3.12)
D.33-D.34	NO consumption in DMEM cell culture media	Chapter 4 (Figure 4.2)
D.35-D.39	NO consumption in A375 melanoma cells	Chapter 4 (Figure 4.2)

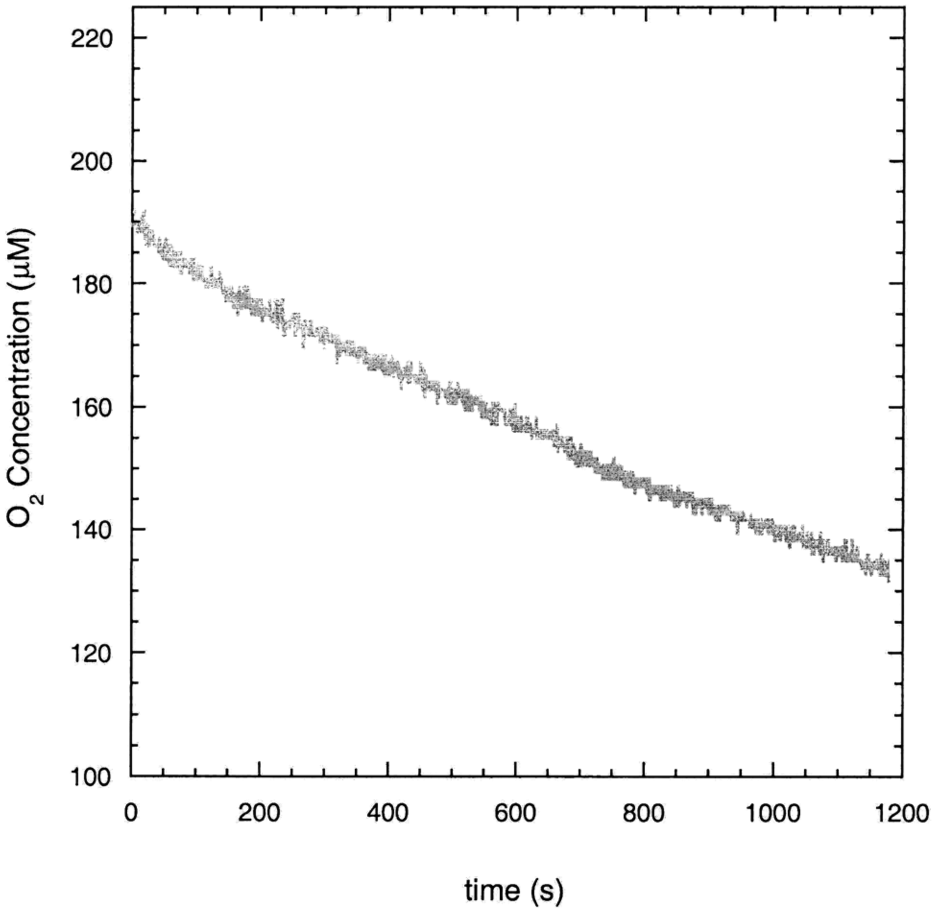

Figure D.1. Time dependence of O_2 concentrations for 12×10^6 unactivated RAW246.7 cells (Experiment 2).

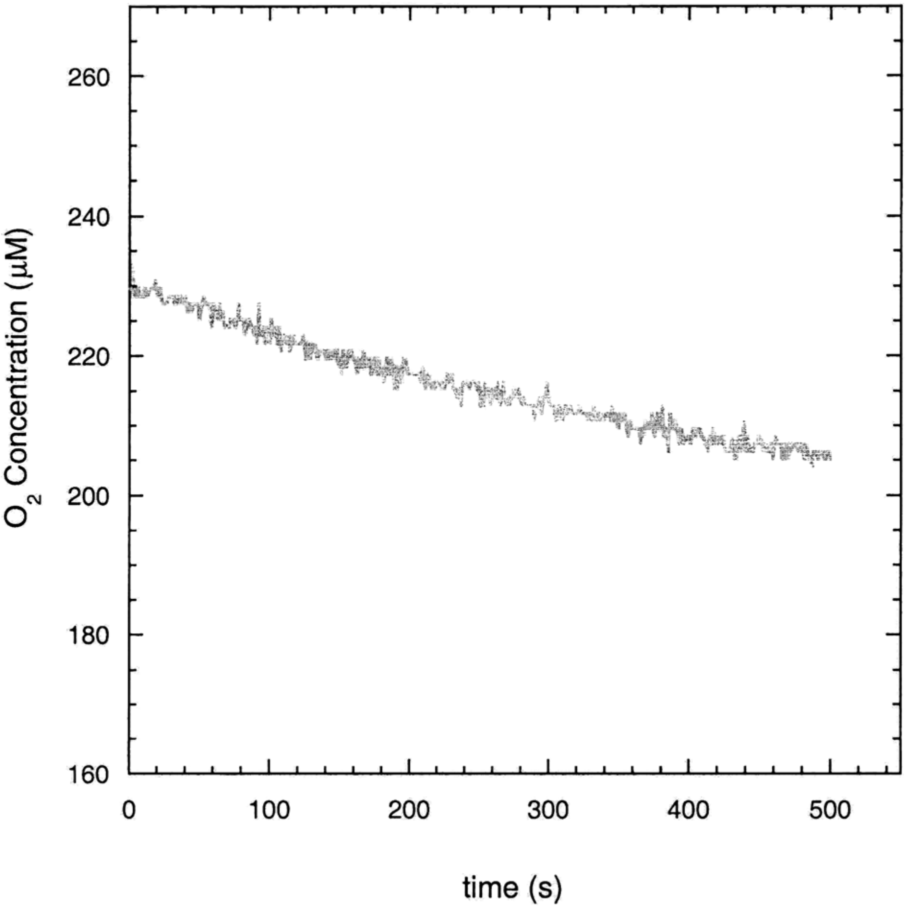

Figure D.2. Time dependence of O_2 concentrations for 9 $\times 10^6$ unactivated RAW246.7 cells (Experiment 3).

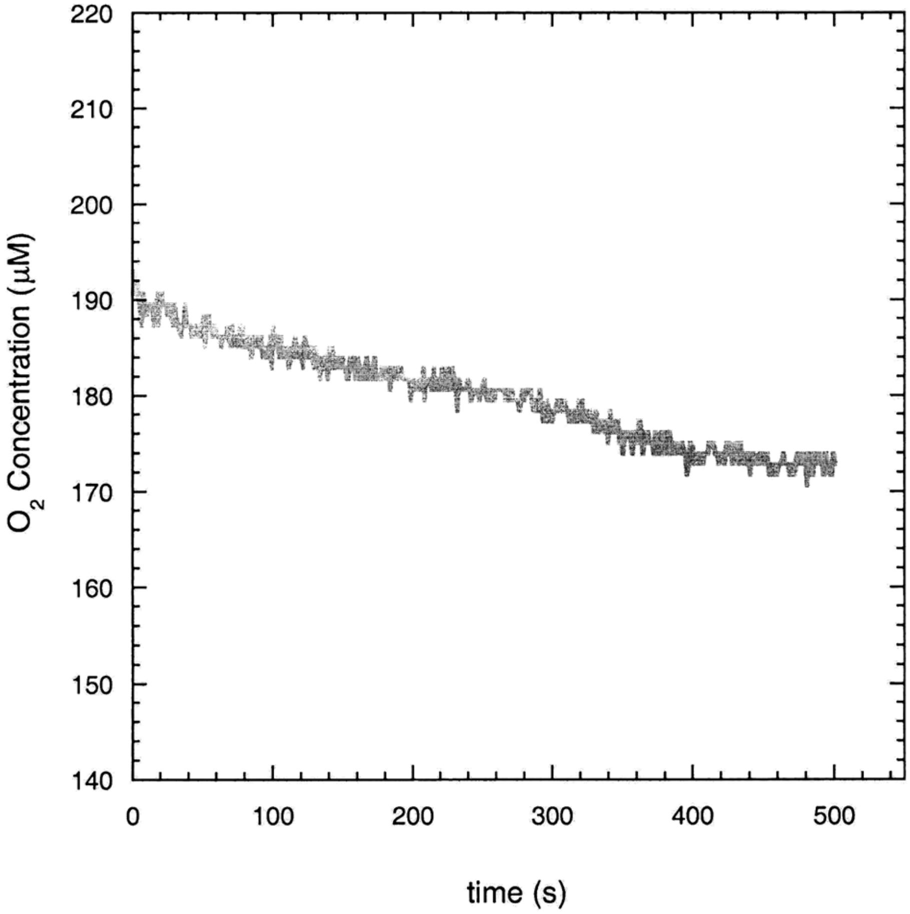

Figure D.3. Time dependence of O_2 concentrations for 10 $\times 10^6$ unactivated RAW246.7 cells (Experiment 4).

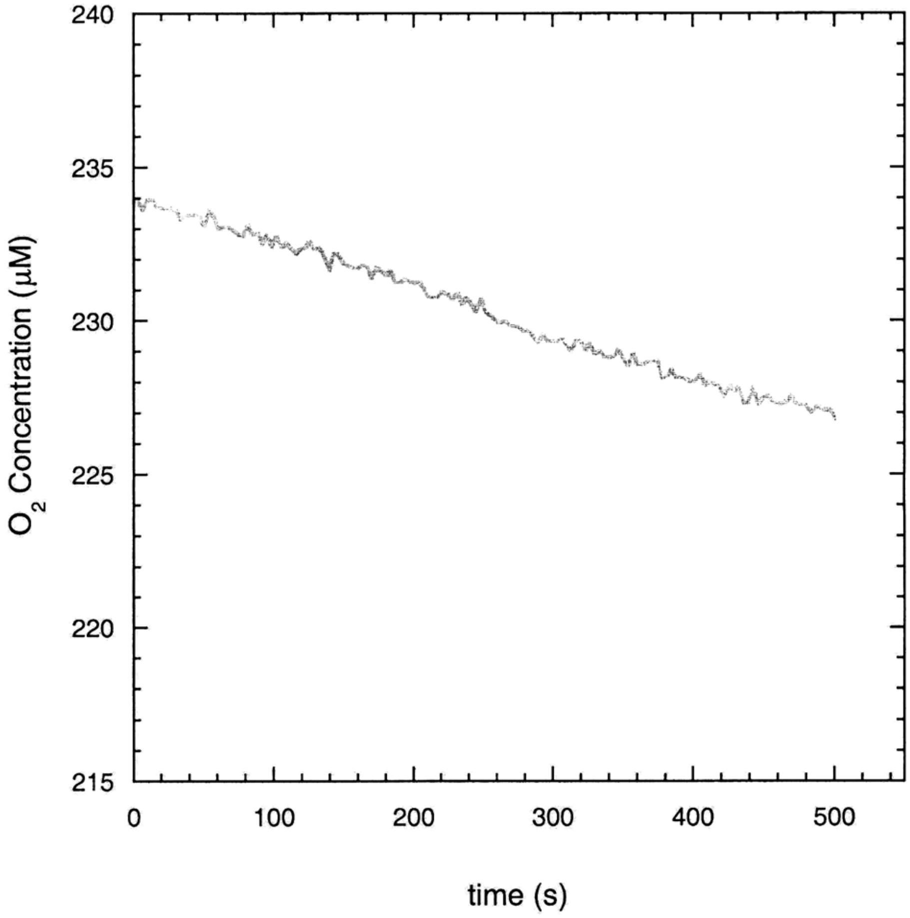

Figure D.4. Time dependence of O_2 concentrations for 4 $\times 10^6$ unactivated primary bone marrow-derived macrophages (Experiment 2).

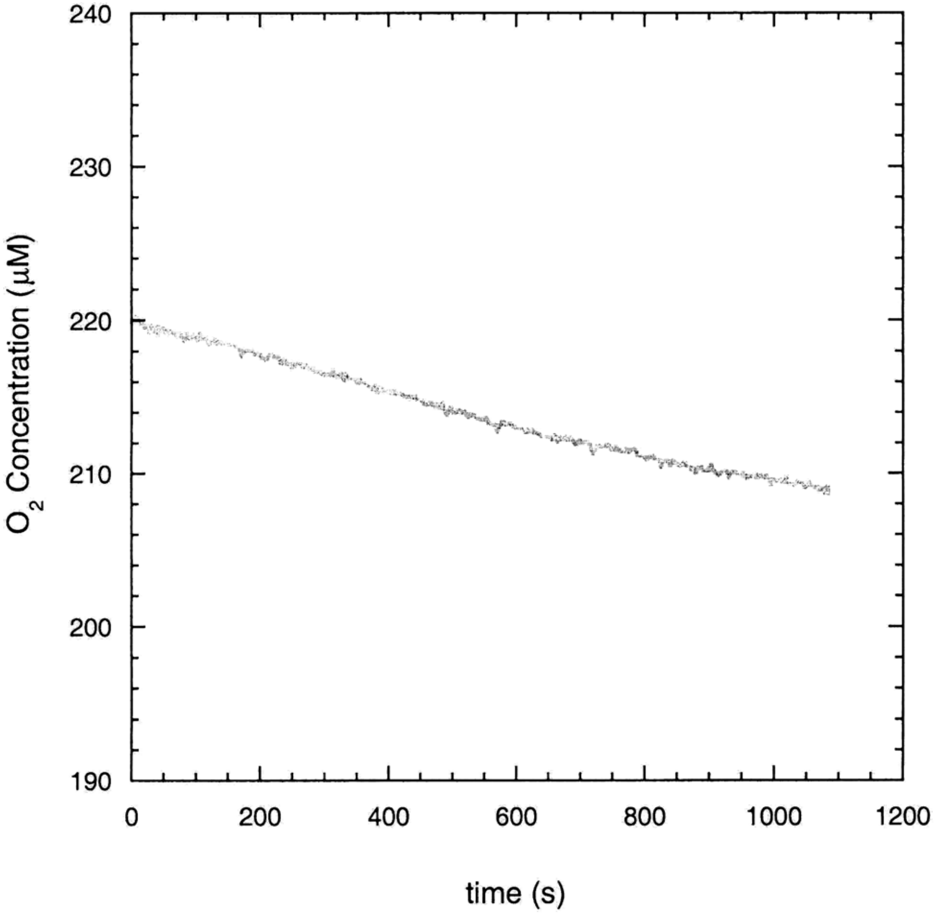

Figure D.5. Time dependence of O_2 concentrations for 5×10^6 unactivated primary bone marrow-derived macrophages (Experiment 3).

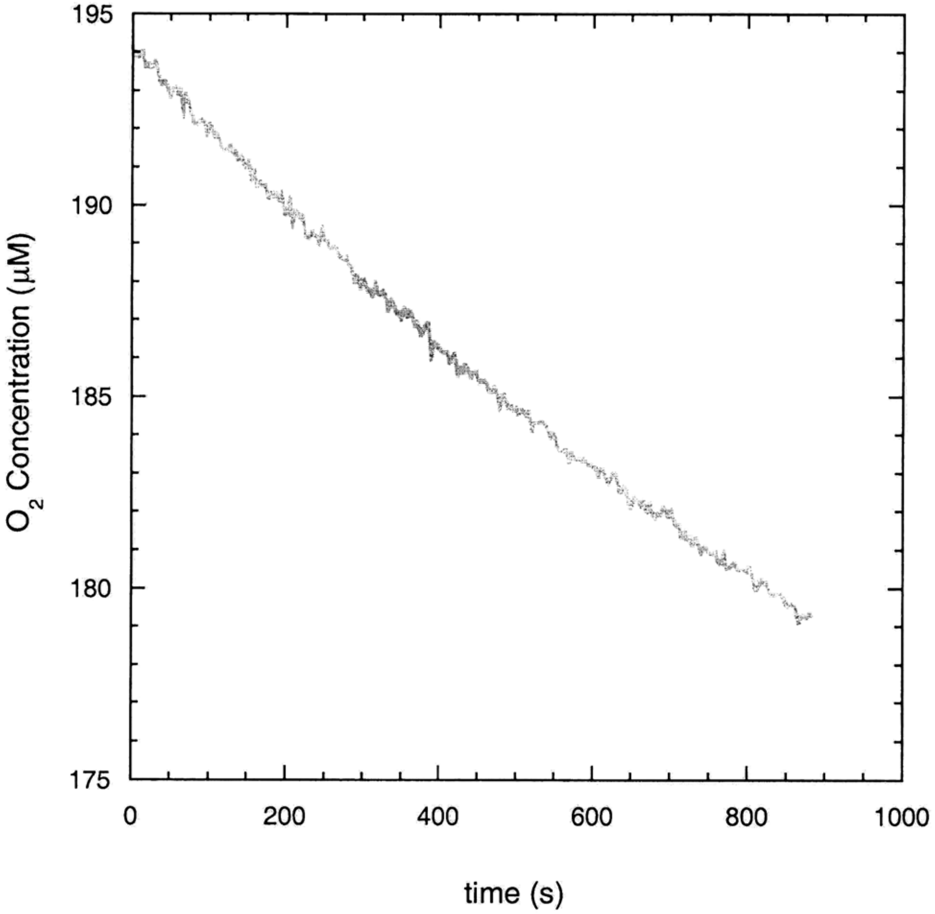

Figure D.6. Time dependence of O_2 concentrations for 4 $\times 10^6$ unactivated primary bone marrow-derived macrophages (Experiment 4).

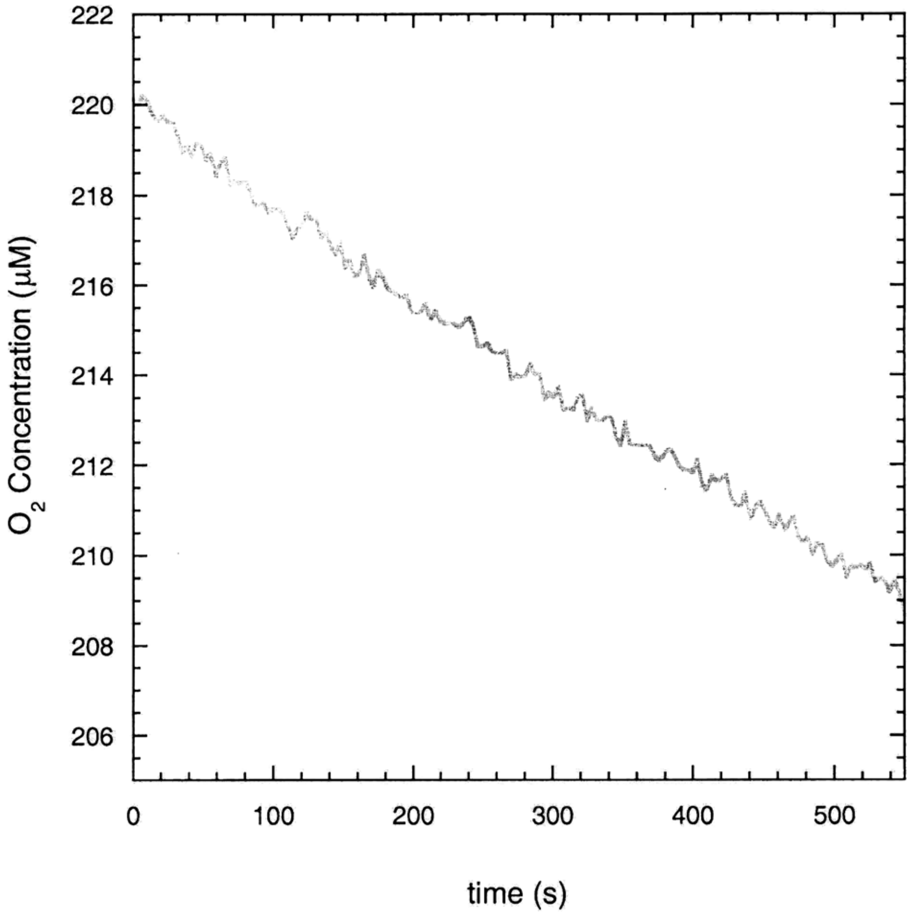

Figure D.7. Time dependence of O_2 concentrations for 4 $\times 10^6$ unactivated HCT116 colonic epithelial cells (Experiment 2).

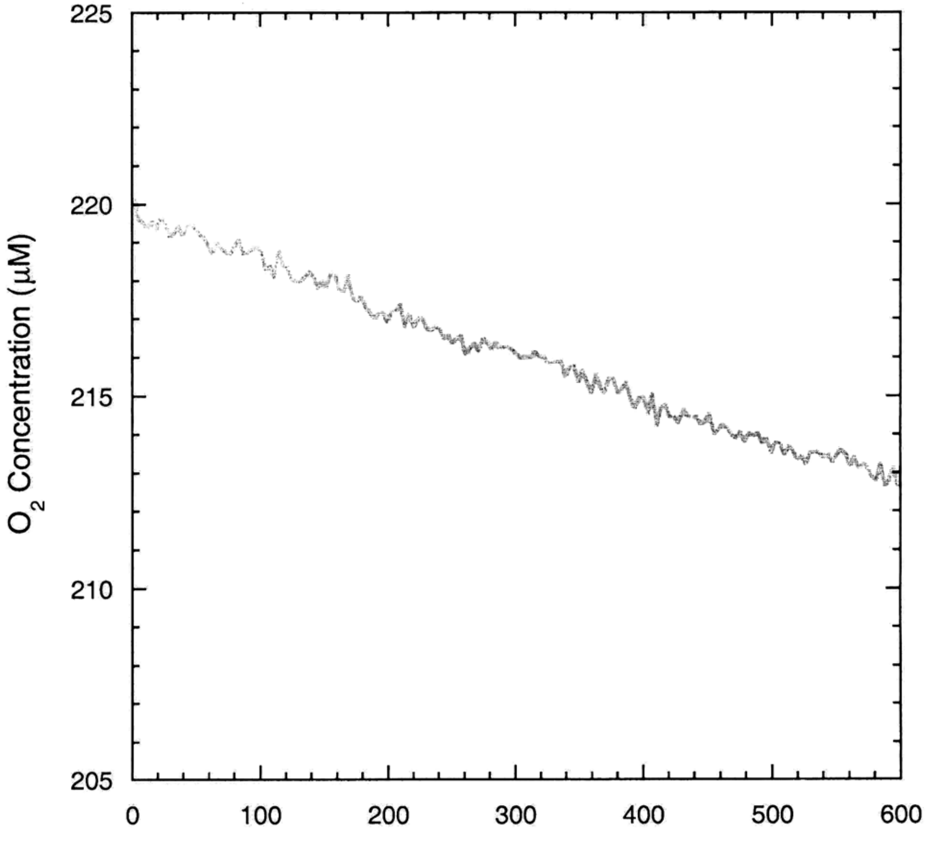

Figure D.8. Time dependence of O_2 concentrations for 6 × 10^6 unactivated HCT116 colonic epithelial cells (Experiment 3).

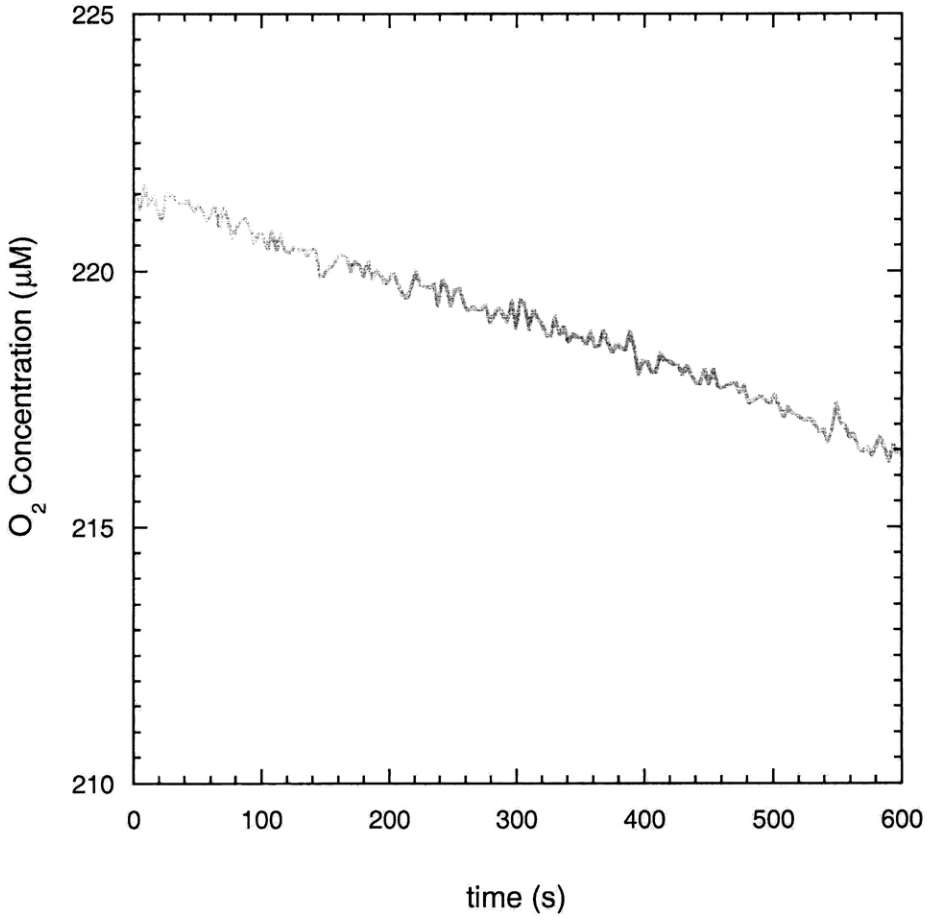

Figure D.9. Time dependence of O_2 concentrations for 4 $\times 10^6$ unactivated HCT116 colonic epithelial cells (Experiment 4).

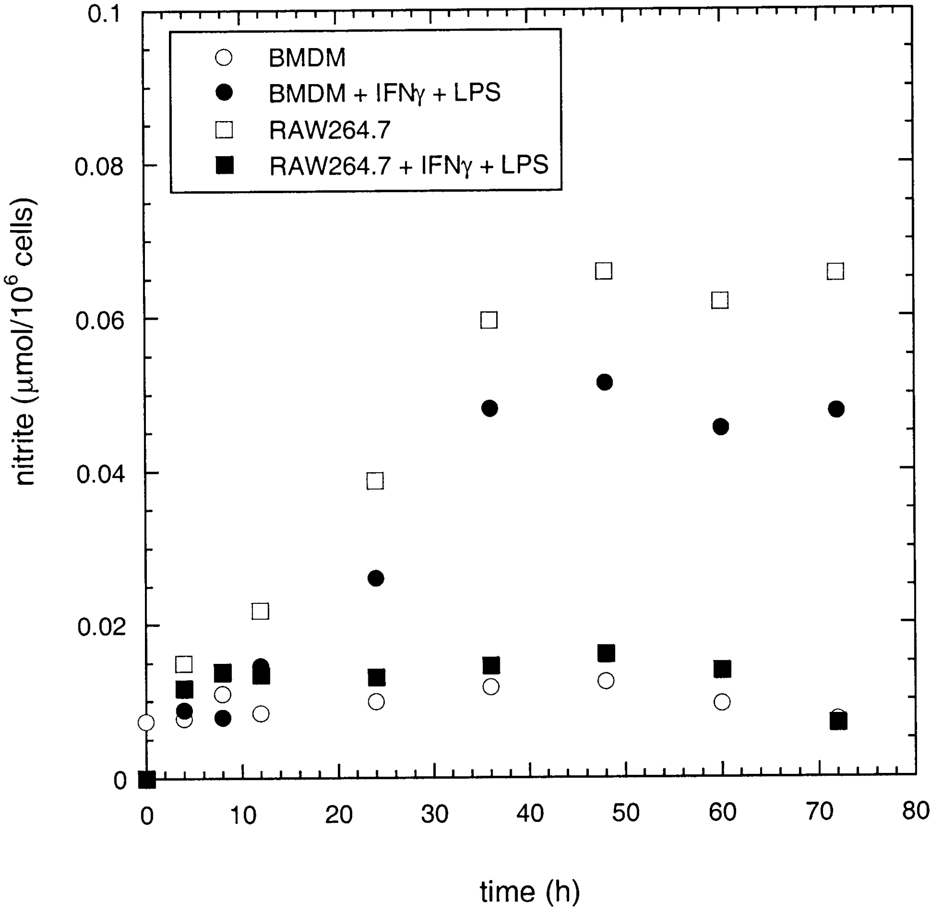

Figure D.10. Nitrite accumulation data as a function of time for unactivated RAW264.7 cells and primary BMDM and macrophages activated with IFNγ and LPS (Experiment 1).

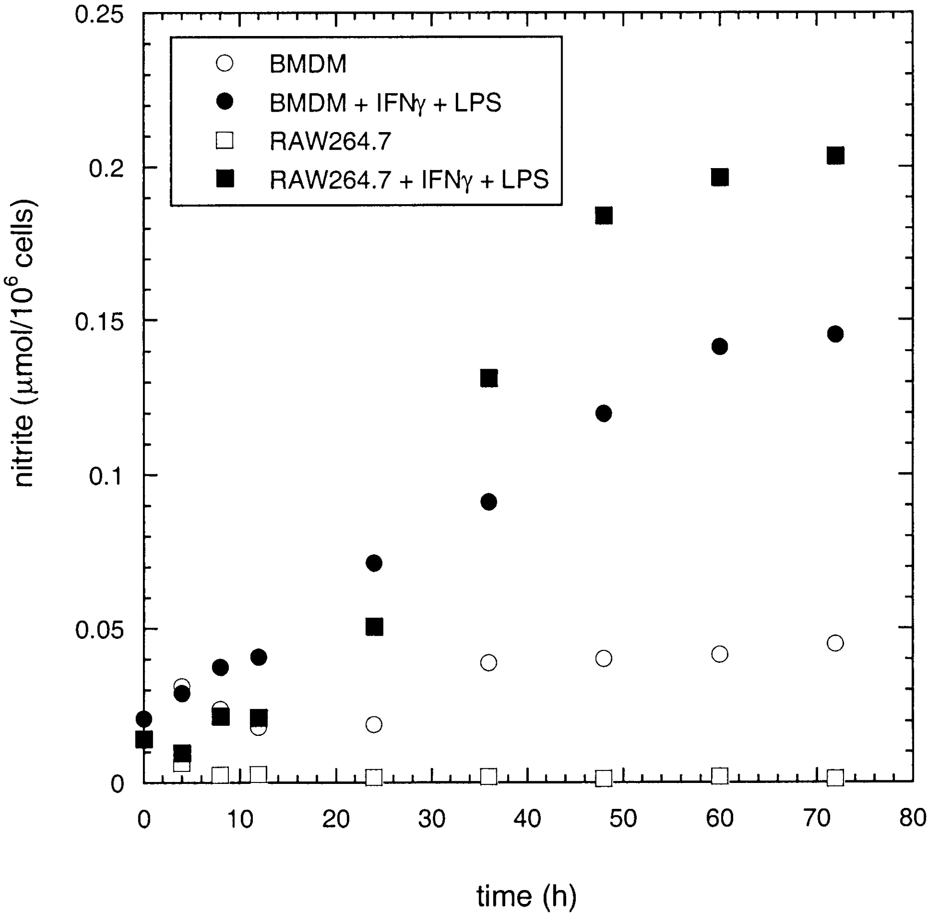

Figure D.11. Nitrite accumulation data as a function of time for unactivated RAW264.7 cells and primary BMDM and macrophages activated with IFNγ and LPS (Experiment 2).

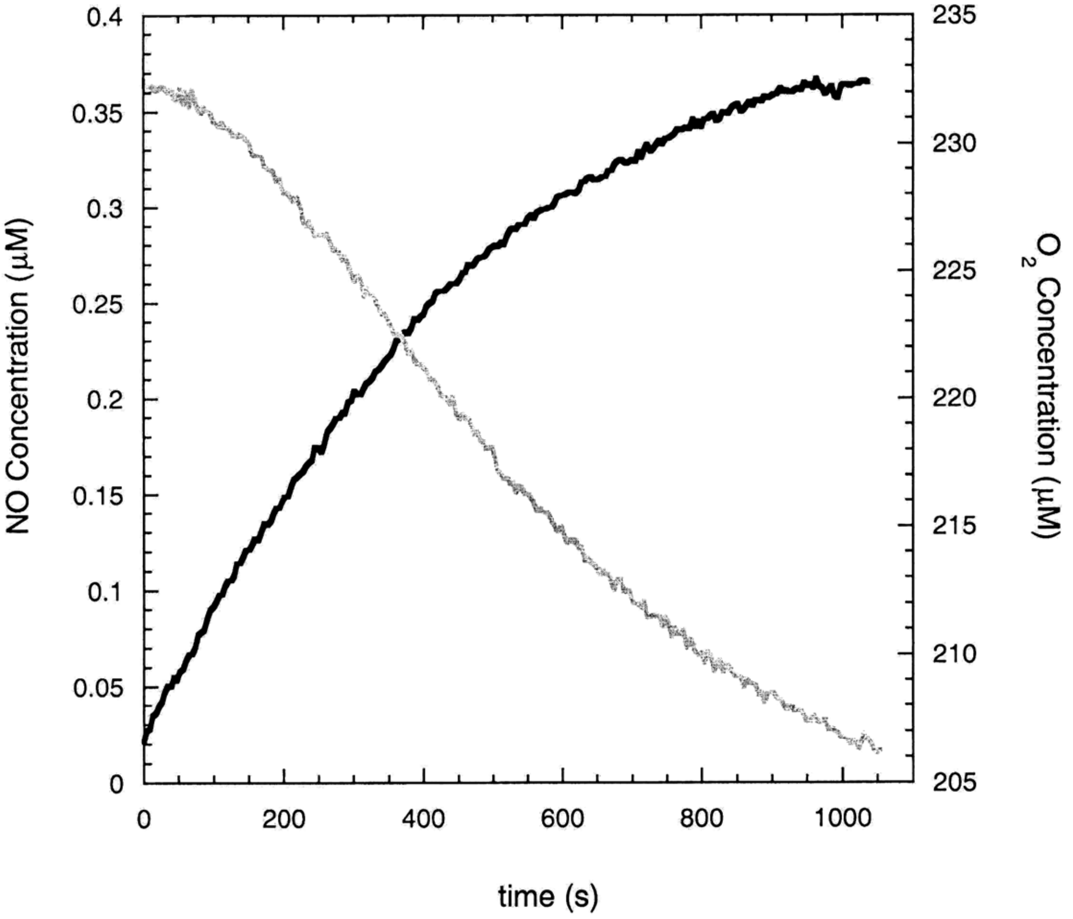

Figure D.12. Plot of NO and O_2 concentrations as a function of time for 7×10^6 primary bone marrow-derived macrophages activated with IFNγ and LPS. (Experiment 2)

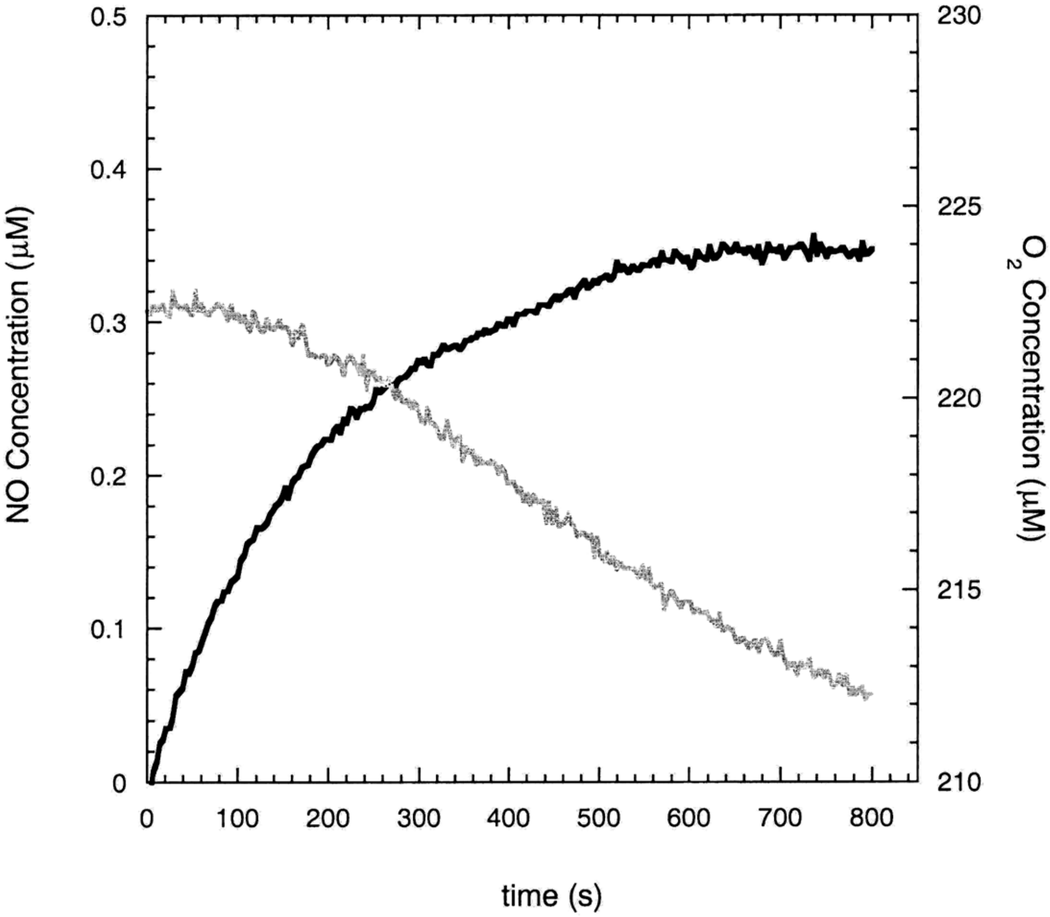

Figure D.13. Plot of NO and O_2 concentrations as a function of time for 8×10^6 bone marrow-derived macrophages activated with IFNγ and LPS. (Experiment 3)

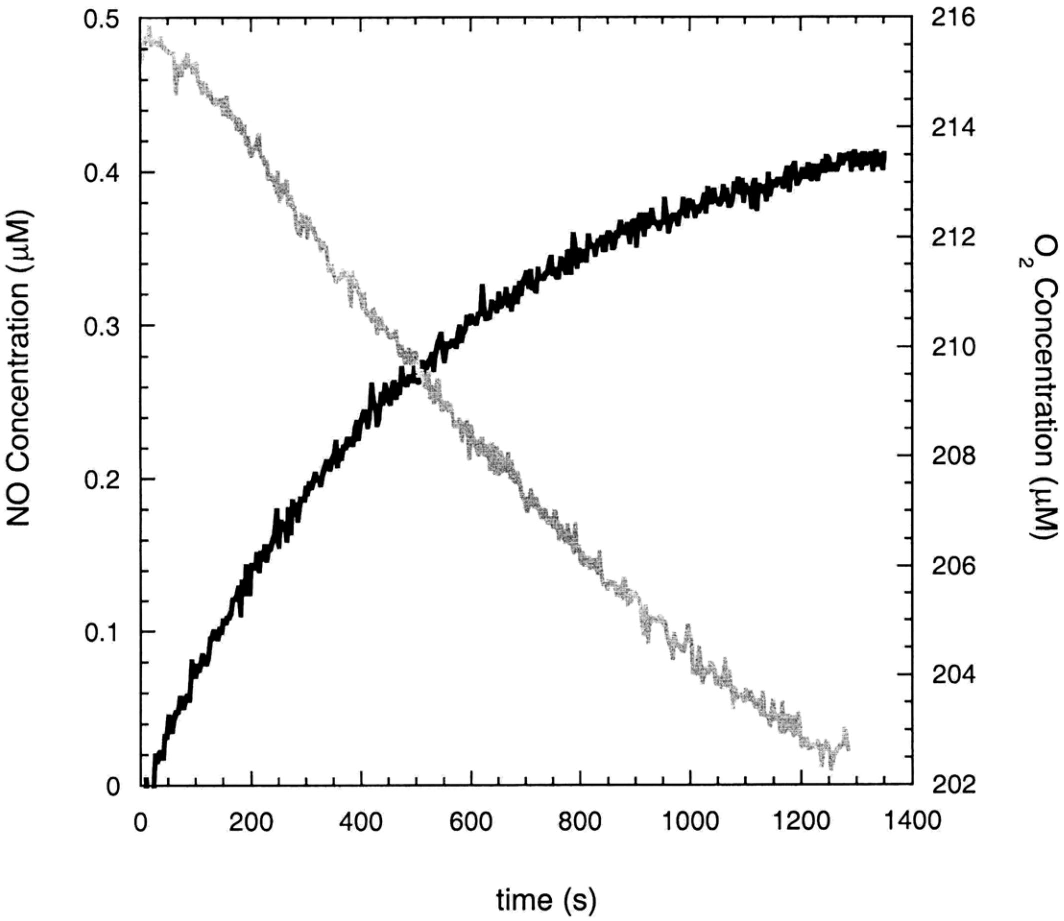

Figure D.14. Plot of NO and O_2 concentrations as a function of time for 7×10^6 bone marrow-derived macrophages activated with IFNγ and LPS. (Experiment 4)

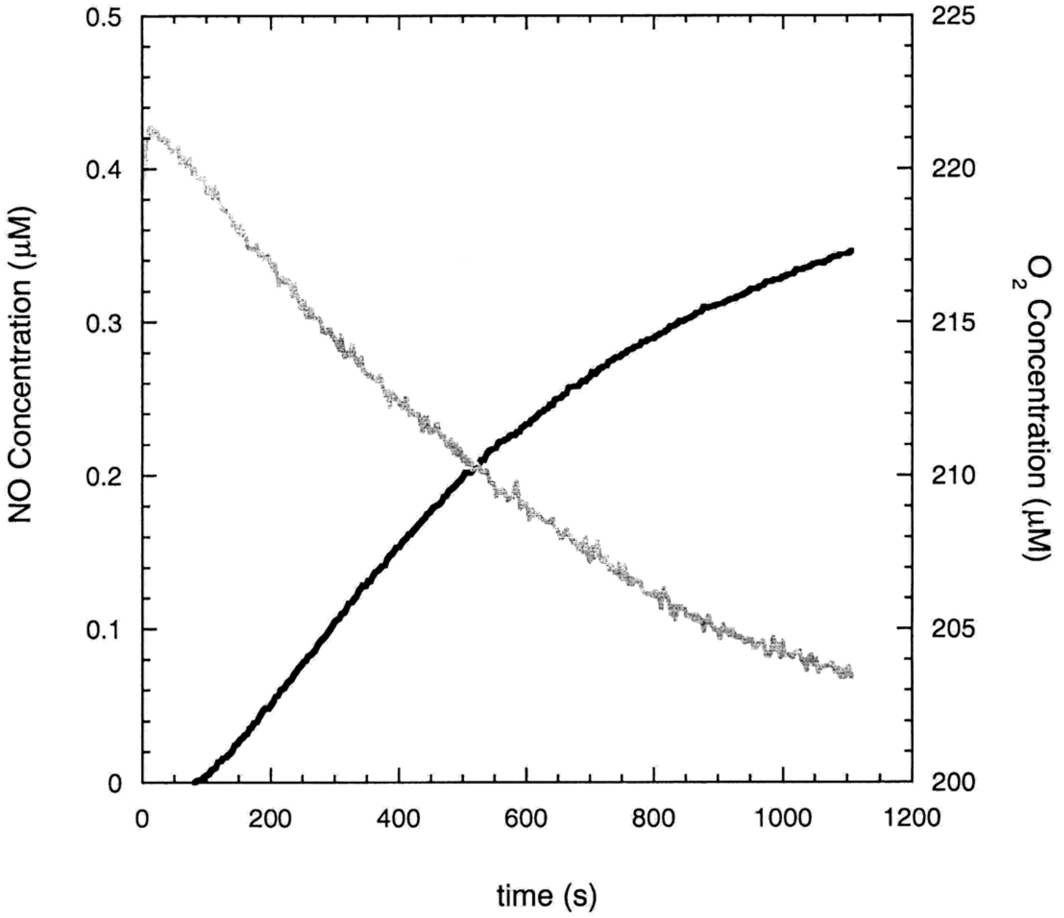

Figure D.15. Plot of NO and O_2 concentrations as a function of time for 5×10^6 bone marrow-derived macrophages activated with IFNγ and LPS. (Experiment 5)

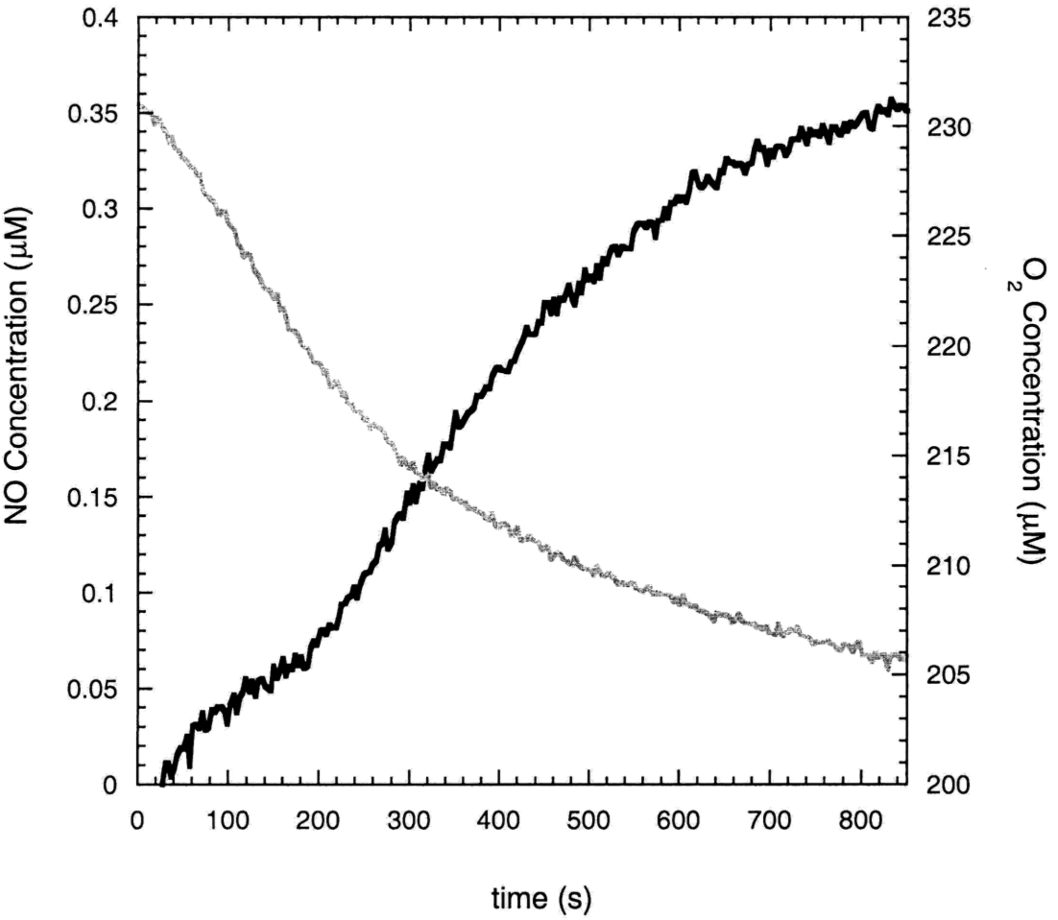

Figure D.16. Plot of NO and O_2 concentrations as a function of time for 6×10^6 bone marrow-derived macrophages activated with IFNγ and LPS. (Experiment 6)

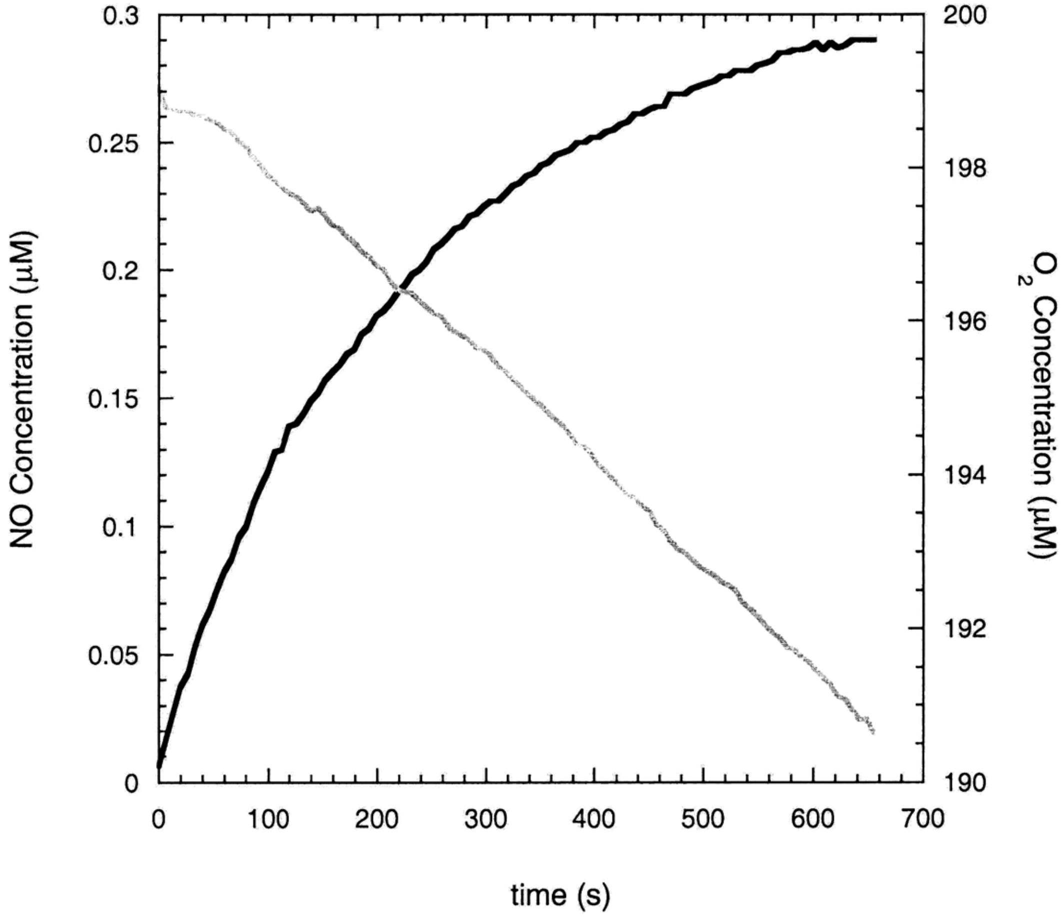

Figure D.17. Plot of NO and O_2 concentrations as a function of time for 6×10^6 RAW264.7 cells activated with IFNγ and LPS. (Experiment 2)

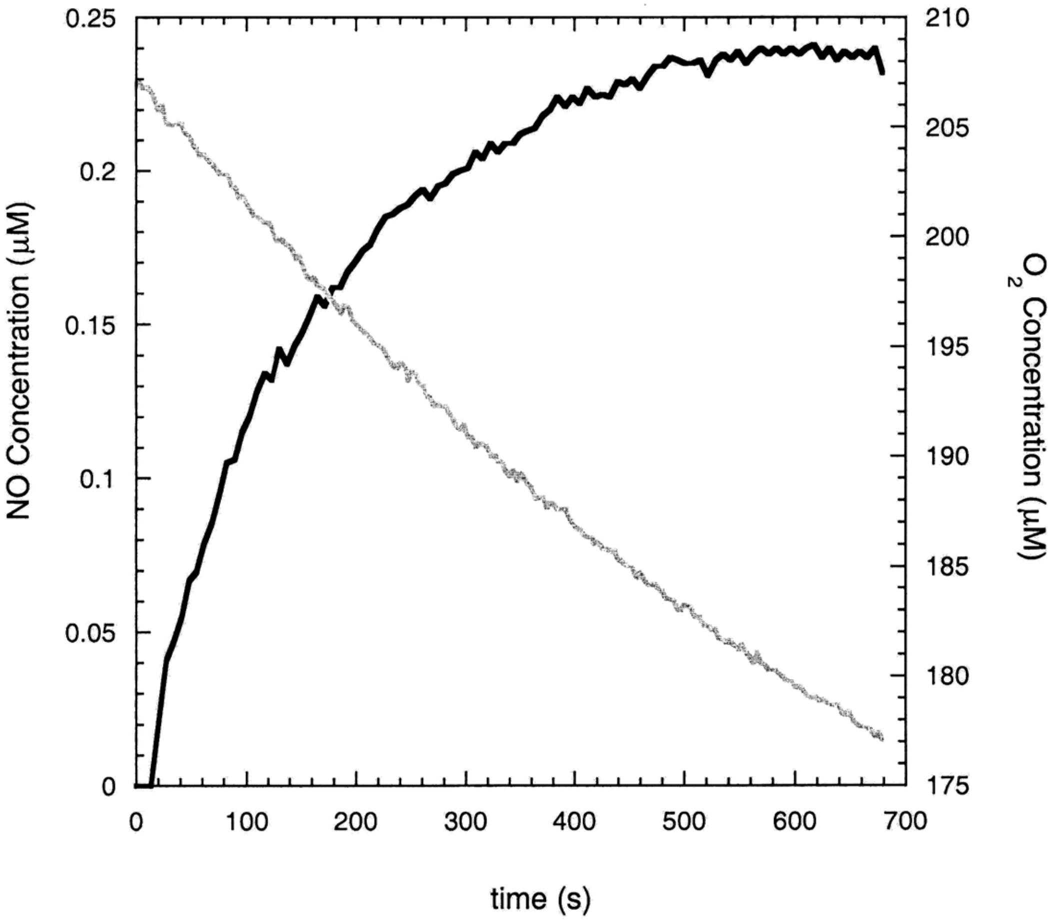

Figure D.18. Plot of NO and O_2 concentrations as a function of time for 8×10^6 RAW264.7 cells activated with IFNγ and LPS. (Experiment 3)

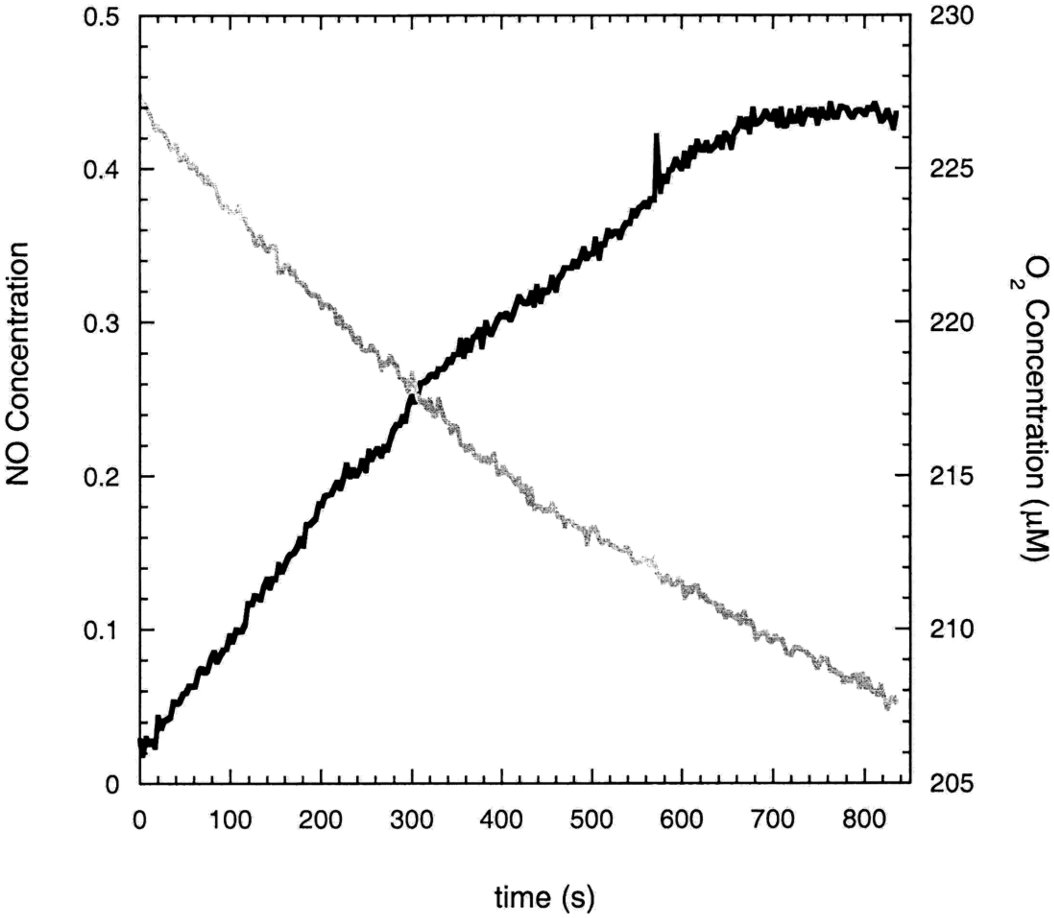

Figure D.19. Plot of NO and O_2 concentrations as a function of time for 8×10^6 RAW264.7 cells activated with IFNγ and LPS. (Experiment 4)

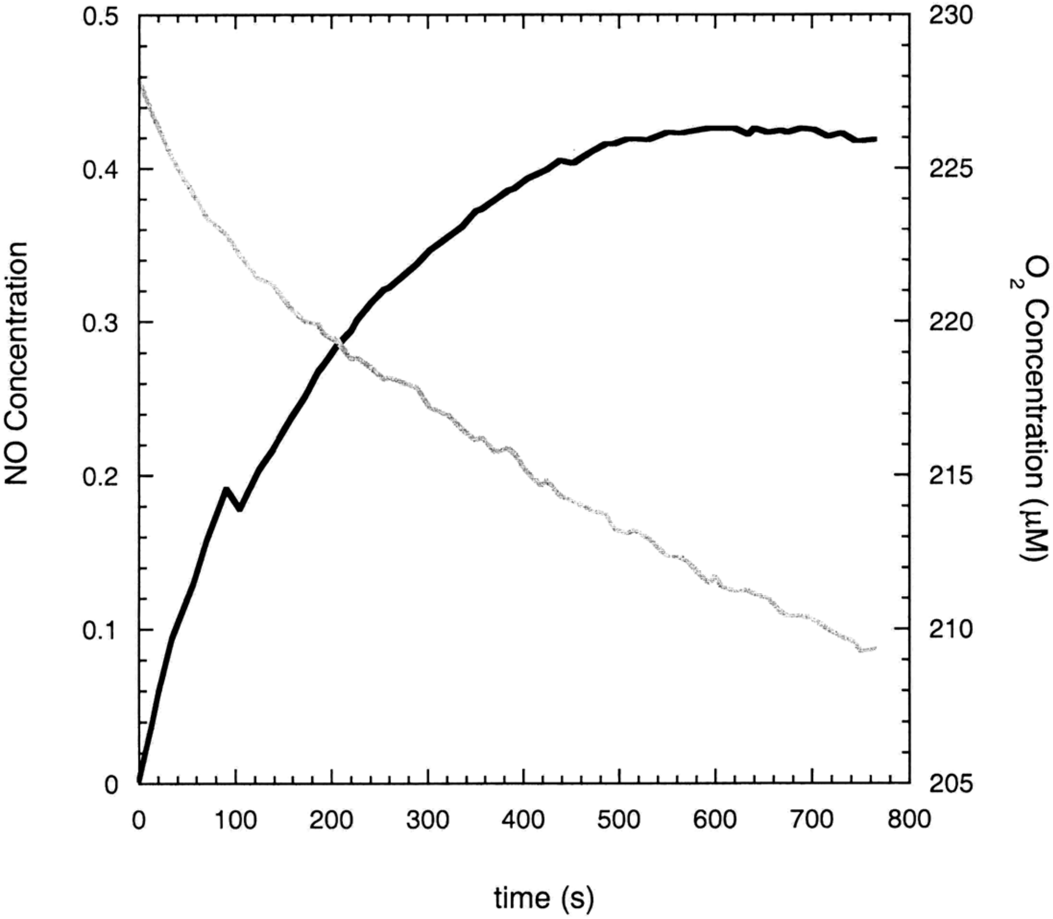

Figure D.20. Plot of NO and O_2 concentrations as a function of time for 8×10^6 RAW264.7 cells activated with IFNγ and LPS. (Experiment 5)

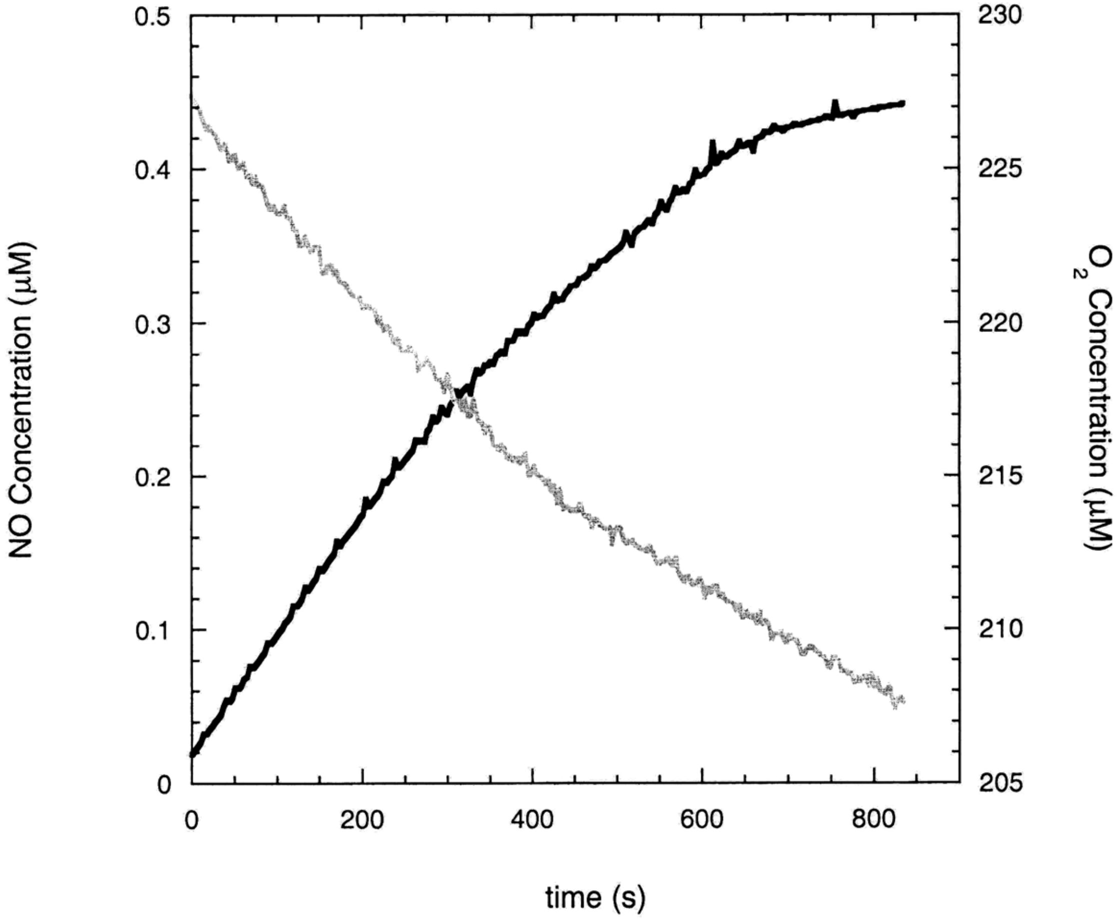

Figure D.21. Plot of NO and O_2 concentrations as a function of time for 8×10^6 RAW264.7 cells activated with IFNγ and LPS. (Experiment 6)

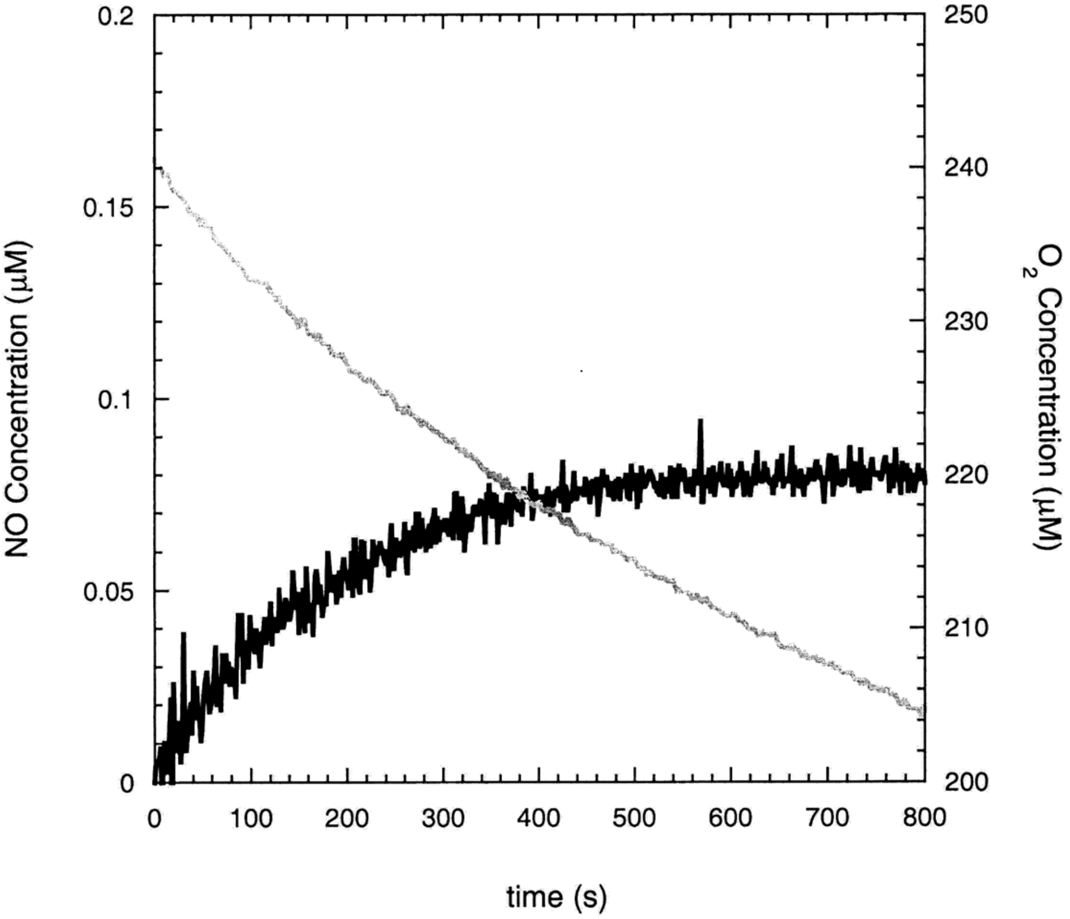

Figure D.22. Plot of NO and O_2 concentrations as a function of time for 7×10^6 HCT116 colonic epithelial cells activated with capsaicin and resveratrol. (Experiment 2)

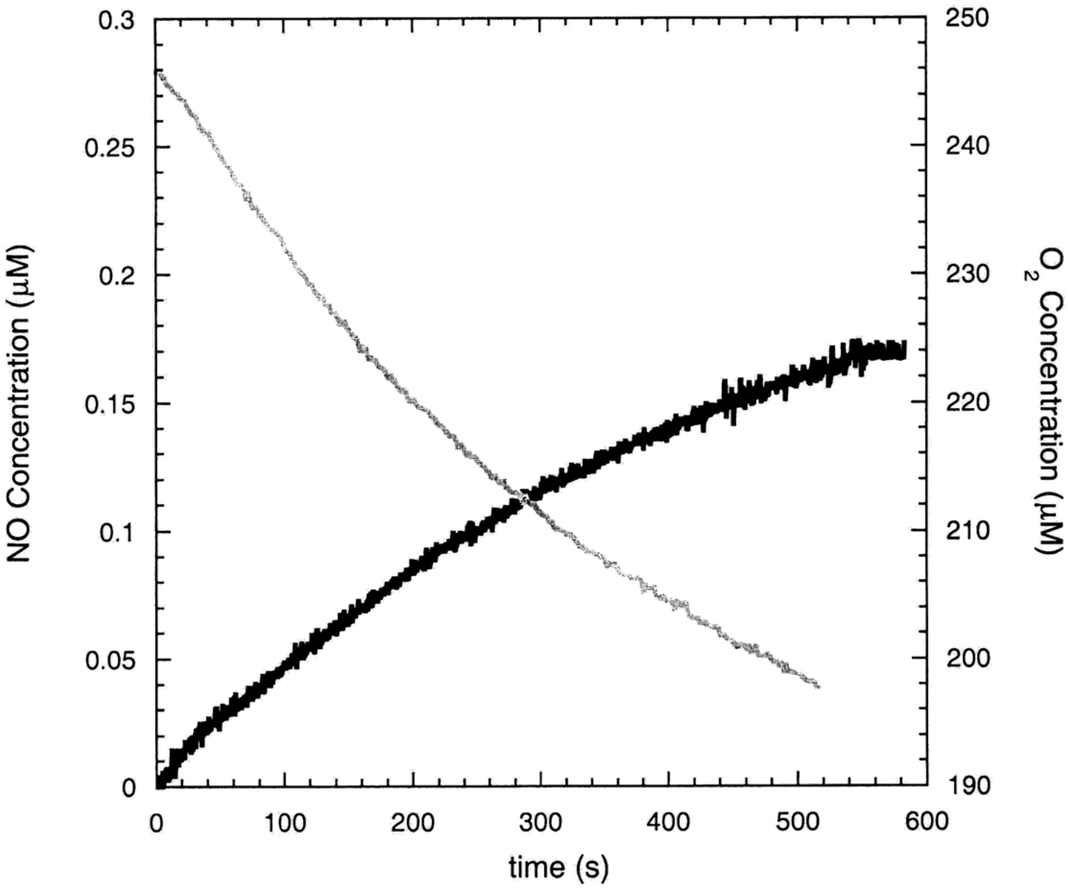

Figure D.23. Plot of NO and O_2 concentrations as a function of time for 7×10^6 HCT116 colonic epithelial cells activated with capsaicin and resveratrol. (Experiment 3)

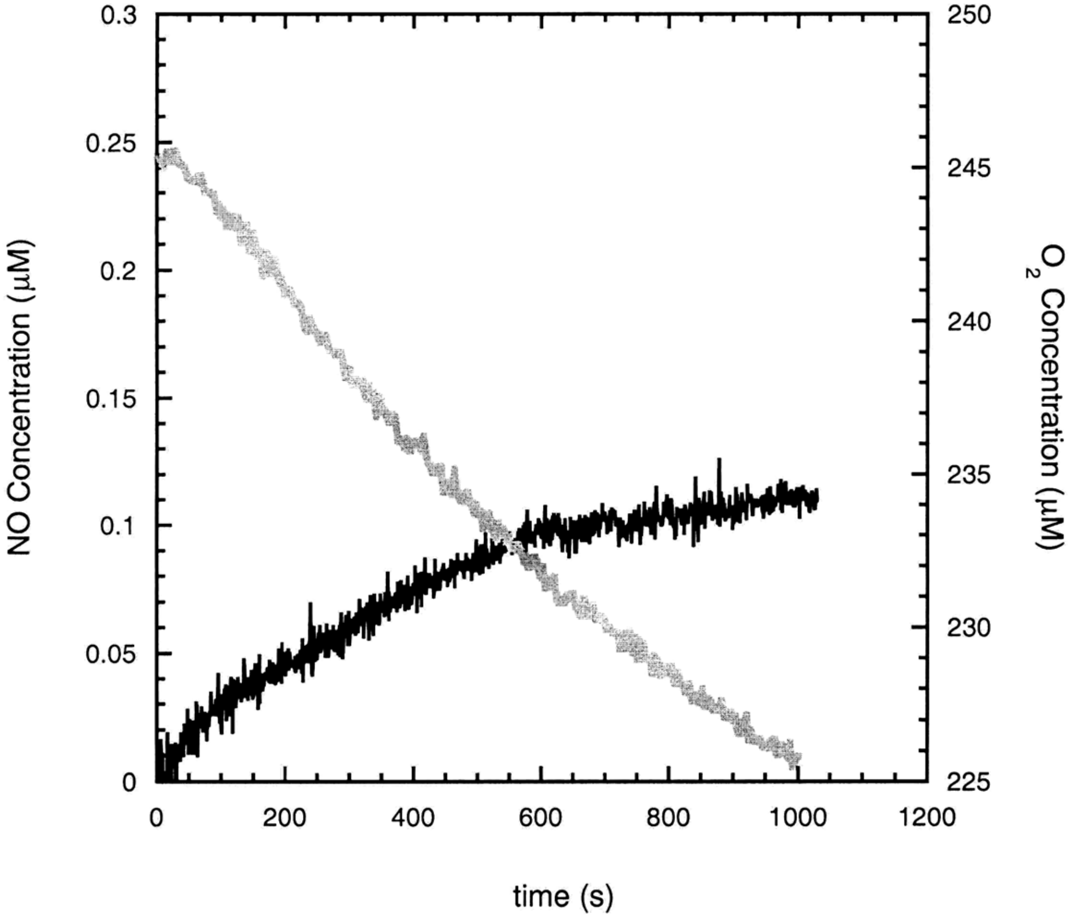

Figure D.24. Plot of NO and O_2 concentrations as a function of time for 7×10^6 HCT116 colonic epithelial cells activated with capsaicin and resveratrol. (Experiment 4)

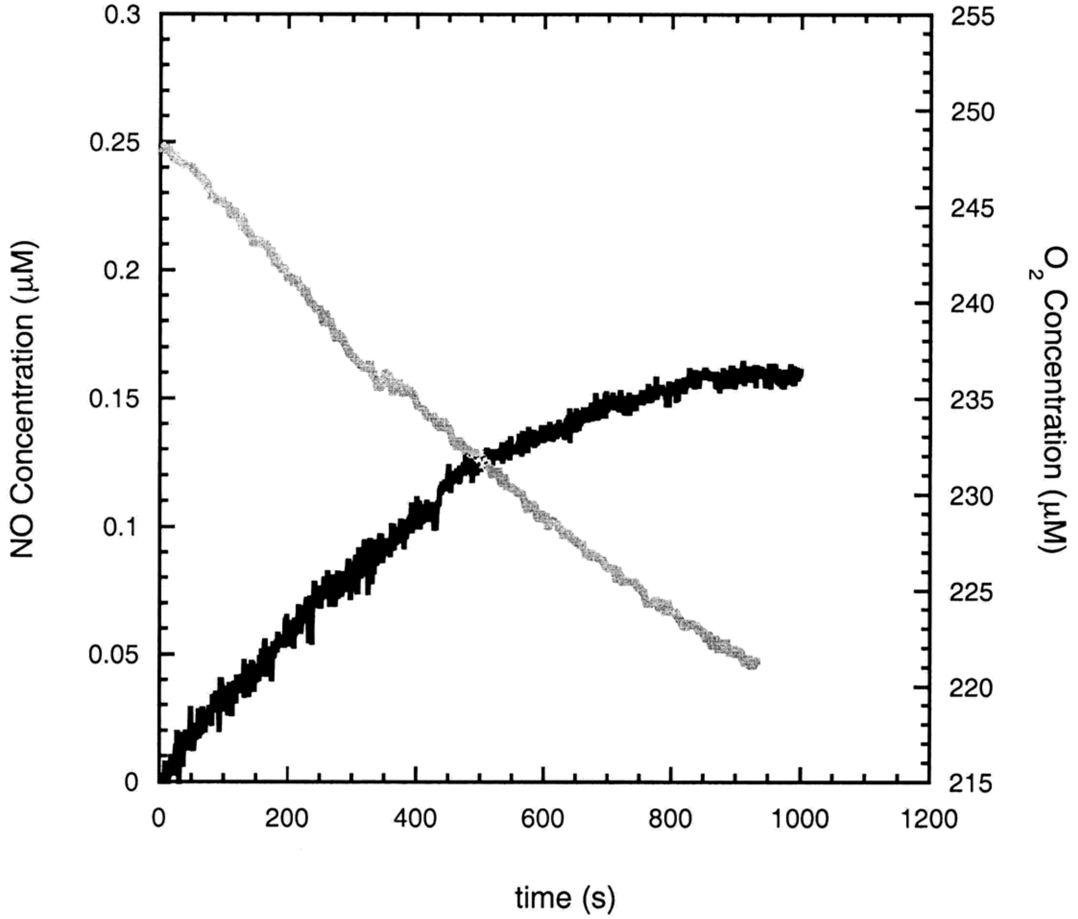

Figure D.25. Plot of NO and O_2 concentrations as a function of time for 7×10^6 HCT116 colonic epithelial cells activated with capsaicin and resveratrol. (Experiment 5)

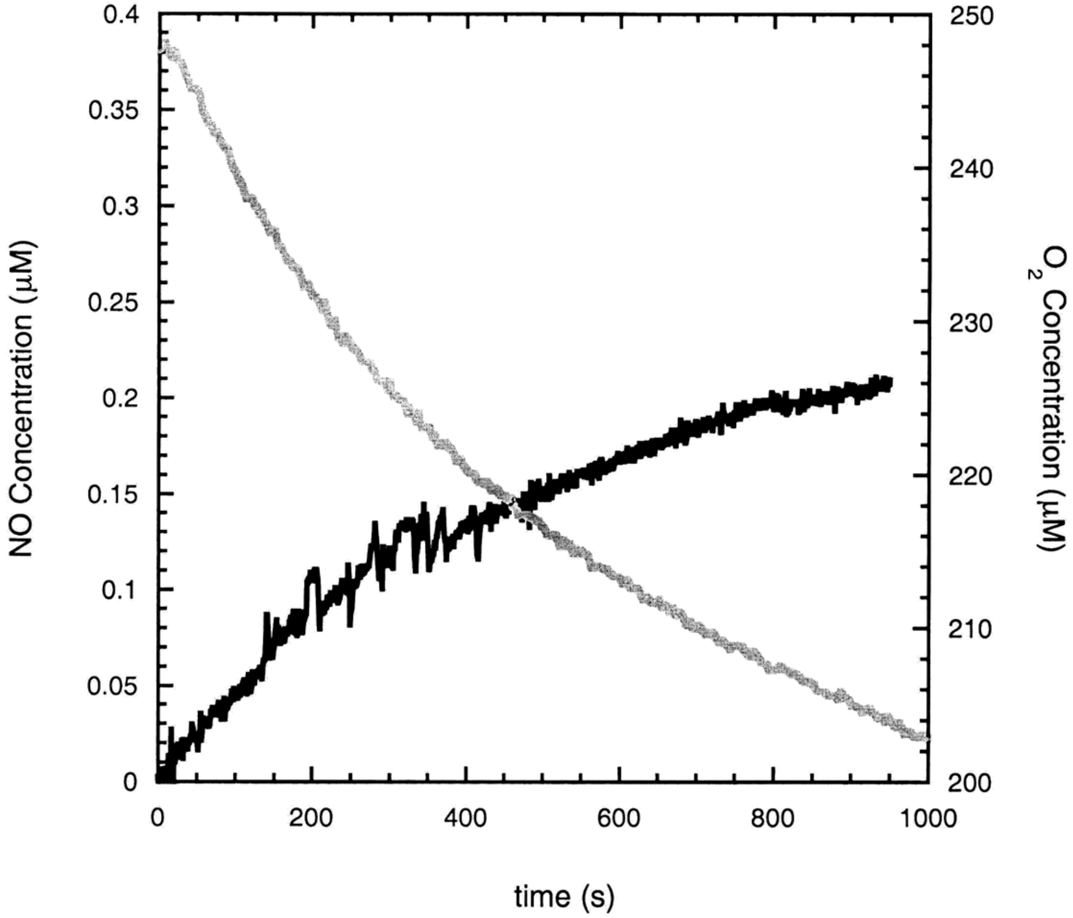

Figure D.26. Plot of NO and O_2 concentrations as a function of time for 7×10^6 HCT116 colonic epithelial cells activated with capsaicin and resveratrol. (Experiment 6)

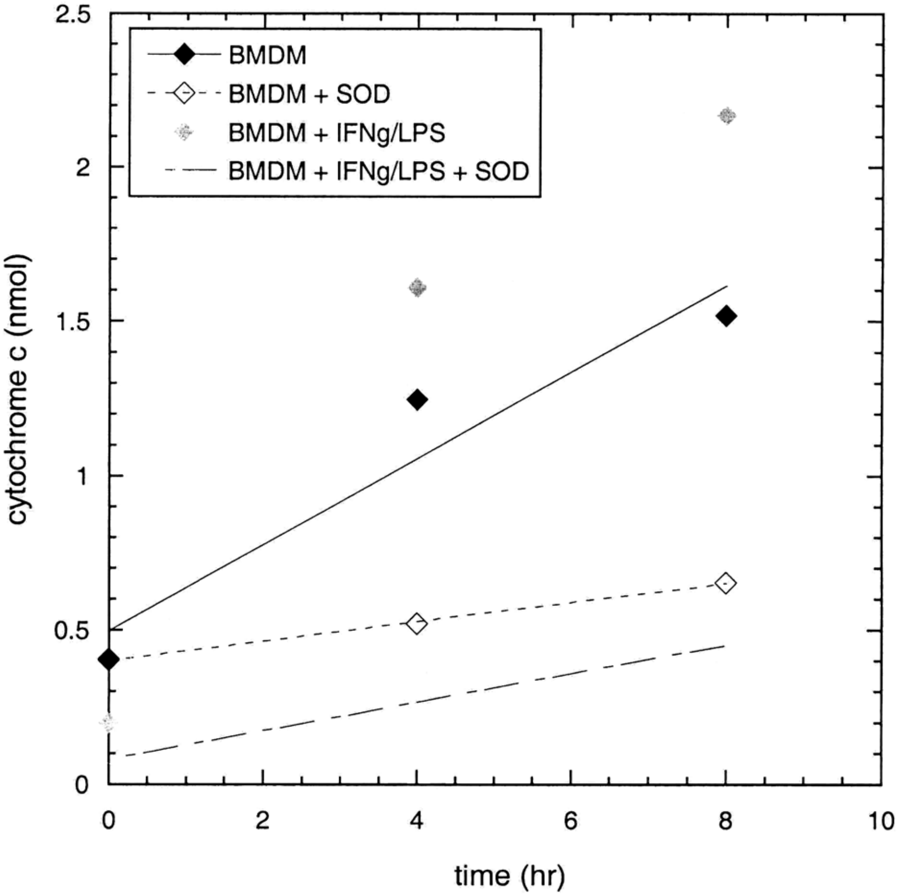

Figure D.27. Ferrocytochrome c concentrations as function of time for 5×10^5 primary bone marrow-derived macrophages. (Experiment 2)

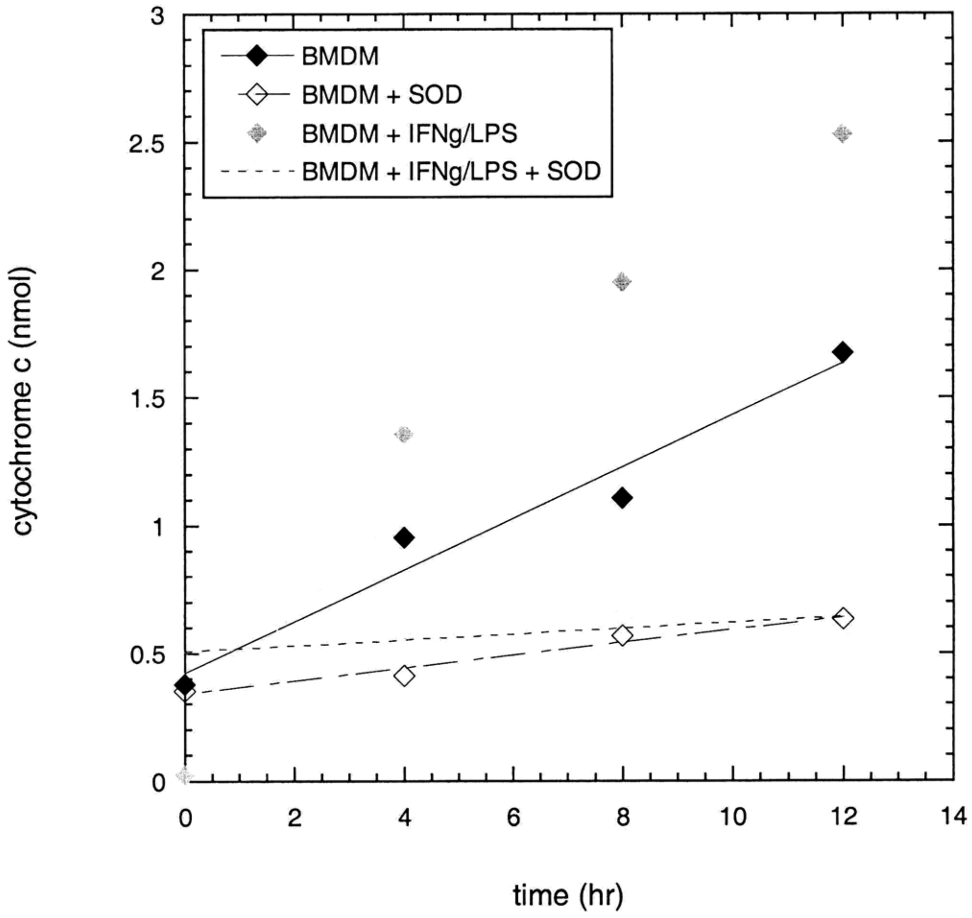

Figure D.28. Ferrocytochrome c concentrations as function of time for 5×10^5 primary bone marrow-derived macrophages. (Experiment 3)

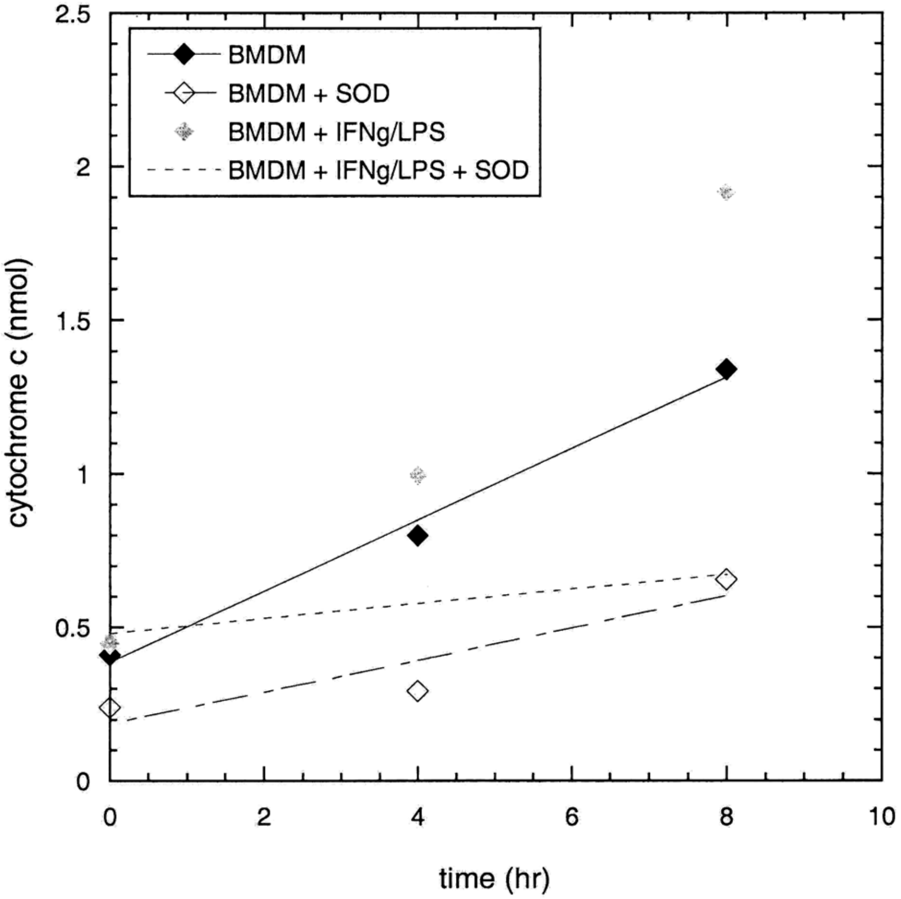

Figure D.29. Ferrocytochrome c concentrations as function of time for 5×10^5 primary bone marrow-derived macrophages. (Experiment 4)

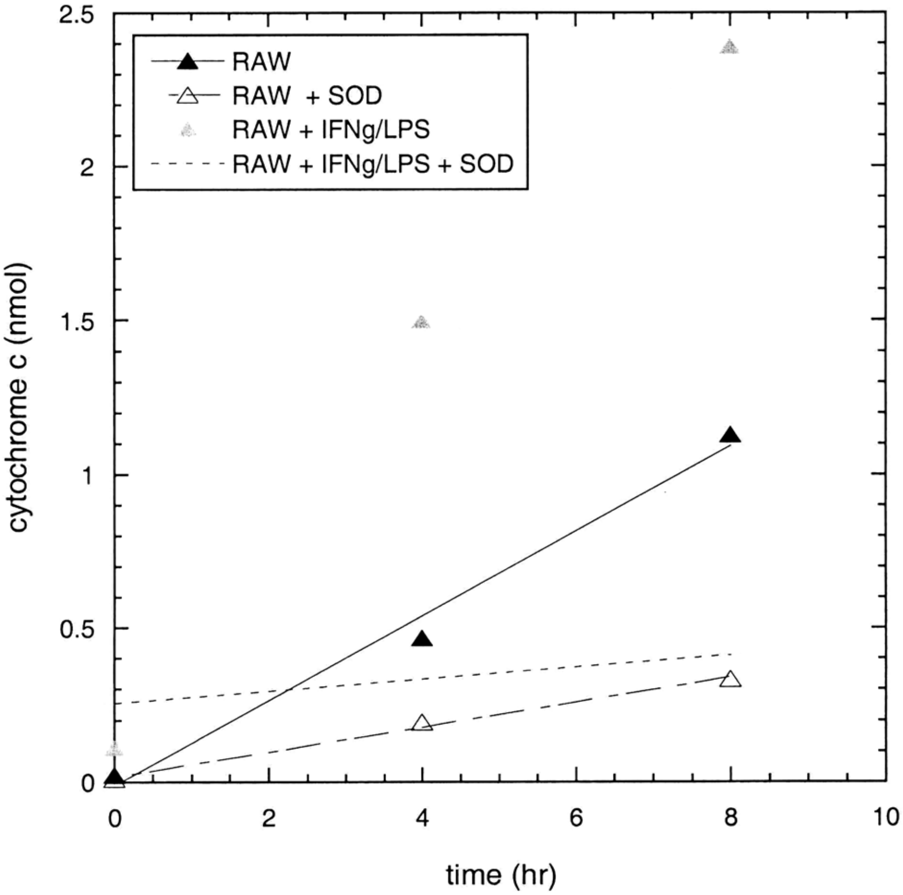

Figure D.30. Ferrocytochrome c concentrations as function of time for 5×10^5 RAW 264.7 cells. (Experiment 2)

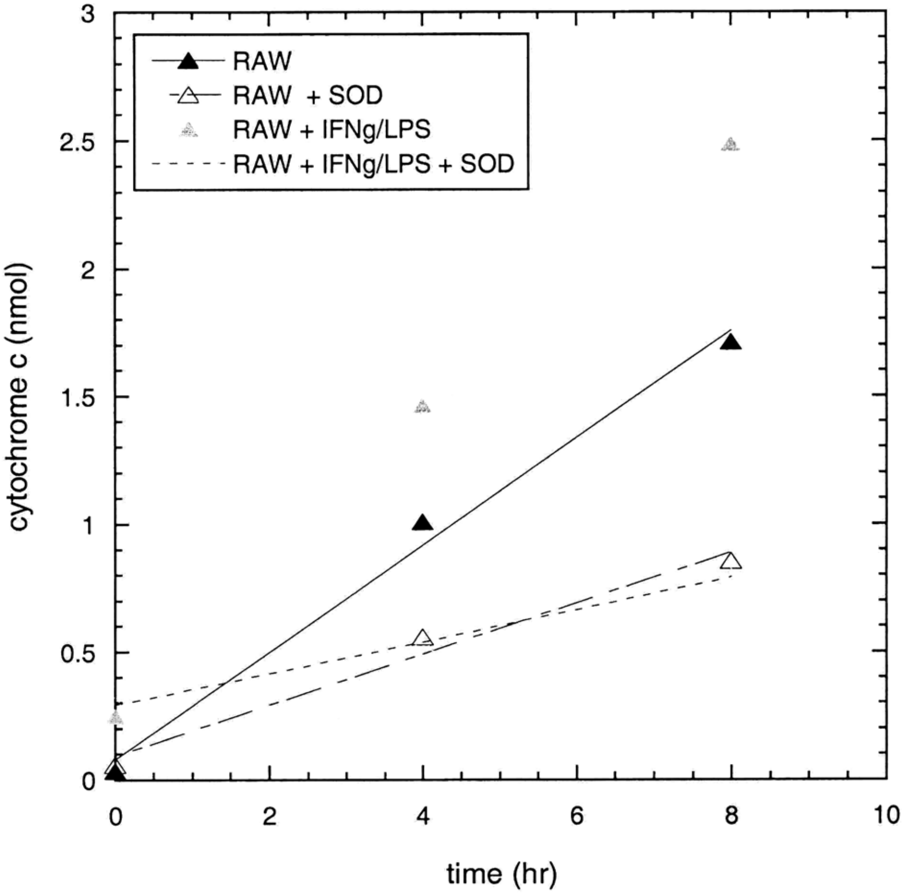

Figure D.31. Ferrocytochrome c concentrations as function of time for 5×10^5 RAW 264.7 cells. (Experiment 3)

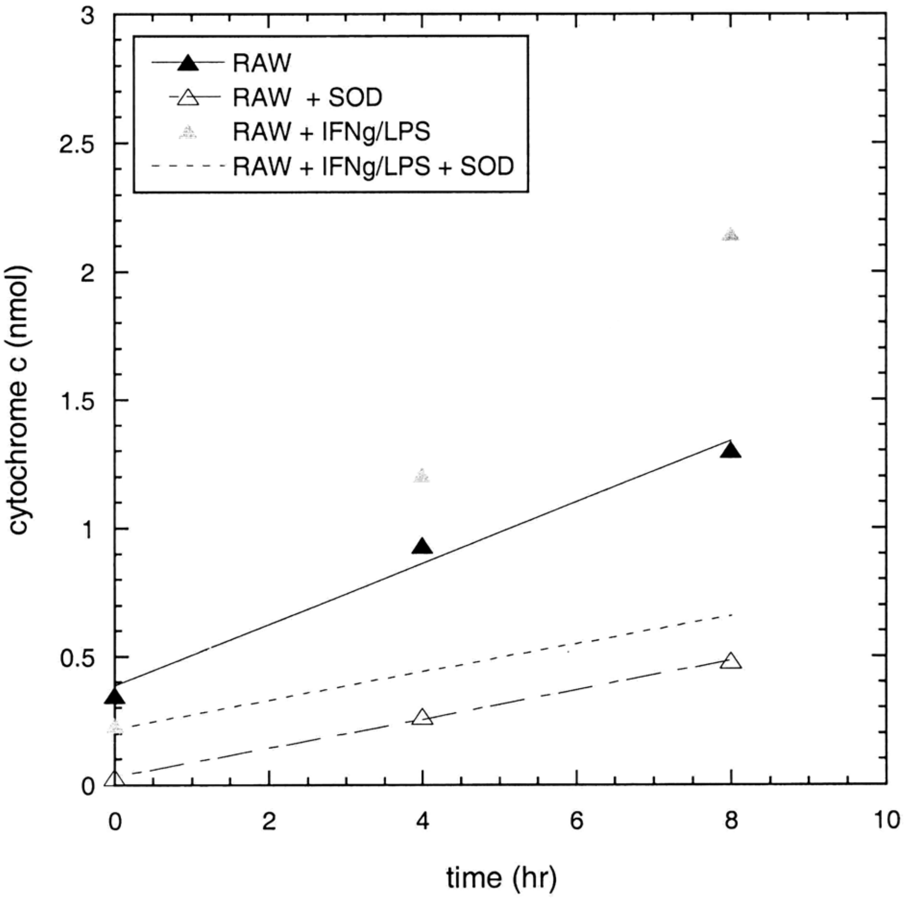

Figure D.32. Ferrocytochrome c concentrations as function of time for 5×10^5 RAW 264.7 cells. (Experiment 4)

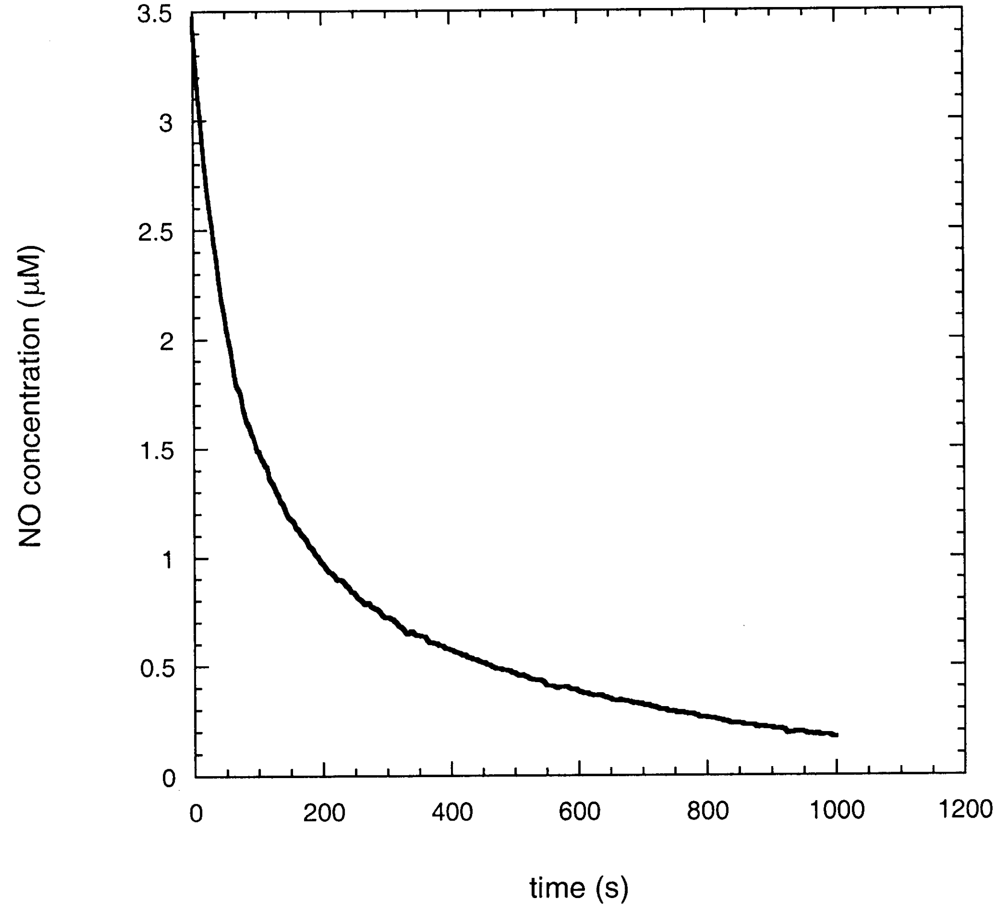

Figure D.33. Plots of NO concentrations as a function of time for cell culture media (DMEM and HEPES in the dark at 37 °C) following an injection of saturated NO solutions. (Experiment2)

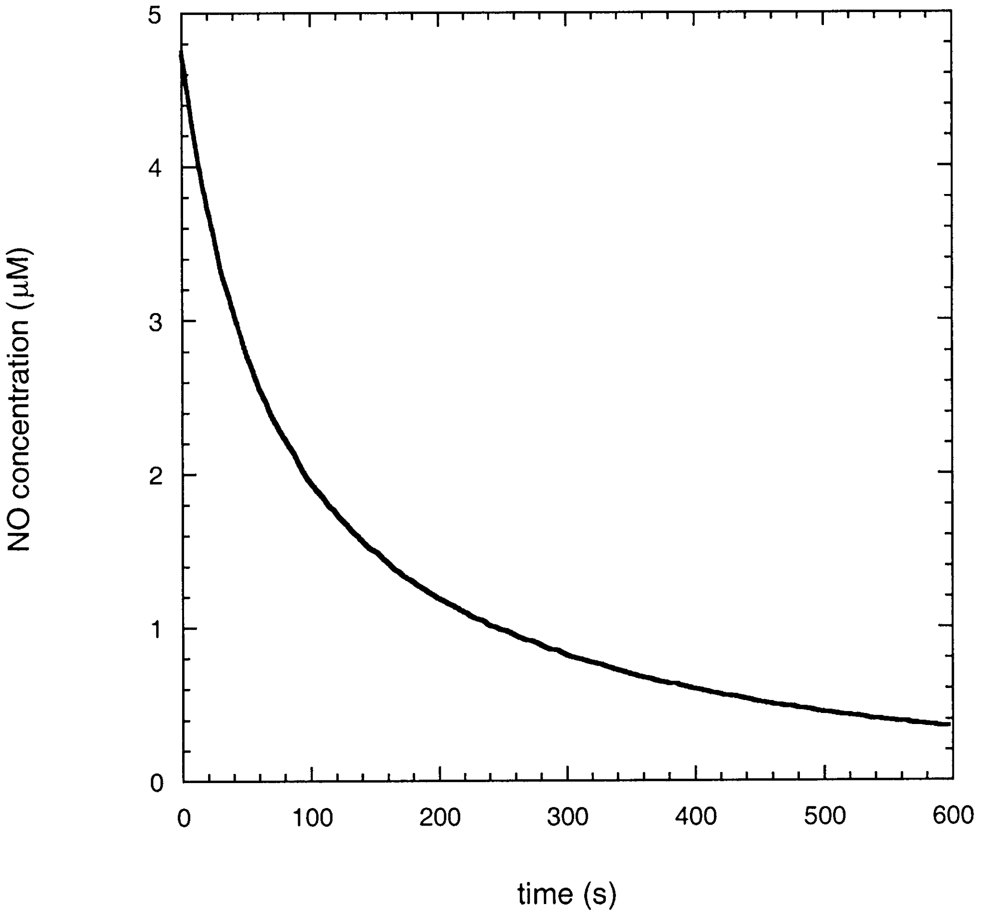

Figure D.34. Plots of NO concentrations as a function of time for cell culture media (DMEM and HEPES in the dark at 37 °C) following an injection of saturated NO solutions. (Experiment 3)

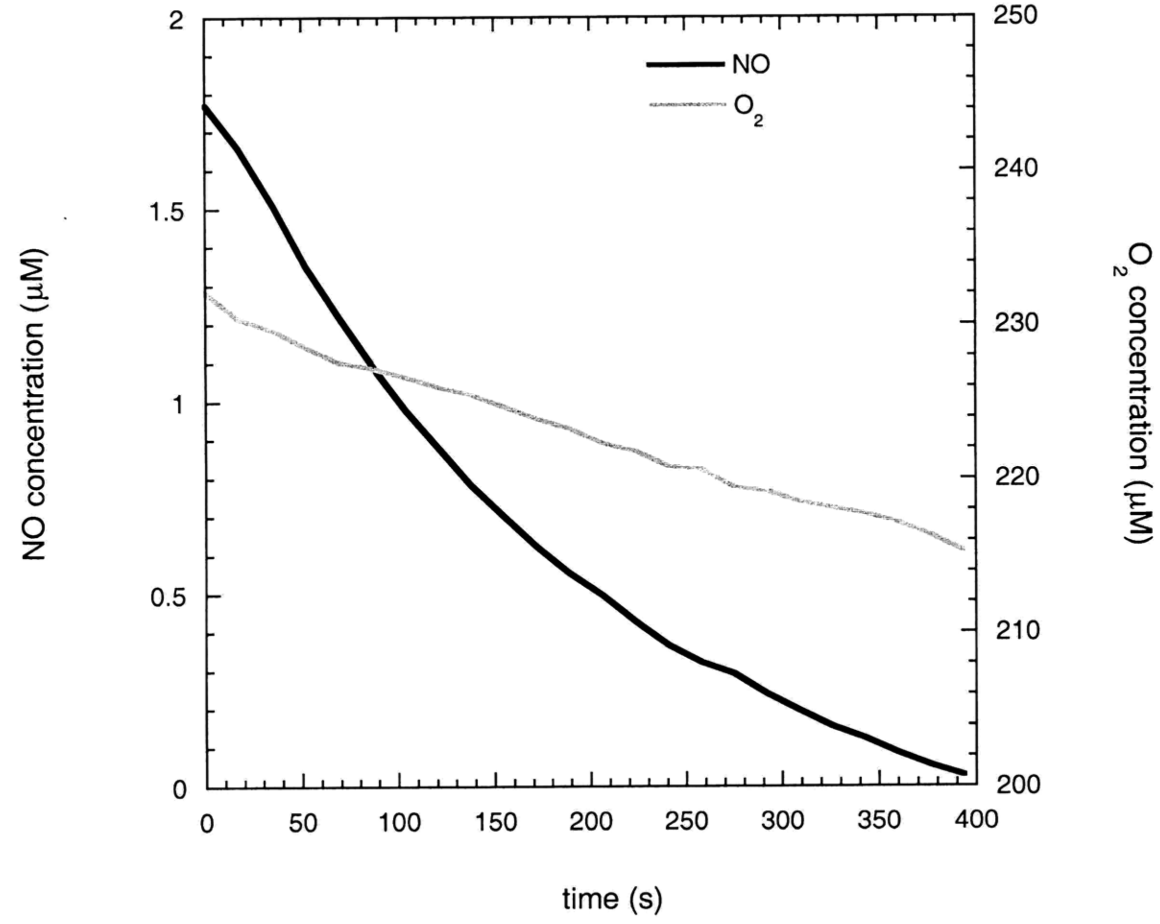

Figure D.35. Plots of NO and O_2 concentrations as a function of time for 5×10^6 A375 melanoma cells. (Experiment 2)

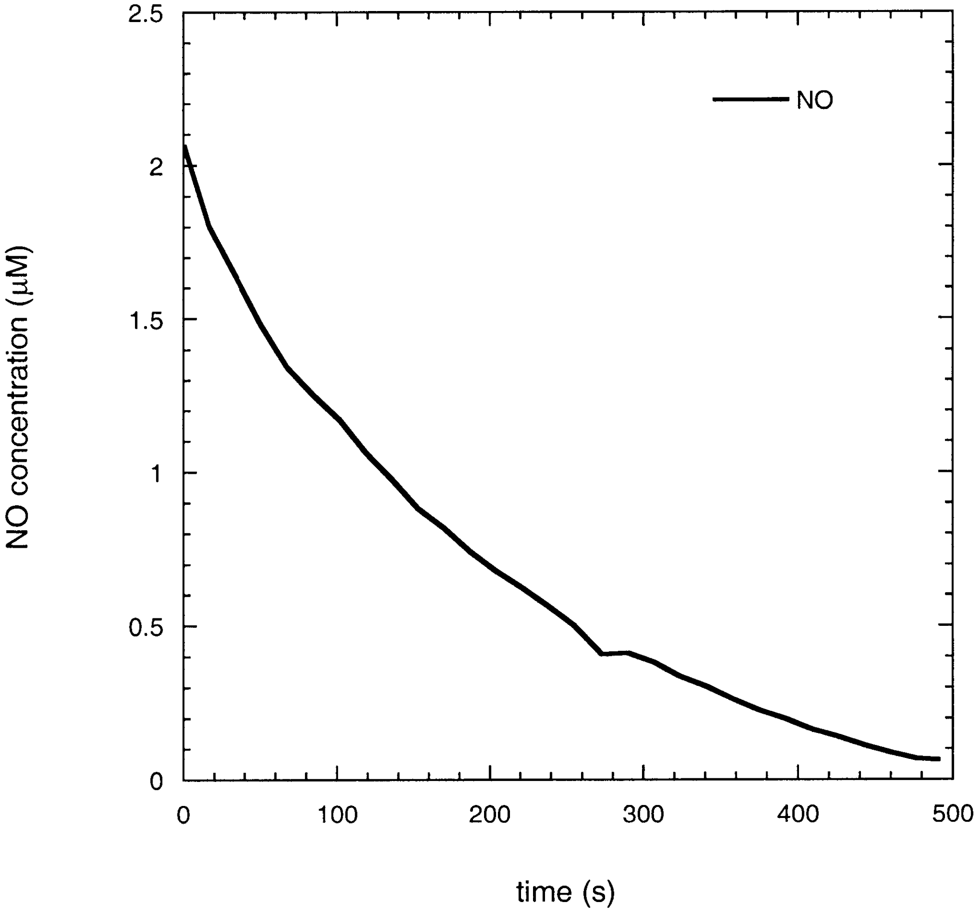

Figure D.36. Plots of NO concentrations as a function of time for 3.5×10^6 A375 melanoma cells. (Experiment 3)

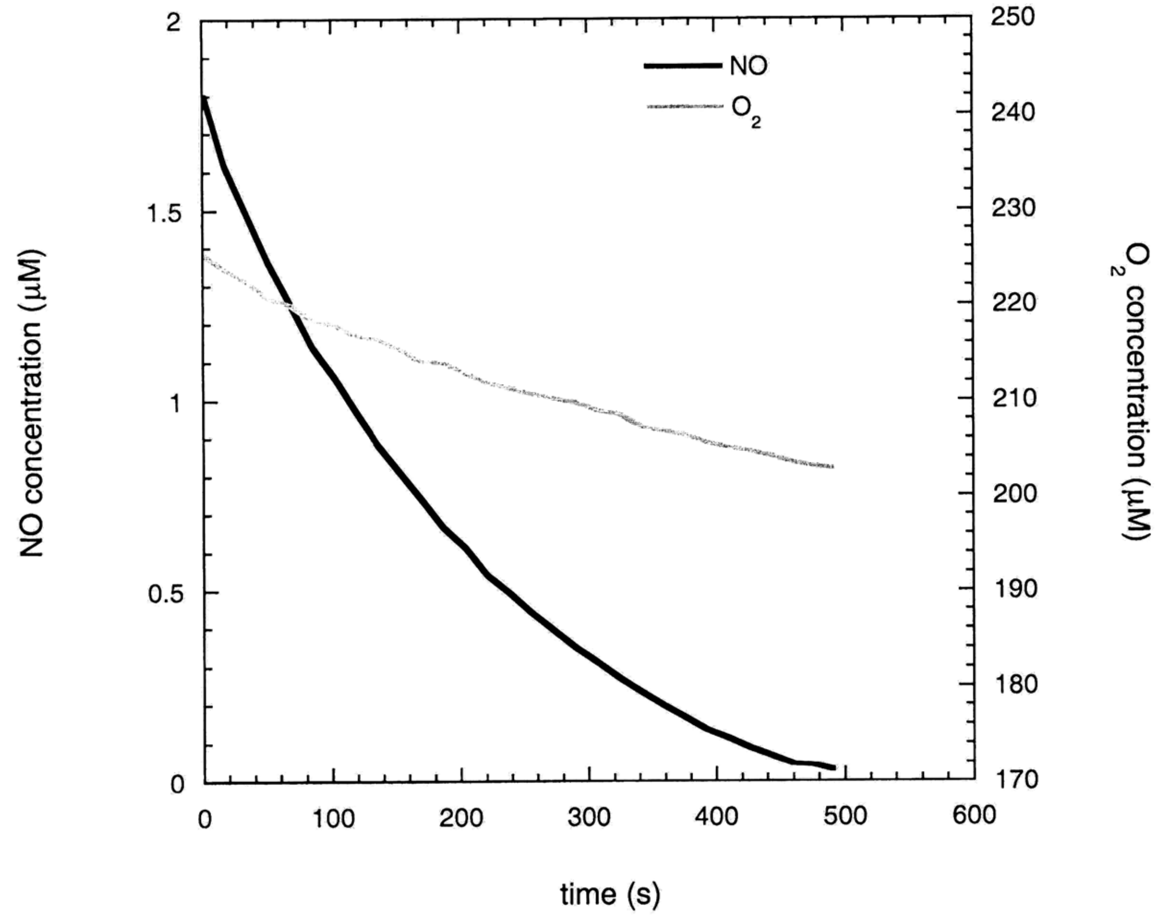

Figure D.37. Plots of NO and O_2 concentrations as a function of time for 4×10^6 A375 melanoma cells. (Experiment 4)

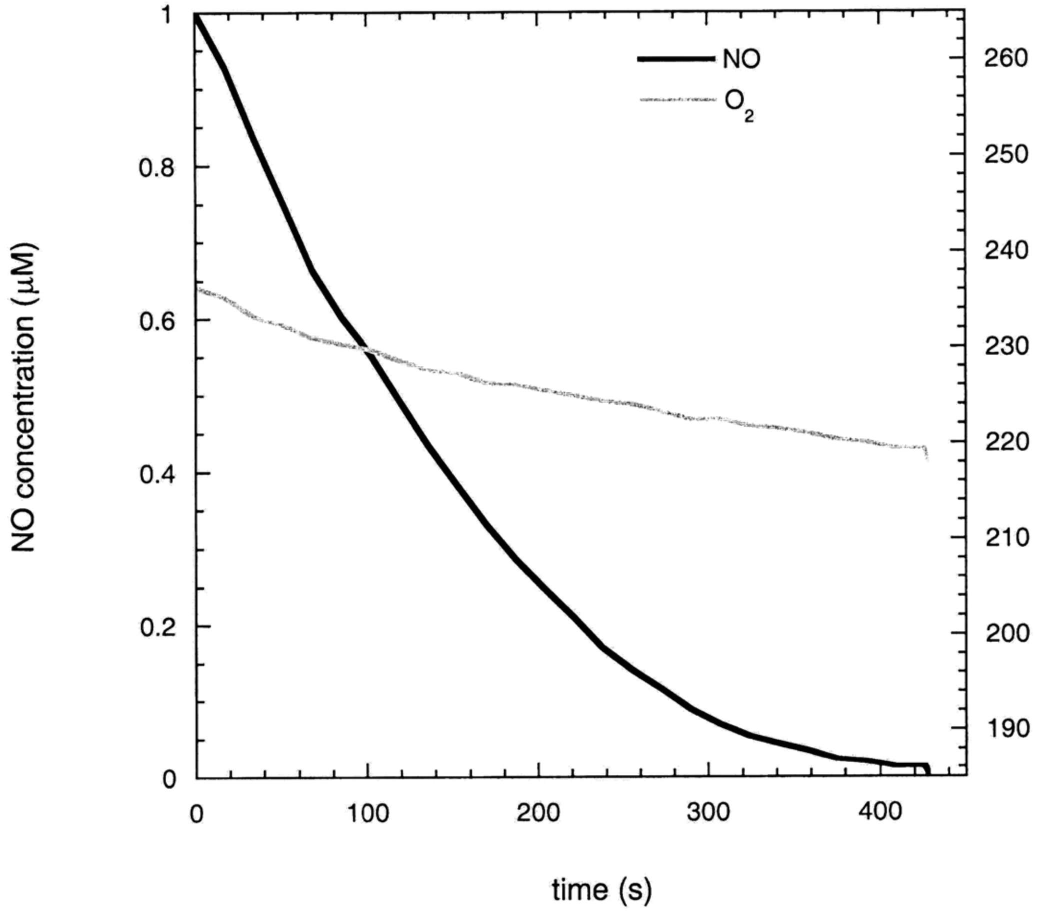

Figure D.38. Plots of NO and O_2 concentrations as a function of time for 5×10^6 A375 melanoma cells. (Experiment 5)

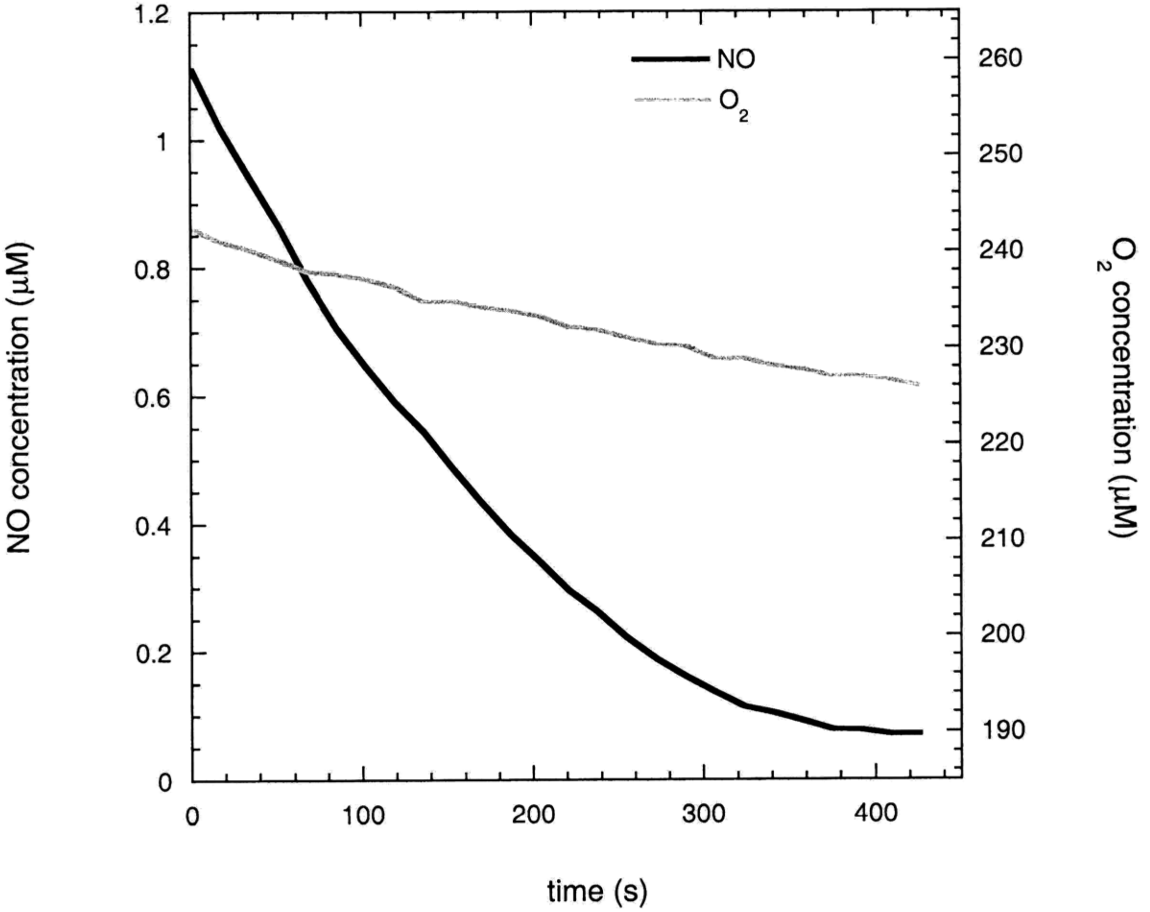

Figure D.39. Plots of NO and O_2 concentrations as a function of time for 5×10^6 A375 melanoma cells. (Experiment 6)

Bibliography

Adler, H., Frech, B., Thony, M., Pfister, H., Peterhans, E., Jungi, T. W., (1995) Inducible nitric oxide synthase in cattle. Differential cytokine regulation of nitric oxide synthase in bovine and murine macrophages. *J Immunol. 154*, 4710–4718.

Ahmed, B. and Van Den Oord, J. J. (1999) Expression of the neuronal isoform of nitric oxide synthase (nNOS) and its inhibitor, protein inhibitor of nNOS, in pigment cell lesions of the skin. *Br J Dermatol, 141*, 12-19.

Alitalo, K., and Carmeliet, P., (2002) Molecular mechanisms of lymphangiogenesis in health and disease. *Cancer Cell. 1*, 219–227.

Ambs, S., Merriam, W. G., Bennett, W. P., Felley-Bosco, E., Ogunfusika, M. O., Oser, S. M., Klein, S., Shields, P. G., Billiar, T. R., and Harris, C. C., (1998) Frequent nitric oxide synthase-2 expression in human colon adenomas: implication for tumor angiogenesis and colon cancer progression. *Cancer Res. 58*, 334-341.

Andrews, P. J., Harant, H., and Lindley, I. J. D. (1995) Nitric oxide regulates IL-8 expression in melanoma cells at the transcriptional level. *Biochem Biophys Res Comm. 214,* 949-946.

Annane, D., Sanquer, S., Sebille, V., Faye, A., Djuranovic, D., Raphael, J. C., Gajdos, P., and Bellissant, E., (2000) Compartmentalized inducible nitric-oxide synthase activity in septic shock. *Lancet. 355*, 1143–1148.

Anstey, N. M., Weinberg, J. B., Hassanali, M. Y., Mwaikambo, E. D., Manyenga, D., Misukonis, M. A., Arnelle, D. R., Hollis, D., McDonald, M. I., and Granger, D, L., (1996) Nitric oxide in Tanzanian children with malaria: inverse relationship between malaria severity and nitric oxide production/nitric oxide synthase type 2 expression. *J Exp Med.184*, 557–567.

Araki, K., Furuya, Y., Kobayashi, M., Matsuura, K., Ogata, T., and Isozaki, H., (1996) Comparison of mucoscal microvasculature between the proximal and distal human colon. *J Electron Microsc. 45,* 202-206.

Auger, M. J., and Ross, J. A. (1992) The biology of the macrophage. In: *The Macrophage* (Lewis, C. E. and McGee, J. O. D., Eds) Oxford University Prses, Oxford, pp. 1-57.

Babior, B. M., (1984) The respiratory burst of phagocytes. *J Clin Invest. 73*, 599-601.

Balch, C. M., Soong, S., Gershenwald, J. E., Thompson, J. F., Reintgen, D. S., Cascinelli, N., Urist, M., McMasters, K. M., Ross, M. I., Kirkwood, J. M., Atkins, M. B., Thompson, J. A., Coit, D. G., Byrd, D., Desmond, R., Zhang, Y., Liu, P., Lyman, G. H., Morabito, A. (2001) Prognostic factors analysis of 17,600 melanoma patients: validation of the American Joint Committee on Cancer melanoma staging system. *J Clin Oncol. 19* 3622-3634.

Balis, U. J., Behnia, K., Dwarakanath, B., Bhatia, S. N., Sullivan, S. J., Yarmush, M. L., and Toner, M. (1999) Oxygen consumption characteristics of porcine hepatocytes. *Metab Eng. 1*, 49-62.

Berg, D. J., Davidson, N., Kuhn, R., Muller, W., Menon, S., Holland, G., Thompson-Snipes, L., Leach, M. W., and Rennick, D., (1996) Enterocolitis and colon cancer in Interleukin-10-deficient mice are associated with aberrant cytokine production and $CD4^+$ TH1-like responses. *J Clin Invest. 98*, 1010-1020.

Berton, G., Dusi, S., and Bellavite, P., (1988) The respiratory burst of phagocytes. In *The Respiratory Burst and Its Physiological Significance* (Sbarra, A. J., and Strauss, R. R., Eds.) Plenum Press, New York, pp 33-52.

Bogdan, C. (2001) Nitric oxide and the immune response. *Nature Immun. 2,* 907-916.

Boughton-Smith, N.K., Evans, S. M., Hawkey, C. J., Cole, A. T., Balsitis, M., Whittle, B. J. R., and Moncada, S., (1993) Nitric oxide synthase activity in ulcerative colitis and Crohn's disease. *Lancet. 342*, 338-340.

Boveris, A., Oshino, N., and Chance, B., (1972) The cellular production of hydrogen peroxide. *Biochem J. 128*, 617-630.

Bray, R. C., Cockle, S. A., Fielden, E. M., Roberts, P. B., Rotilio, G., and Calabres, L., (1974) Reduction and inactivation of superoxide dismutase by hydrogen peroxide. *Biochem J. 139*, 43-48.

Brocker, E.B., Zwaldo, G., Holzmann, B., Macher, E. and Sorg, C., (1988) Inflammatory cell infiltrates in human melanoma at different stages of tumor progression. *Int J Cancer*, 41, 562–567.

Brown, G. C. and Cooper, C. E. (1994) Nanomolar concentrations of nitric oxide reversibly inhibit synaptosomal respiration by competing with oxygen at cytochrome oxidase. *FEBS Lett, 63,* 910-916.

Brown, G. C., Foxwell, N. and Moncada, S. (1998) Transcellular regulation of cell respiration by nitric oxide generated by activated macrophages. *FEBS Letters, 439, 321-324.*

Brown, G. C., (1999) Nitric oxide and mitochondrial respiration. *Biochim Biophys Acta. 1411*, 351-369.

Brune, B., Gotz, C., Mebmer, U. K., Sandau, K., Hirvonen, M., and Lapetina, E. G. (1997) Superoxide formation and macrophage resistance to nitric oxide-mediated apoptosis. *J Biol Chem. 272,* 7253-7258.

Burney, S. C., Dedon, P. C., and Tannenbaum, S. R., (1999) DNA damage in deoxynucleosides and oligonucleotides treated with peroxynitrite. *Chem Res Toxicol. 12*, 513-520.

Busam K. J., Antonescu C. R., Marghoob A. A. (2001) Histologic classification of tumor-infiltrating lymphocytes in primary cutaneous malignant melanoma. *Am J Clin Pathol.115,* 856-860.

Chan, E. D., Winston, B. W., Uh, S., Murray, W. W., Rose, D. M., Riches, W. H. (1999) Evaluation of the role of mitogen-activated protein kinases in the expression of inducible nitric oxide synthease by IFN-γ and TNF-α in mouse macrophages. *J Immun. 162,* 415-422.

Chen, B., and Deen, W. M., (2001) Analysis of the effects of cell spacing and liquid depth on nitric oxide and its oxidation products in cell cultures. *Chem Res Toxicol. 14*, 135-147.

Chen, B., and Deen, W. M., (2002) Effect of liquid depth on the synthesis and oxidation of nitric oxide in macrophage cultures. *Chem Res Toxicol. 15*, 490-496.

Cherayil, B. J., McCormick, B. A., and Bosley, J., (2000) *Salmonella enterica* serovar *typhimurium*–dependent regulation of inducible nitric oxide synthase expression in macrophages by invasins SipB, SipC, SipD and effector SopE2. *Infect Immun. 68*, 5567–5574.

Chin, M. P., Schauer, D. B., and Deen, W. M., (2008) Prediction of nitric oxide concentrations in the colonic crypt during inflammation. *Nitric Oxide. 19*, 266-275.

Crowell, J. A., Steele, V. E., Sigman, C. C., and Fay, J. R., (2003) Is inducible nitric oxide synthase a target for chemoprevention? *Mol Cancer Ther. 2*, 815–823.

Dadras, S., Paul, T., Bertoncini, J., Brown, L.F., Muzikansky, A., Jackson, D.G., Ellwanger, U., Garbe, C., Mihm, M.C., and Detmar, M. (2003) Tumor lymphangiogenesis: a novel prognostic indicator for cutaneous melanoma metastasis and survival. *Am J Pathol. 162*, 1951-1960.

Dalton, D. K., Pitts-Meek, S., Keshav, S., Figari, I. S., Bradley, A., and Stewart, T. A., (1993) Multiple defects of immune-cell function in mice with disrupted interferon-γ genes. *Science. 259*, 1739-1742.

deRojas-Walker, T., Tamir, S., Ji, H., Wishnok, J. S., and Tannenbaum, S. R., (1995) Nitric oxide induces oxidative damage in addition to deamination in macrophage DNA. *Chem Res Toxicol. 8*, 473-477.

Deen, W. M., (1998) Analysis of Transport Phenomena, Oxford University Press, New York.

Deen, W. M., Tannenbaum, S. R., and Beckman, J. S., (2002) Protein tyrosine nitration and peroxynitrites. *Comment FASEB J. 16*, 1144-1144.

Dignass, A. U., Podolsky, D. K., Rachmilewitz, D., (1995) NOx generation by cultured small intestinal epithelial cells. *Dig Dis Sci. 40*, 1859–1865.

Drath, D. B., and Karnovsky, M. L. (1975) Superoxide production by phagocytoxic leukocytes. *J Exp Med. 141*, 257-262.

Drucker, D. J., Yusta, B., Boushey, R. P., DeForest, L., and Brubaker, P. L., (1999) Human [Gly^2]GLP-2 reduces the severity of colonic injury in a murine model of experimental colitis. *Am J Physiol Gastrointest Liver Physiol. 276*, G79-G91.

Dykhuizen, R. S., Masson, J., McKnight, G., Mowat, A. N., Smith, C. G., Smith, L. M., and Benjamin, N., (1996) Plasma nitrate concentration in infective gastroenteritis and inflammatory bowel disease. *Gut. 39*, 393–395.

Eich, R. F., Li, T. S., Lemon, D. D., Doherty, D. H., Curry, S. R., Aitken, J. F., Mathews, A. J., Johnson, K. A., Smith, R. D., Phillips, G. N., and Olson, J. S., (1996) Mechanism of NO-induced oxidation of myoglobin and hemoglobin. *Biochemistry. 35*, 6976–6983.

Ekmekcioglu, S., Ellerhorst, J.A., Prieto, V.G., Johnson, M.M., Broemeling, L.D., and Grimm, E.A. (2000) Tumor iNOS predicts poor survival for stage III melanoma patients. *Int. J. Cancer. 119,* 861-866.

Ellsworth, M. L., and Pittman, R. N., (1983) Heterogeneity of oxygen diffusing through hamster striated muscles. *Am J Physiol Heart Circ Physiol. 246*, H161–H167.

Farrell, R. J., and Peppercorn, M. A., (2002) Ulcerative colitis. *Lancet. 359*, 331-340.

Franchi, A., Massi, D., Santucci, M., Masini, E., Degl'Innocenti, D. R., Magnelli, L., Fanti, E., Naldini, A., Ardinghi, C., Carraro, F., and Gallo, O., (2006) Inducible nitric oxide synthase activity correlates with lymphangiogenesis and vascular endothelial growth factor-C expression in head and neck squamous cell carcinoma. *J Pathology. 208*, 439-445.

Gal, A., and Wogan, G. N., (1996) Mutagenesis associated with nitric oxide production in transgenic SJL mice. *Proc Natl Acad Sci USA. 93*, 15102-15107.

Galle, J., Hoffmann, M., and Aust, G., (2009) From single cells to tissue architecture – a bottom-up approach to modeling the spatio-temporal organization of complex multi-cellular systems. *J Math Biol. 58*, 261-283.

Gallo, O., Masini, E., Morbidelli, L., Franchi, A., Fini-Storchi, I., Vergari, W. A., and Ziche, M., (1998) Role of nitric oxide in angiogenesis and tumor progression in head and neck cancer. *J Natl Cancer Inst. 90*, 584-596.

Gao, J. J., *Zuvanich, E. G., Xue, Q., Horn' D. L., Silverstein, R., and Morrison, D. C., (1999)* Bacterial DNA and LPS act in synergy in inducing nitric oxide production in RAW 264.7 macrophages. *J Immunol. 163*, 4095–4099.

Gardner, P. R., Gardner, A. M., and Martin, L. A., (2000) Nitric oxide dioxygenase activity and function of flavohemoglobins. *J Biol Chem. 275*, 31581-31587.

Gardner, P. R., Martin, L. A., Hall, D., and Gardner, A. M., (2001) Dioxygen-dependent metabolism of nitric oxide in mammalian cells. *Free Radic Biol Med. 31*, 191-204.

Geller, D. A., Nussler, A. K., Di Silvo, M., Lowenstein, C. J., Shapiro, R. A., Wang, S. C., Simmons, R. L., Billiar, T. R. (1993) Cytokines, endotoxin, and glucocorticoids regulate the expression of inducible nitric oxide synthase in hepatocytes. *Proc Natl Acad Sci. 90*, 522-526.

Giorgadze, T. A., Zhang, P. J., Pasha, T., Coogan, P. S., Acs, G., Elder, D. E., and Xu, X. (2004) Lymphatic vessel density is significantly increased in melanoma. *J Cut Pathol. 31*, 672-677.

Grimm, E. A. (2008) Constitutive intracellular production of iNOS and NO in human melanoma: possible role in regulation of growth and resistance to apoptosis. *Nitric Oxide. 19*, 133-137

Goldstick, T. K., and Fatt, I., (1970) Diffusion of oxygen in solutions of blood proteins. *Mass transfer in biological systems. 66*, 101-113.

Halliwell, B., and Gutteridge, J. M. C., (1989) Free radicals in biology and medicine. Clarendon Press, Oxford, pp 379-380.

Herulf, M., Ljung, T., Hellstrom, P. M., Weitzberg, E., and Lundberg, J. O. N., (1998) Increased luminal nitric oxide in inflammatory bowel disease as shown with a novel minimally invasive method. *Scand J Gastroenterol. 33*, 164-169.

Hibbs, J. B. Jr., Westenfelder, C., Taintor, R., Vavrin, Z., Kablitz, C., Baranowski, R. L., Ward, J. H., Menlove, R. L., McMurry, M. P., and Kushner, J. P., (1992) Evidence for cytokine-inducible nitric oxide synthesis from L-arginine in patients receiving interleukin-2 therapy. *J Clin Invest. 89*, 867-877.

Hirsch, T., Marzo, I., and Kroemer, G., (1997) Role of the mitochondrial permeability transition pore in apoptosis. *Biosci Rep. 17,* 67-76.

Hofseth, L. J., Hussain, S. P., Wogan, G. N., and Harris, C. C., (2003) Nitric oxide in cancer and chemoprevention. *Free Radic Biol Med. 34*, 955–968.

Holian, O., Wahid, S., Atten, M. J., and Attar, B. M., (2002) Inhibition of gastric cancer cell proliferation by resveratrol: role of nitric oxide. *Am J Physiol Gastrointest Liver Physiol. 282*, G809-G816.

Hornef, M. W., Frisan, T., Vandewalle, A., Normark, S., and Richter-Dahlfors, A., (2002) Toll-like receptor 4 resides in the Golgi apparatus and colocalizes with internalized lipopolysaccharide in intestinal epithelial cells. *J Exp Med. 195*, 559-570.

Huie, R. E., and Padmaja, S., (1993) The reaction of NO with superoxide. *Free Radic Res Commun. 18*, 195-199.

Ischiropoulos, H., Zhu, L., and Beckman, J. S., (1992) Peroxynitrite formation from macrophage-derived nitric oxide. *Arch Biochem Biophys. 298*, 446-451.

Johnston, R. B., Lehmeyer, J. E., and Guthrie, L. A. (1975) Generation of superoxide anion and chemiluminescence by human monocytes during phagocytosis and on contact with surface-bound immunoglobulin G. *J Exp Med.143,* 1551-1556.

Johnston, R. B., Godzik, C. A., and Cohn, Z. A. (1978) Increased superoxide anion production by immunologically activated and chemically elicited macrophages. *J Exp Med. 148,* 115-129.

Jungi, T. W., Adler, H., Adler, B., Pfister, H., Brcic, M., Thony, M., Tipold, A., Zurbriggen, A., Fatzer, R., Pauli, U., and Peterhans, E., (1996) Regulation of inducible nitric oxide synthase in ungulate mononuclear phagocytes. Presented at *FASEB Res. Conf. on Principles in Viral, Bacterial, Fungal and Protozoan Pathogenesis, Snowmass, CO.*

Keynes, R. G., Griffiths, C., and Garthwaite, J., (2003) Superoxide-dependent consumption of nitric oxide in biological media may confound *in vitro* experiments. *Biochem J. 369*, 399-406.

Kim, M. Y. and Wogan, G. N. (2006) Mutagenesis of the *sup*F gene of pSP189 replicating in AD293 cells cocultivated with activated macrophages: roles of nitric oxide and reactive oxygen species. *Chem Res Toxiol. 19*, 1483-1491.

Kimura, H., Hokari., R., Miura, S., Shigetmatsu, T., Hirokawa, M., Akiba, Y., Kurose, I., Higuchi, H., Fujimori, H., Tsuzuki, Y., Serizawa, H., and Ishii, H., (1998) Increased expression of an inducible isoform of nitric oxide synthase and the formation of peroxynitrite in colonic mucosa of patients with active ulcerative colitis. *Gut. 42*, 180-187.

Kiss, J., Timar, J., Somlai, B., Gilde, K., Fejos, Z., Gaudi, I., Ladanyi, A. (2007) Association of microvessel density with infiltrating cells in human cutaneous malignant melanoma. *Path Oncol Res. 13*, 21-31.

Kobzik, L., Bredt, D. S., Lowenstein, C. J., Drazen, J., Gaston, B., Sugarbaker, D., and Stamler, J. S., (1993) Nitric oxide synthase in human and rat lung: immunocytochemical and histochemical localization. *Am J Respir Cell Mol Biol. 4*, 371–377.

Kolios, G., Rooney, N., Murphy, C. T., Robertson, D. A. F., Westwick, J., (1996) Expression of inducible nitric oxide synthase activity in human colon epithelial cells: modulation by T lymphocyte derived cytokines. *Gut. 43*, 56-63.

Konopka, T. E., Barker, J. E., Bamford, T. L., Guida, E., Anderson, R. L., and Stewart, A. G., (2001) Nitric oxide synthase II gene disruption: implications for tumor growth and vascular endothelial growth factor production. *Cancer Res. 61*, 3182–3187.

Lamkin-Kennard, K. A., Buerk, D., and Jaron, D., (2004) Interactions between NO and O_2 in the microcirculation: a mathematical analysis. *Microvasc Res. 68*, 38-50.

Lancaster, J., (1994) Simulation and diffusion of endogenously produced nitric oxide. *Proc Natl Acad Sci. 91*, 8137-8141.

Lange, N.A., Ed. (1967) Lange's Handbook of Chemistry, rev. 10th ed., p 1101, McGraw-Hill, New York.

Lee, J. S., Zhang, Y., and Ro, J. Y., (2008) Involvement of neuronal, inducible and endothelial nitric oxide synthases in capsaicin-induced muscle hypersensitivity. *Eur J Pain.13*, 924-928.

Leithäuser, F., Trobonjaca, Z., Möller, P., and Reimann, J., (2001) Clustering of colonic lamina propria $CD4^+$ T cells to subepithelial dendritic cell aggregates precedes the development of colitis in a murine adoptive transfer model. *Lab Invest. 81*, 1339-1349.

Leschelle, X., Delpal, S., Goubern, M., Blottiere, H., Blachier, F., (2000) Butyrate metabolism upstream and downstream acetyl-coA synthesis and growth control of human colon carcinoma cells. *Eur J Biochem. 267*, 6435-6442.

Leskovar, A., Moriarty, L. J., Turek, J., Schoenlein, I., and Borgens, R. B., (2000) The macrophage in acute neural injury: changes in cell numbers over time and levels of cytokine production in mammalian central and peripheral nervous systems. *J Exp Biol. 203*, 1783-1795.

Levin, B., (1993) Ulcerative colitis and colon cancer: biology and surveillance. *J Cell Biochem Suppl. 16G*, 47-50.

Lewis, R. S., and Deen, W. M., (1994) Kinetics of the reaction of nitric oxide with oxygen in aqueous solutions. *Chem Res Toxiol. 7*, 568-574.

Lewis, R. S., Tamir, S., Tannenbaum, S. R., and Deen, W. M., (1995) Kinetic analysis of the fate of nitric oxide synthesized by macrophages *in vitro*. *J Biol Chem. 270*, 29350-29355.

Lewis, R. S., Tannenbaum, S. R., and Deen, W. M., (1995) Kinetics of N-nitrosation in oxygenated nitric-oxide solutions at physiological pH – role of nitrous anhydride and effects of phosphate and chloride. *J Am Chem Soc. 117*, 3933-3939.

Li, Q., Pang, B., Kiziltepe, T., Trudel, L., Engelward, B. P., Dedon, P., and Wogan, G. N., (2006) Threshold effects of nitric oxide-induced toxicity and cellular responses in wild-type and p53-null human lymphoblastoid cells. *Chem Res Toxicol. 19*, 399-406.

Li, Q., Kim, M. Y., Godoy, L. C., Thiantanawat, A., Trudel, L. J., and Wogan, G. N., (2009) Nitric oxide activation of Keap1/Nrf2 signaling in human colon carcinoma cells. *Proc Natl Acad Sci. 106*, 14547 – 14551.

Lim, C. H., Dedon, P. C., and Deen, W. M., (2008) Kinetic analysis of intracellular concentrations of reactive nitrogen species. *Chem Res Toxicol. 21*, 2134-2147.

Lipkin, M., (1974) Phase 1 and phase 2 proliferative lesions of colonic epithelial cells in diseases leading to colon cancer. *Cancer. 34*, 878-888.

Lipkin, M., (1985) Growth and development of gastrointestinal cells. *Ann Rev Physiol. 47*, 175-197.

Ludwig, H. C., Feiz-Erfan, I., Bockermann, V., Behnke-Mursch, J., Schallock, K., and Markakis, E., (2002) Expression of nitric oxide synthase isozymes (NOS I-III) by immunohistochemistry and DNA in situ hybridization. Correlation with macrophage presence, vascular endothelial growth factor (VEGF) and oedema volumetric data in 220 glioblastomas. *Anticancer Res.* 20, 299-304.

Lundberg, J. O. N., Hellstrom, P. M., Lundberg, J. M., and Alving, K., (1994) Greatly increased luminal nitric oxide in ulcerative colitis. *Lancet. 344*, 1673-1674.

Lymar, S. V., and Hurst, J. K., (1996) Physiological catalyst for peroxynitrite-mediated cellular damage or cellular protectant? *Chem Res Toxicol. 9*, 845-850.

Maciejewski, J. P., Selleri, C., Sato, T., Cho, H. J., Keefer, L. K., Nathan, C. F., and Young, N. S. (1995) Nitric oxide suppression of human hematopoiesis *in vitro*. Contribution to inhibitory action of interferon-gamma and tumor necrosis factor-alpha. *J Clin Invest. 96*, 1085-1092.

MacMicking, J. Xie, Q.W., Nathan, C. (1997) Nitric oxide and macrophage function. *Ann Rev Immun. 14*, 323-350.

Marletta, M. A., Yoon, P. S., Iyengar, R., Leaf, C. D., and Wishnok, J. S., (1998) Macrophage oxidation of L-arginine to nitrite and nitrate: nitric oxide is an intermediate. *Biochemistry.* 27, 8706-8711.

Marrogi, A. J., Travis, W. D., Welsh, J. A., Khan, M. A., Rahim, H., Tazelaar, H., Pairolero, P., Trastek, V., Jett, J., Caporaso, N. E., Liotta, L. A., and Harris, C. C., (2000) Nitric oxide synthase, cyclooxygenase 2, and vascular endothelial growth factor in the angiogenesis of non-small cell lung carcinoma. *Clin Cancer Res. 6*, 4739-4744.

Massey, V., (1959) The microestimation of succinate and the extinction coefficient of cytochrome c. *Biochim Biophys Acta. 35*, 255-256.

Massi, D., De Nisi, M. C., Franchi, A., Mourmouras, V., Baroni, G., Panelos, J., Santucci, M., Miracco, C. (2009) Inducible nitric oxide synthase expression in melanoma; implications in lymphangiogenesis. *Mod Path. 22*, 21-30.

McCormick, C. G., Li, W. P., Calero, M. (2000) Oxygen tension limits nitric oxide synthesis by activated macrophages. *Biochem. J. 350*, 709–716.

McLaren, W., Anikijenko, P., Thomas, S., Delaney, P., and King, R., (2002) *In vivo* detection of morphological and microvascular changes of the colon in association with colitis using fiberoptic confocal imaging. *Dig Dis Sci. 47*, 2424-2433.

Middleton, S. J., Shorthouse, M., and Hunter, J. O., (1993) Increased nitric oxide synthesis in ulcerative colitis. *Lancet. 341*, 465-466.

Mohiuddin, A., (1966) Blood and lymph vessels in the jejunal villi of the white rat. *Anat Rec. 156*, 83-89.

Mori, N., Nunokawa, Y., Yamada, Y., Ikeda, S., Tomonaga, M., and Yamamoto, N., (1999) Expression of human inducible nitric oxide synthase gene in T-cell lines infected with human T cell leukemia virus type I and primary adult T-cell leukemia cells. *Blood. 94*, 2862–2870.

Morton, D.L., Essner, R., Kirkwood, J.M., and Wollman, R.C. (2006) Malignant melanoma. In *Cancer Medicine* (Kuff, D.W., Bast, R.C., Hait, W.N., Hong, W.K., Pollock, R.E., Weichselbam, R.R., Holland, J.F., Frei, E. , Eds.) pp 1640-1662, American Association for Cancer Research, New York.

Muñoz-Fernández, M. A., Fernández, M. A., Fresno, M., (1992) Activation of human macrophages for the killing of intracellular Trypanosoma cruzi by TNF-alpha and IFN-gamma through a nitric oxide-dependent mechanism. *Immunol Lett. 33*, 35-40.

Murray, H. W., Spitalny, G. L., and Nathan, C. F. (1985) Activation of mouse peritoneal macrophages *in vitro* and *in vivo* by interferon-gamma. *J Immunol. 134*, 1619-1622.

Nakamura, Y., Yasuoka, H., Tsujimoto, M., Yoshidome, K., Nakahara, M., Nakao, K., Nakamura, M., and Kakudo, K., (2006) Nitric Oxide in Breast Cancer: Induction of Vascular Endothelial Growth Factor-C and Correlation with Metastasis and Poor Prognosis. *Clin Cancer Res. 12*, 1201-1207.

Nalwaya, N., and Deen, W. M., (2003) Analysis of cellular exposure to peroxynitrite in suspension cultures. *Chem Res Toxicol. 16*, 920-932.

Nalwaya, N., and Deen, W. M., (2004) Analysis of effects of nitric oxide and oxygen on nitric oxide production by macrophages. *J Theor Biol. 226*, 409-419.

Nalwaya, N., and Deen, W. M., (2005) Nitric oxide, oxygen, and superoxide formation and consumption in macrophage cultures. *Chem Res Toxicol. 18*, 486-493.

Nam, K. T., Oh, S.-Y., Ahn, B., Kim, Y. B., Jang, D. D., Yang, K.-H., Hahm, K.-B., and Kim, D.-Y., (2004) Decreased *Helicobacter pylori* associated gastric carcinogenesis in mice lacking inducible nitric oxide synthase. *Gut. 53*, 1250–1255.

Nathan, C. F., Murray, H. W., Wiebe, M. E., and Rubin, B. Y. (1983) Identification of interferon-y as the lymphokine that activates human macrophage oxidative metabolism and antimicrobial activity. *J Exp Med. 158*, 670-689.

Nathan, C. F., Prendergast, T. J., Wiebe, M. E., Stanley, E. R., Platzer, E., Remold, H. G., Welte K., Rubin, B. Y. and Murray, H. W. (1984) Activation of human macrophages: comparison of other cytoklnes with interferon-y. *J.* Exp. Med. *160,* 600-605.

Nathan, C., and Xie, Q. W., (1994) Regulation of biosynthesis of nitric oxide. *J Biol Chem. 269*, 13725–13728.

Nejdfors, P., Wang, Q., Ekelund, M., Westrom, B. R., Jansson, O., Lindstrom, C. L., Karlsson, B., and Jeppsson, B., (1998) Increased colonic permeability in patients with ulcerative colitis: an *in vitro* study. *Scand J Gastroenterol. 3*, 749-753.

Newman, J., Kosaka, T., Sheppard, B. J., Fox, J. G., and Schauer, D. B., (2001) Bacterial infection promotes colon tumorigenesis in Apc$^{Min/+}$ mice. *J Infect Dis. 184*, 227-230.

Nicholson, S., Bonecini-Almeida, M. D., Lapa e Silva, J. R., Nathan, C., Xie, Q. W., Mumford, R., Weidner, J. R., Calaycay, J., Geng, J., Boechat, N., Linhares, C., Rom, W., and Ho, J. L., (1996) Inducible nitric oxide synthase in pulmonary alveolar macrophagesfrom patients with tuberculosis. *J Exp Med. 183*, 2293–2302.

Niu, X. J., Wang, Z. R., Wu, S. L., Geng, Z. M., Zhang, Y. F., and Qing, X. L., (2004) Relationship between inducible nitric oxide synthase expression and angiogenesis in primary gallbladder carcinomatissue. *World J Gastroenterol. 10*, 725-728.

Nozaki, Y., Hasegawa, Y., Ichiyama, S., Nakashima, I., and Shimokata, K., (1997) Mechanism of nitric oxide-dependent killing of *Mycobacterium bovis* BCG in human alveolar macrophages. *Infect Immun, 65*, 3644–3647.

Ohashi, K., Burkart, V., Flohe, S., and Kolb, H., (2000) Heat shock protein 60 is a putative endogenous ligand of the Toll-like receptor-4 complex. *J Immunol. 164*, 558–561.

Otto, C. M., and Baumgardner, J. E. (2001) Effect of culture P_{O_2} on macrophage (RAW 264.7) nitric oxide production. *Am. J. Physiol. 280*, C280–C287

Packer, M. A., Scarlette, J. L., Martin, S. W., and Murphy, M. P., (1997) Induction of the mitochondrial permeability transition by peroxynitrite. *Biochem Soc Trans. 25*, 909-914.

Pahan, K., Sheikh, F., Namboodiri, A., and Singh, I. (1997) N-Acetyl cysteine inhibits induction of NO production by endotoxin or cytokine stimulated rat peritoneal macrophages, C_6 glial cells and astrocytes. *Free Rad Bio Med. 24*, 39-48.

Palmer, L. A., Semenza, G. L., Stoler, M. H., and Johns, R. A. (1998) Hypoxia induces type ii nos gene expression in pulmonary artery endothelial cells via hif-1. *Am. J. Physiol. 274*, L212–L219.

Paulsen, J., Namork, E., Steffensen, I., Eide, T., and Alexandar, J., (2000) Identification and quantification of aberrant crypt foci in the colon if Min mice – a murine model of familial adenomatous polyposis. *Scand J Gastroenterol. 35*, 534-539.

Phillipides, A., Husbands, P., and O'Shea, M., (2000) Four-dimensional neuronal signaling by nitric oxide: a computational analysis. *J Neurosci. 20*, 1199-1207.

Phillips, W. A. and Hamilton, J. A. (1989) Phorbol ester-stimulated superoxide producton by murine bone marrow-derived macrophages requires preexposure to cytokines. *J Immunol. 142*, 2445-2449.

Potten, C. S., and Lowffler, M., (1990) Stem cells: attributes, cycles, spirals, pitfalls and uncertainties. Lessons for and from the crypt. *Development. 110*, 1001–1020.

Preston, S. L., Wong, W., Chan, A. O., Poulsom, R., Jeffery, R., Goodlad, R. A., Mandir, N., Elia, G., Novelli, M., Bodmer, W. F., Tomlinson, I. P., and Wright, N. A., (2003) Bottom-up histogenesis of colorectal adenomas. *Cancer Res. 63*, 3819-3825.

Pull, S., Doherty, J., Mills, J., Gordon, J., and Stappenbeck, T., (2004) Activated macrophages are an adaptive element of the colonic epithelial progenitor niche necessary for regenerative responses to injury. *Proc Natl Acad Sci. 102*, 99-104.

Rachmilewitz, D., Stamler, J. S., Bachwich, D., Karmeli, F., Ackerman, Z., Podolsky, D. K., (1995) Enhanced colonic nitric oxide generation and nitric oxide synthase activity in ulcerative colitis and Crohn's disease. *Gut. 36*, 718–723.

Radi, R., Beckman, J. S., Bush, K. M., and Freeman, B. A., (1991) Peroxynitrite induced membrane lipid peroxidation: the cytotoxic potential of superoxide and nitric oxide. *Arch Biochem Biophys. 288,* 481-487.

Reiling, N., Ulmer, A. J., Duchrow, M., Ernst, M., Flad, H. D., and Hauschildt, S., (1994) Nitric oxide synthase: mRNA expression of different isoforms in human monocytes/macrophages. *Eur J Immunol. 24*, 1941–1944.

Rengasamy, A., and Johns, R. A., (1996) Determination of K_m for oxygen of nitric oxide synthase isoforms. *J Pharmacol Exp Ther. 276*, 30-33.

Ribbons, K. A., Zhang, X., Thompson, J. H., Greenberg, S. S., Moore, W. M., Kornmeier, C. M., Currie, M. G., Lerche, N., Blanchard, J., Clark, D. A., Miller, M. J. S., (1995) Potential role of nitric oxide in a model of chronic colitis in rhesus macaques. *Gastroenterology. 108*, 705–711.

Rouzer, C. A., Jacobs, A. T., Nirodi, C. S., Kinglsey, P. J., Morrow, J. D., Marnette, L. J. (2005) RAW264.7 cells lack prostaglandin-dependent autoregulation of tumor necrosis factor-a secretion. *J Lipid Research, 46,* 1027-1037.

Ruffieux, P., Stockar, U. V., Marison, I. W., (1998) Minireview: Measurement of volumetric (OUR) and determination of specific (qO_2) oxygen uptake rates in animal cell cultures. *J Biotechnol. 63*, 85-95.

Santolini, J., Meade, A. L., and Stuehr, D. J. (2001) Differences in three kinetic parameters underpin the unique catalytic profiles of nitric-oxide synthases i, ii, and iii. *J. Biol. Chem. 276*, 48887–48898.

Sasada, M., Pabst, M. J., Johnston, R. B. (1983) Activation of mouse peritoneal macrophages by lipopolysaccharide alter s the kinetic parameters of the superoxide-producing NADPH oxidase. *J Biol Chem, 258,* 9631-9635.

Schneemann, M., Schoedon, G., Hofer, S., Blau, N., Guerrero, L., and Schaffner, A., (1993) Nitric oxide synthase is not a constituent of the antimicrobial armature of human mononuclear phagocytes. *J Infect Dis. 167*, 1358–1363.

Shen, Z., Feng, Y., Rogers, A. B., Rickman, B., Whary, M. T., Xu, S., Clapp, K. M., Boutin, S. R., and Fox, J. G., (2009) Cytolethal distending toxin promotes Helicobacter cinaedi-associated typhlocolitis in interleukin-10-deficient mice. *Infect Immun. 77*, 2508-2516.

Sheridan, J. W., Bishop, C. J., and Simmons, R. J. (1981). Biophysical and morphological correlates of kinetic change and death in a starved human melanoma cell line. *J Cell Sci. 49*, 119-137.

Shih, I. M., Wang, T., Traverso, G., Romans, K., Hamilton, S. R., Ben-Sasson, S., Kinzler, K. W., and Vogelstein, B., (2001) Top-down morphogenesis of colorectal tumors. *Proc Natl Acad Sci. 98*, 2640-2645.

Shoda, L. K. M**.,** Kegerreis, K. A., Suarez, C. E., Roditi, I., Corral, R. S., Bertot, G. M., Norimine, J., and Brown, W. C., (2001) DNA from protozoan parasites *Babesia bovis*, *Trypanosoma cruzi*, *T. brucei* is mitogenic for B lymphocytes and stimulates macrophage expression of interleukin-12, tumor necrosis factor-α and nitric oxide. *Infect Immun. 69*, 2162–2171.

Singer, I., Kawka, D. W., Scott, S., Weidner, J. R., Mumford, R. A., Riehl, T. E., and Stenson, W. F., (1996) Expression of inducible nitric oxide synthase and nitrotyrosine in colonic epithelium in inflammatory bowel disease. *Gastroenterology. 111*, 871-885.

Smith, M. A., Harris, P. L. R., Sayre, L. M., Beckman, J. S., and Perry, G., (1997) Widespread pesroxynitrite mediated damage in Alzheimer's disease. *J Neurosci. 17*. 2653-2657.

Sohn, J. J-h., (2005) Intestinal cancer: linking infection, inflammation and neoplasia. Ph.D. Thesis, MIT.

Song, Z. J., Gong, P., and Wu, Y. E., (2002) Relationship between the expression of iNOS, VEGF, tumor angiogenesis and gastric cancer. *World J Gastroenterol. 8*, 591-595.

St. Clair, E. W., Wilkinson, W. E., Lang, T., Sanders, L., Misukonis, M. A., Gilkeson, G. S., Pisetsky, D. S., Granger, D. L., and Weinberg, J. B., (1996) Increased expression of blood mononuclear cell nitric oxide synthase type 2 in rheumatoid arthritis patients. *J Exp Med. 184*, 1173–1178.

Stamler, J., Jaraki, O., Osborne, J., Simon, D. I., Keane, J., Vita, J., Singel, D., Valeri, C. R., and Loscalzo, J., (1992) Nitric oxide circulates in mammalian plasma primarily as an S-Nitroso adduct of serum albumin. *Proc Natl Acad Sci. 89*, 7674-7677.

Straume, O., Jackson, D. G., and Akslen, L. A. Independent prognostic impact of lymphatic vessel density and presence of low-grade lymphangiogenesis in cutaneous melanoma. *Clin Cancer Res. 9,* 250-256.

Stuehr, D. J., and Marletta, M. A., (1985) Mammalian nitrate biosynthesis: mouse macrophages produce nitrite and nitrate in response to Escherichia coli lipopolysaccharide. *Proc Natl Acad Sci USA. 82*, 7738-7742.

Stuehr, D. J., and Marletta, M. A., (1987) Synthesis of nitrite and nitrate in murine macrophage cell lines. *Cancer Research. 47*, 5590-5594.

Stuehr, D. J., and Nathan, C. F. (1989) Nitric oxide: a macrophage product responsible for cytostasis and respiratory inhibition in tumor target cells. *J Exp Med. 169*, 1543-1545.

Stuehr, D. J., (1999) Mammalian nitric oxide synthases. *Biochim Biophys Acta. 1411*, 217-230.

Subczynski, W. K., Lomnicka, M., and Hyde, J. S., (1996) Permeability of nitric oxide through lipid bilayer membranes. *Free Radic Res. 24*, 343-349.

Suzuki, M., Hisamatsu, T., and Podolsky, D. K., (2001) Gamma interferon augments the intracellular pathway for lipopolysaccharide recognition in human intestinal epithelial cells through coordinated up-regulation of LPS uptake and expression of the intracellular toll-like receptor 4-MD-2 complex. *Infect Immun. 71*, 3503-3511.

Swietach, P., Patiara, S., Supuran, C. T., Harris, A. L., and Vaughan-Jones, R. D., (2009) The role of carbonic anhydrase 9 in regulating extracellular and intracellular pH in three-dimensional tumor cell growths. *J Biol Chem. 284,* 20299-20310.

Tamir, S., and Tannenbaum, S. R., (1996) The role of nitric oxide in the carcinogenic process. *Biochim Biophys Acta. 1288*, F31-F38.

Tang, C. and Grimm, E.A. (2004) Depletion of endogenous nitric oxide enhances cisplatin-induced apoptosis in a p53-dependent manner in melanoma cell lines. *J Biol Chem. 279,* 288-98.

Tannenbaum, S. R., Fett, D., Young, V. R., Land, P. D., and Bruce, W. R., (1978) Nitrile and nitrate are formed by endogenous synthesis in the human intestine. *Science. 200*, 1487-1489.

Tannenbaum, S. R., Tamir, S., deRojas-Walker, T., and Wishnok, J. S., (1994) DNA Damage and Cytotoxicity Caused by Nitric Oxide. In: *Nitrosamines and Related N-Nitroso Compounds: Chemistry and Biochemistry* (Loeppky, R. N., and Michejda, C. J., eds.) American Chemical Society, Washington, D.C., pp120-135.

Taylor, C. T., and Colgan, S. P., (2007) Hypoxia and gastrointestinal disease. *J Mol Med. 85*, 1295-1300.

Thomas, D., Liu, X., Kantrow, S., and Lancaster, J., (2001) The biological lifetime of nitric oxide: implications for the perivascular dynamics of NO and O_2. *Proc Natl Acad Sci. 98*, 355-360.

Thoma-Uszynski, S., Stenger, S., Takeuchi, O., Ochoa, M. T., Engele, M., Sieling, P. A., Barnes, P. F., Röllinghoff, M., Bölcskei, P. L., Wagner, M., Akira, S., Norgard, M. V., Belisle, J. T., Godowski, P. J., Bloom, B. R., and Modlin, R. L., (2001) Induction of direct antimicrobial activity through mammalian Toll-like receptors. *Science. 291*, 1544–1547.

Thomas, D., Espey, M. G., Ridnour, L. A., Hofseth, L. J., Mancardi, D., Harris, C. C., and Wink, D., (2004) Hypoxic inducible factor 1, extracellular signal-regulated kinase, and p53 are regulated by distinct threshold concentrations of nitric oxide. *Proc Natl Acad Sci. 101*, 8894-8899.

Tomczak, M. F., Erdman, S. E., Poutahidis, T., Rogers, A. B., Holcombe, H., Plank, B., Fox, J. G., and Horwitz, B. H., (2003) NF-$\kappa\beta$ is required within the innate immune system to inhibit microflora-induced colitis and expression of IL-12 p40. *J Immunol. 171*, 1484-1492.

Torisu, H., Ono, M., Kiryu, H., Furue, M., Ohmoto, Y., Nakayama, J., Nishioka, S.S., and Kuwano, M. (2000) Macrophage infiltration correlates with tumor stage and angiogenesis in human malignant melanoma: possible involvement of TNF-α and Il-1α. *Int J Cancer,* 182-188.

Tretyakova, N. Y., Burney, S., Pamir, B., Wishnok, J. S., Dedon, P. C., Wogan, G. N., and Tannenbaum, S. R., (2000) Peroxynitrite-induced DNA damage in the supF gene: Correlation with the mutational spectrum. *Mutation Research. 447*, 287-303.

Trush, M. A., and Kensler, T. W., (1991) An overview of the relationship between oxidative stress sand chemical carcinogenesis. *Free Radical Biol Med. 10,* 201-209.

Tufto, I. and Rofstad, E. (1999) Interstitial fluid pressure and capillary diameter distribution in human melanoma xenografts. *Microvasc Res. 58*, 205-214.

Tyler, D. D. (1975) Polargraphic assay and intracellular distribution of superoxide dismutase in rat liver. *Biochem J. 147*, 493-504.

Vakkala, M., Kahlos, K., Lakari, E., Pääkkö, P., Kinnula, V., and Soini, Y., (2000) Inducible Nitric Oxide Synthase Expression, Apoptosis, and Angiogenesis in in Situ and Invasive Breast Carcinomas. *Clin Cancer Res.* 6, 2408-2416.

Vaughn, M., Kuo, L., and Liao, J., (1998) Estimation of nitric oxide production and reaction rates in tissue by use of a mathematical model. *Am J Physiol Heart Circ Physiol. 274,* H2163-H2176.

Vouldoukis, I., Riveros-Moreno, V., Dugas, B., Ouaaz, F., Becherel, P., Debre , P., Moncada, S., and Mossalayi, M. D., (1995) The killing of *Leishmania major* by human macrophages is mediated by nitric oxide induced after ligation of the Fc epsilon RII/CD23 surface antigen. *Proc Natl Acad Sci USA. 92*, 7804–7808.

Wagner, D. A., and Tannenbaum, S. R., (1982) Enhancement of nitrate biosynthesis by Escherichia coli lipopolysaccharide. In: *Nitrosamines and Human Cancer* (Magee, P. N., ed.) Cold Spring Harbor, NY, Cold Spring Harbor, pp 437–441.

Wagner, D. A., Young, V. R., and Tannenbaum, S. R., (1983) Mammalian nitrate biosynthesis: incorporation of NH_3 into nitrate is enhanced by endotoxin treatment. *Proc Natl Acad Sci USA. 80*, 4518-4521.

Wang, C., (2003) Controlled delivery of nitric oxide for cytotoxicity studies. Ph. D. Thesis, MIT.

Wang, C., Trudel, L., Wogan, G. N., and Deen, W. M., (2003) Thresholds of nitric oxide-mediated toxicity in human lymphoblastoid cells. *Chem Res Toxicol. 16*, 1004-1013.

Weinberg, J., Misukonis, M., Wood, E., Smith, G., Shami, P., Mason, S., and Granger, D., (1993) Human mononuclear phagocyte nitric oxide synthase (NOS): evidence for induction of NOS mRNA and protein without detectable capacity for nitric oxide production. *Blood. 82*, 186a.

Weinberg, J. B., (1998) Nitric oxide production and nitric oxide synthase type 2 expression by human mononuclear phagocytes: A review. *Mol Med. 4*, 557–591.

Witthoft, T**.,** Eckmann, **L.,** Kim., J. M., and Kagnoff, M. F., (1998) Enteroinvasive bacteria directly activate expression of iNOS and NO production in human colon epithelial cells. *Am J Physiol Gastrointest Liver Physiol. 275*, G564-571.

Wood, J., and Garthwaite, J., (1994) Models of the diffusional spread of nitric oxide: implications for neural nitric oxide signaling and its pharmacological properties. *Neuropharmacology. 33*, 1235-1244.

Wright, K., Kolios, G., Westwick, J., and Ward, S. G., (1999) Cytokine-induced apoptosis in epithelial HT-29 cells is independent of nitric oxide formation. *J Bio Chem. 274*, 17193-17201.

Xie, K., Huang, S., Dong, Z., Juang, S. H., Gutman, M., Xie, Q. W., Nathan, C., and Fidler, I. J. (1995) Tranfection with the inducible nitric oxide synthase gene suppresses tumorigenicity and abrogates metastasis by K-1735 murine melanoma cells. *J Exp Med. 181,* 1333-1343.

Yamada, T., Yang, J. J., Ricchiuti, N. V., and Seraydarian, M. W., (1985) Oxygen consumption of mammalian myocardial cells in culture: Measurements in beating cells attached to the substrate of the culture dish. *Anal Biochem. 145*, 302-307.

Zacharia, I., and Deen, W. M., (2005) Diffusivity and solubility of nitric oxide in water and saline. *Ann Biomed Eng. 33*, 214-222.

Zheng, M., Ekmekcioglu, S., Walch, E. T., Tang, C., and Grimm, E. A. (2004) Inhibition of nuclear factor-κB and nitric oxide by curcumin induces G_2/M cell cycle arrest and apoptosis in human melanoma cells. *Melanoma Res. 14,* 161-175.

Zhuang, J. C., and Wogan, G. N., (1997) Growth and viability of macrophages continuously stimulated to produce nitric oxide. *Proc Natl Acad Sci. 94*, 11875-11880.